MEMS SCANNERS ACTUATED WITH MECHANICAL COUPLING AND COMB DRIVES

by

Aslıhan Arslan

A Thesis Submitted to the

Graduate School of Engineering

in Partial Fulfillment of the Requirements for

the Degree of

Master of Science

in

Electrical and Computer Engineering

Koc University

December, 2008

Koc University

Graduate School of Sciences and Engineering

This is to certify that I have examined this copy of a master's thesis by

Aslıhan Arslan

and have found that it is complete and satisfactory in all respects,
and that any and all revisions required by the final
examining committee have been made.

Committee Members:

_____

Hakan Urey, Ph. D. (Advisor)

_____

Erdem Alaca, Ph. D.

_____

Yusuf Leblebici, Ph. D.

Date: _____

To my family…

ABSTRACT

MEMS microscanners are used to guide or manipulate the light beams more precisely and faster than conventional scanners. Microscanners are mostly used in display, imaging, telecommunication and barcode recognition applications.

In this thesis, a new actuation mechanism using mechanical coupling is demonstrated to increase the efficiency of the comb-drive MEMS scanners and provides large resonant deflections at low voltages. An additional outer frame is defined around the scanner and the comb actuators are presented only on the outer frame. At the mechanical coupling frequency of the 2-DoF (Degree- of- freedom) system, which is mainly defined by the stiffness of the scanner flexures and the scanner geometry, the deflection of the outer frame coupled to the scanner with a mechanical coupling efficiency (coupling gain). The main advantage of this system is that, a small electrostatic force generated in the comb fingers is sufficient to achieve large scanner deflections in comparison to 1-DoF systems. Moreover, this method is applicable to eliminate the pull-in limitation in the linear scanners and reduce the sliding film damping of the comb fingers on the torsional scanners.

The mechanical coupling efficiency and the mechanical coupling frequency formulae are derived analytically. To optimize the system for maximum deflection, numerical analysis of the mechanical coupling efficiency is performed, as well. Different linear and torsional scanners are designed and fabricated in this work using SOI fabrication techniques. In addition, designs are tested to validate the mechanical coupling mechanism.

In the second part of the thesis, a maskless laser writing system is developed for making polymer waveguides and other optical structures integrated with mechanical structures.

Keywords: Microscanner, mechanical coupling, electrostatic actuation, comb drive

ÖZET

MEMS (Mikro- Elektro- Mekanik- Sistemler) mikrotarayıcılar standart tarayıcılara göre ışık ışınlarını daha hassas ve hızlı yönlendirebilmek için kullanılmaktadır. Mikrotarayıcılar özellikle görüntüleme, haberleşme ve barkod okuma uygulamalarında kullanılmaktadır.

Bu tezde, elektrostatik kuvvet ile sürülen tarayıcılar için sistemin verimini arttırmak ve doğal salınım frekansında düşük voltaj ile yüksek genlikli hareket elde etmek için mekanik bağlaşım prensibini kullanan yeni bir metot sunulmuştur. Bu yöntemde, tarayıcının etrafına ikinci bir platform tanımlanmıştır ve elektrostatik kuvvet üreten tarak tahrikleyicileri (comb actuator) sadece dış platformda bulunmaktadır. İki boyutlu serbestlik derecesi olan sistemlerde (2-DoF), temel olarak tarayıcının geometrisi ve tarayıcı ile dışarıdaki platformu bağlayan yayın yay sabiti tarafından belirlenen mekanik bağlaşım frekansında, dış platformun genlik miktarı tarayıcıya sistemin mekanik bağlaşım katsayısı ile katlanarak iletilmektedir. Bu sistemin temel yararı, tarak tahrikleyicileri ile üretilen az miktardaki elektrostatik kuvvetin, bir boyutlu serbestlik derecesi olan sistemlere göre, tarayıcının daha yüksek genlikli hareketi için yeterli olmasıdır. Bu sistem, ayrıca doğrusal hareket (linear) modunda sürülen tarayıcılardaki yapışma (pull-in) problemini ortadan kaldırmak ve burulma (torsion) modunda sürülen tarayıcılardaki kayma hareketine (sliding) bağlı sönümleme etkisini azaltmak için de uygulanabilmektedir.

Mekanik bağlaşım katsayısına ve mekanik bağlaşım frekansına ait formüller çözümsel olarak elde edilmiştir. Sistemde yüksek genlikli hareket elde edebilmek için mekanik bağlaşım katsayısı bilgisayar destekli metotlarla da analiz edilmiştir. Burulma ve doğrusal hareket modlarında çalışan tarayıcılar tasarlanmış ve SOI (silicon- on- insulator) mikro-üretim teknikleri ile üretilmiştir. Ayrıca, tasarımlar test edilerek mekanik bağlaşım tekniği deneysel yollarla doğrulanmıştır.

Tezin ikinci bölümünde, polimer dalga kılavuzu üretmek için lazer ile maskesiz yazma sistemi geliştirilmiş ve optik yapılar ile mekanik yapılar entegre edilmiştir.

Anahtar Kelimeler: Mikrotarayıcı, mekanik bağlaşım, elektrostatik tahrikleme, tarak tahrikleyicileri

ACKNOWLEDGEMENTS

I would like to express my sense of gratitude to my thesis advisor Dr. Hakan Ürey for his patient guidance and encouragement. He supported me to improve myself in MEMS by combining my physics knowledge with engineering skills and expand my point of view. I would also like to thank Dr. Erdem Alaca and Dr. Yusuf Leblebici for attending my thesis committee. I also appreciate Koç University for the scholarship of my master of degree. I gratefully acknowledge our collaborator TÜBİTAK (The Scientific and Technological Research Council of Turkey) and Microvision. Inc, USA for their support. I would like to acknowledge Middle East Technical University for providing significant academic and social facilities during my undergraduate and my professors in the Physics Department.

I am thankful to my colleagues in Optical Microsystems Laboratory for sharing the experiences and knowledge as well as working in an enjoyable atmosphere. Specially, I would like to thank to Çağlar and Hüseyin for their contribution to my thesis.

Last, but not least, I would like to thank to my mom, dad and my sisters. I am deeply indebted to them for their moral support, trust and love.

TABLE OF CONTENTS

List of Tables XI

List of Figures XII

Nomenclature XX

Chapter 1: Introduction 1

1.1 Review of Silicon and Polymer Microscanners and Their Applications 2

1.2 Actuation of MEMS Scanners 7

1.2.1 Electrostatic Actuation 7

1.2.2 Electromagnetic Actuation 9

1.3 MEMS Stages for Scanning with Microlens Arrays 10

Chapter 2: Microfabrication and Operation of Comb Drive Scanners 15

2.1 Microfabrication of Linear and Torsional Scanners 15

2.2 Comb Drive Electrostatic Actuation 17

2.2.1 Actuation Principle and Modes of Operation 17

2.2.2 DC Pull- in Phenomena 22

2.3 Characterization of Comb Drive Scanners 24

Chapter 3: Mechanical Design with Coupled Actuation and Test Results..... 25

3.1 Introduction..... 25

3.2 Mechanical Coupling..... 26

3.3 1D in- Plane Sliding Mode Scanner Design..... 32

3.3.1 Numerical and Analytical Analyses..... 33

3.3.2 Experimental Results of the 1D In- plane Sliding Design..... 43

3.4 2D Sliding Mode Devices..... 47

3.5 Torsion Devices..... 51

3.5.1 FEM and Numerical Analyses of Torsion Devices..... 52

3.5.2 Experimental Results..... 57

Chapter 4: Voltage Stability and Damping Analysis for Torsional Scanners..... 59

4.1 Frequency Domain Characteristics of Torsion Scanners..... 59

4.2 Stability Analysis: Numerical and Experimental Results..... 63

4.3 Damping Analysis of Torsional Microscanners..... 68

4.3.1 Sliding Film Damping and Drag Force..... 68

4.3.2 Damping Analysis of the Torsional Devices and Comparison with Voltage Stability Results..... 72

4.4 Torsional Scanner Redesign Results..... 77

Chapter 5: Integration of Polymer Waveguides on FR4 Scanner 89

5.1 Polymer Waveguide and LED Array Integration on FR4 Scanner 89

5.1.1 FR4 Scanner 89

5.1.2 Waveguide Fabrication at Heriot Watt University and LED Array Integration on FR4 Scanner 90

5.2 Polymer Waveguide and Maskless Lithography Setup 95

Chapter 6: Conclusions 100

Appendix A 103

Bibliography 106

Vita 113

LIST OF TABLES

Table 3.1: Dimensions of D2HF2 34

Table 3.2: Dimensions of 2D linear devices 48

Table 3.3: Natural resonance frequencies of IP and OOP modes of *Design 2* obtained using MATLAB 50

Table 3.4: Dimensions of the fabricated torsional scanner 52

Table 4.1: Deflection amplitudes at IP- resonance mode 66

Table 4.2: Deflection amplitudes at OP- resonance mode 66

Table 4.3 Geometrical dimensions of the revised scanner 78

Table 4.4 Deflection amplitudes at the OP- resonance mode, low damping case (IP-mode quality factor=237, OP- mode quality factor=2325) 81

Table 4.5: Deflection amplitudes at the OP- resonance mode, high damping case (IP-mode quality factor=50, OP- mode quality factor=500) 81

Table 4.6: Deflection amplitudes for single frame scanner 81

LIST OF FIGURES

Figure1.1: Schematic drawing of the laser scanning display [2]. 3

Figure 1.2: Two DMD pixels [5] 3

Figure 1.3: SEM video images of operating DMD (left mirrors are-10º, ... 4

Figure 1.4: (a) Torsional microscanner with coils and magnets for a moving-coil actuator. (b) Nomad™ personal display system [6]. 4

Figure 1.5: Optical multiplexers (MUX/DEMUX) 5

Figure 1.6: Setup of the confocal laser scanning microscope [17]. 6

Figure 1.7: Schematic of the angular vertical comb (AVC) scanner [20]. 7

Figure 1.8: The basic electrostatic actuator: Parallel plate capacitor 8

Figure 1.9: General configuration of a moving coil torsional scanner 9

Figure 1.10: Microlens beam steering system [29] 11

Figure 1.11: Process flow of reflowed Cytop lenses. (a) Deposition of SiO2 on the silicon wafer. (b) Spin coating and patterning of Cytop to form cylinders on the oxide surface. (c) Thermal reflow of Cytop at 200 ◦C. (d) Patterning of the backside of wafer and dry plasma silicon etching to remove the silicon from the light path [30]. 12

Figure 1.12: 500 um diameter microlens fabricated monolithically with the MEMS scanner using reflow method. 13

Figure 1.13 Hot embossing process flow. a) The replication tool; a glass mould with refractive lens arrays. b) Silicon wafer with a ~20 um thick spun polymer layer on top. c) The wafer with the spun polymer is brought in contact with the glass mould under pressure at an elevated temperature. d) Silicon wafer with the replicated polymer lens arrays [33]. 14

Figure 1.14. (a) SEM picture of the fabricated Cytop microlens array. (b) 3D surface profile of the microlens array [33]..... 14

Figure 2.1: Microfabrication process of the linear MEMS scanners..... 15

Figure 2.2: (a), (b) Microscope pictures of 50 um thick 2D linear devices. (c) SEM picture of the 35 um length comb fingers with 20 um comb overlap..... 16

Figure 2.3: First torsional silicon scanner designed by Petersen utilizing two bottom electrodes [34]..... 17

Figure 2.4: Schematic diagram of comb drive actuator..... 18

Figure 2.5: 3D illustration of comb actuated MEMS scanner..... 19

Figure 2.6: Capacitance vs. Displacement modeling of the comb actuators using COMSOL© Multiphysics..... 20

Figure 2.7: Capacitance- displacement characteristics of the 1D linear scanner presented in the thesis (a) In- plane sliding mode (b) Out-of- plane sliding mode..... 21

Figure 2.8: Schematic diagram of the parallel plate actuators..... 22

Figure 2.9: Equilibrium curve of 1 DOF parallel- plate actuator [41]..... 23

Figure 3.1: 3D illustration of the linear and torsional devices actuated using mechanical coupling..... 26

Figure 3.2: Harmonic analysis: Frequency spectrum of 2- DoF systems. Mechanical coupling is obtained in (a) OP-mode (b) IP-mode..... 29

Figure 3.3: Numerical simulation result for mechanical coupling variation with frequency 31

Figure 3.4: 3D illustration of the 1D in-plane sliding device 33

Figure 3.5: 2D illustration of the 1D in- plane scanner and geometrical parameters 34

Figure 3.6: Modal analysis results of D2HF2 obtained using ANSYS 35

Figure 3.7: Harmonic analysis result of D2HF2..... 36

Figure 3.8: Transient analysis using MATLAB © ODE solver. (a) Deflection vs. Time at the IP- resonance mode. (b) Deflection vs. Time at the OP- resonance mode 36

Figure 3.9: Effects of the outer frame mass and outer flexure stiffness on (a) Inner frame deflection. (b) Mechanical coupling efficiency. 39

Figure 3.10: Effects of the outer frame mass and outer flexure stiffness on (a) coupling frequency (b) mechanical coupling efficiency..... 41

Figure 3.11: Frequency spectrum of the device with same inner frame dimensions..... 42

Figure 3.12: Mechanical coupling efficiency vs. quality factor at the OP- resonance mode 43

Figure 3.13: Driving of the comb actuated in- plane sliding devices with complementary biased signal. 44

Figure 3. 14: Microscope picture of the fabricated 1D comb actuated MEMS device (D2HF2). 45

Figure 3.15: Experimental result of frequency response at (a) IP- resonance mode (b) OP- resonance mode. (c) Frequency shift with voltage variation at the IP- resonance frequency, (d) Frequency shift with voltage variation at the OP- resonance frequency. 46

Figure 3.16: 3D illustrations of 2D linear devices 48

Figure 3.17: Harmonic analysis results of *Design 2* 49

Figure 3.18: Modal analysis results of *Design 2* is obtained using ANSYS simulation tool 50

Figure 3.19: 3D illustration of the torsional scanner actuated with mechanical coupling. The comb fingers are along the two edges of the outer frame. 51

Figure 3.20: ANSYS: FEA of the 1D torsional MEMS scanner 53

Figure 3.21: Stress analysis results in ANSYS 54

Figure 3.22: Frequency response of the fabricated torsional scanner 55

Figure 3.23: Transient analysis results at 2f excitation frequency (a) IP- resonance mode (b) OP-resonance mode 56

Figure 3.24: Experimentally obtained deflections at (a) IP- resonance mode, 58

Figure 4.1: Oscillation and excitation waveform. Solid line represents the square- wave excitation signal and dashed line represents the deflection waveform of the torsional scanner 62

Figure 4.2: Hysterical frequency response of torsional microscanners [49] 63

Figure 4.3: Typical voltage stability: Excitation voltage amplitude vs. frequency [50]..... 64

Figure 4.4: (a) Frequency response of the test device at the IP- resonance mode. (b) Frequency response of the test device at the OP- resonance mode 65

Figure 4.5: Voltage stability tongue for sample 1D torsional comb drive scanner at the OP- resonance mode..... 67

Figure 4.6: Sliding film damping between two infinite plates. (a) Stoke's flow model. (b) Laminar Couette flow model 69

Figure 4.7: Damping response of the scanner at OP- resonance mode 73

Figure 4.8: IP- resonance mode (a) Red lines represent the electrostatic work with respect to different drive voltages; blue line represents the dissipated work by air damping. (b) Blue line represents damping work found due to (4.22), red line represents the damping work calculated with respect to experimentally obtained quality factors (c) Fit function used to find the drag coefficient [Wyatt Davis, Microvision Inc. personal communication, 2008] 75

Figure 4.9: OP- resonance mode (a) Red lines represent the electrostatic work with respect to different drive voltages; blue line represents the dissipated work by air damping. (b)

Blue line represents damping work found due to (4.22), red line represents the damping work calculated with respect to experimentally obtained quality factors (c) Fit functions used to find the drag coefficient for plate and mirror. [Wyatt Davis, Microvision Inc. personal communication, 2008] 77

Figure 4.10: 3D illustration of the torsional scanner 78

Figure 4.11: Frequency response of the revised scanner performed using MATLAB simulation tool 79

Figure 4. 12 Modal and stress analyses results obtained using ANSYS. 80

Figure 4.13: 2D illustration of the comb actuated torsional scanner and the force in-equilibrium at the corner fingers 83

Figure 4.14 Pull- in problem due to the electrostatic force at the corner fingers 84

Figure 4.15: Pull in voltage analysis: a) V_{pi}=300 V with 5 um comb width and 160 um comb length, (b) V_{pi}=480 V with7 um comb width and 160 um comb length. (c) V_{pi}=90 V with 5 um comb width and 300 um comb length..... 85

Figure 4.16: Pull in voltages calculated with parallel plate assumption, red line represents the comb fingers with 160 um length and the black line represents the comb fingers with 300 um length 86

Figure 4. 17: Modeling of parallel plate capacitor..... 86

Figure 4.18: Cantilever beam under distributed load..... 87

Figure 5.1: Magnetically actuated FR4 scanner and the driving electro-coil. 90

Figure 5.2: LED array integrated FR4 scanner 91

Figure 5.3: The waveguide specifications mounted on top of the FR4 scanner 92

Figure 5.4 : UV light emitted by laser cures the polymer material..... 92

Figure 5.5: Waveguide integrated FR4 scanner is actuated with an external electro- coil. The waveguide is coupled only one LED in the array. 93

Figure 5.6: Torsion mode analysis of the polymer waveguide integrated FR4 scanner using ANSYS Software 94

Figure 5.7: (a) Top view of the waveguide. The bright spot closer to camera (bottom of picture) is the light output from the waveguide, the top bright spot is the reflection from the 45º mirror that is not guided (b)Scan line generated in torsion mode captured by directly imaging the output of the waveguide illustrating several mm edge deflection and rotation capability of the FR4 stage. 94

Figure 5.8: Maskless lithography setup 95

Figure 5.9: Microscope picture of (a) 58 um width, 5 mm length trench. (b) 125 um width, 5 mm length trench, (c) 136 um width, 5 mm length trench 97

Figure 5.10: Surface profile of (a) 65 um width, 5 mm length trench. (b) 125 um width, 5 mm length trench, (c) 136 um width, 5 mm length trench. 98

Figure 5.11: Microscope picture of 37 um width, 5 mm length waveguide. 98

Figure 5.12: Surface profile of 37 um width waveguide 99

Figure A.1: The characterizations setup of the microscanners (a) Measurement of the in-plane sliding device (b) Measurement of the torsional scanner..... 104

NOMENCLATURE

x_i	deflection amplitude of the inner frame
x_o	deflection amplitude of the outer frame
ω_i	natural resonance frequency of the inner frame
ω_o	natural resonance frequency of the outer frame
ω_{IP}	IP-mode resonance frequency
ω_{OP}	OP- mode resonance frequency
ω_D	frequency of the mechanical dip
F_{Ext}	total electrostatic created in the system
$F_{Di,}$ F_{Do}	damping force exerted on the inner and outer frame
M	mechanical coupling efficiency
θ_i, θ_o	mechanical scan angle (MSA) of the inner frame and the outer frame
MLA	microlens array
MMLA	movable microlens array
DMLA	double microlens array
PSL	prescan lens
f_{PSL}	focal length of the prescan lens
f_{MLA}	focal length of the microlens array
n	refractive index of the material
r_1	lateral displacement of the prescan lens
r_2	lateral displacement of the microlens array

Chapter 1

INTRODUCTION

Micro-Electro-Mechanical Systems (MEMS) technology combines electrical and mechanical components on the same platform to build microscopic machines. Accelerometers, microrobots, sensors, microactuators and micromirrors are some of the examples of MEMS devices. Micro-Opto-Electro-Mechanical Systems (MOEMS), also known as Optical MEMS is a new class of MEMS and used to sense or manipulate the optical signals by using micromechanical systems. Applications of MOEMS are mainly found in waveguides, microscanners and dynamic diffraction gratings. Advanced improvements in microfabrication techniques allow small size, low cost, fast speed and high resolution MOEMS scanners.

This thesis mainly deals with the comb actuated silicon microscanners which are modeled and developed for display and endoscopic imaging applications. 1D and 2D linear comb actuated scanners are fabricated to actuate the microlens arrays designed for an endoscopic laser camera system.

Main contributions of this thesis are proposing a novel actuation technique for comb actuated in-plane and out-of-plane scanners, numerical and analytical investigations and verification of the theoretical expectations with the experimental results. Also, torsional scanners are modeled and fabricated for laser scanning display applications. Another research area as part of this thesis was related to fabrication of polymer waveguides and integration of the waveguides with scanning platforms. FR4 based scanners were used for

easy integration of micro-optics and micromechanics. To give a general overview, applications of the silicon and polymer microscanners, fabrication details and the actuation mechanisms are discussed in Chapter 1 and Chapter 2. Chapter 3 describes the mechanical coupled actuation principle in detail and presents analytical, numerical, and experimental results. Chapter 4 discusses the dynamics of the electrostatic actuator and presents damping analysis. Chapter 5 discuss the polymer waveguides that are integrated with scanners and our own efforts to make waveguides on polymer substrates using a general purpose laser writing setup for maskless lithography developed as part of this thesis.

1.1 Review of Silicon and Polymer Microscanners and Their Applications

Microscanners are one of the most important MOEMS components and play an important role in display, imaging, telecommunication, barcode recognition and biomedical applications. Microscanners are mainly used for the mirror applications by depositing a reflective metal layer. Mostly aluminum or gold are used due to their high reflectivity. Today, microscanners are concerned to be used for refractive scanning for imaging applications. In this section, only reflective microscanners are discussed and refractive microscanners are explained in detail in Chapter 1.3. Main applications of the reflective microscanners are discussed below.

Display and Imaging: MOEMS scanners are charming devices for this application due to their high performance such as high frequency, large scan-angle, low response time and low power consumption. Microscanners are integrated with light sources like LED or laser sources to achieve high definition display and imaging systems (Figure1.1). Lasers are popular components of the display and imaging systems, since they have wider color gamut and emit monochromatic, coherent, small and straight beam of light [1-4].

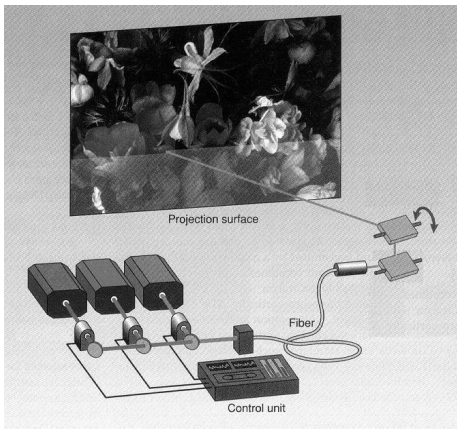

Figure1.1: Schematic drawing of the laser scanning display [2].

Most famous MOEMS scanner product is Digital Micromirror Device™ (DMD) developed by Texas Instruments©. DMD is designed for conference-room and classroom projection, high-performance home-theater systems and large auditorium projectors. DMD consists of an array of reflective light switches. The light switches are MEMS micromirrors and operate digitally and illustrated in Figure 1.2 and Figure 1.3. DMD micromirrors are coated with Al to increase the surface reflection and operate electrostatically [5].

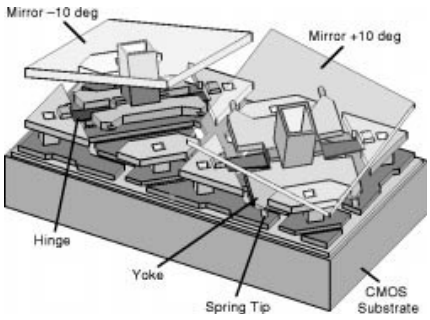

Figure 1.2: Two DMD pixels [5]

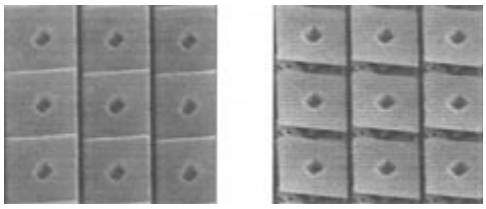

Figure 1.3: SEM video images of operating DMD (left mirrors are-10º, right mirrors are +10 º) [5].

Another display application of the MOEMS scanners is Retinal Scanning Display (RSD) which is developed by Microvision, Inc. [6, 7]. RSD creates a virtual image by raster scanning at the viewer's eyes using LED or laser and illustrated in Figure 1.4. Biaxial scanners are actuated electromagnetically that the metal coil is deposited on the scanner and the scanner is placed in a magnetic field generated by the permanent magnets.

(a) (b)

Figure 1.4: (a) Torsional microscanner with coils and magnets for a moving-coil actuator. (b) Nomad^{TM} personal display system [6].

Optical Switches in Telecommunication: Fiber optic cables are started to replace the copper electric wires since they are less expensive and thinner. Moreover, fast data transmission, lower signal attenuation and no crosstalk makes fiber optic systems more advantageous. Optical-cross-connect (OXC) switches are required to change the route of the light guided by fiber optic cable and illustrated in Figure 1.5 [8, 9].

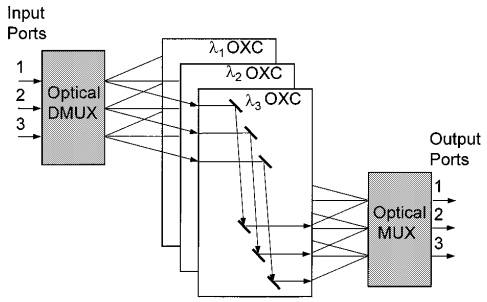

Figure 1.5: Optical multiplexers (MUX/DEMUX)
spatially separate the input optical beams by wavelength. Each wavelength
channel is routed to an independent N x N cross-connect [8]

Biomedical Applications: In recent years, MEMS devices, such as microsensors and microactuators have been widely used in biomedical applications both for diagnosis and therapy [10]. Mostly, MEMS scanners are used in optical coherence tomography (OCT) and confocal microscopes. Optical coherence tomography (OCT) is a sub-nanometer resolution, endoscopic imaging technique for the biological tissues [11, 12]. When the sample is scanned with the microscanners, since OCT is an interferometric technique, only reflected coherent light is collected for image formation and the scattered light is eliminated.

Similar to OCT, confocal microscopy is 3D, high resolution imaging technique which uses MEMS scanners for in- vivo imaging. The basic confocal microscopy setup is shown in Figure 1.6. Light emitted from the laser is filtered by a pinhole and then by the help of an objective lens, light is focused on the sample. Reflected light is again filtered by the second pinhole placed at the entrance of the detector. The pinhole is used to eliminate the out-of-focus light from the detector in order to increase the resolution. In recent studies, the pinhole is replaced by the single mode fiber optic cables. The MEMS scanner is utilized to scan the sample in x-y plane with high accuracy and stability, and effective in miniaturizing the system [13- 15]. The fiber optic approach offers advantages in terms of spatial resolution, flexibility, miniaturization and immunity to external influences. Confocal laser

microscopy ensures sharp imaging and able to image thick specimens by rejecting out-of-focus light [16].

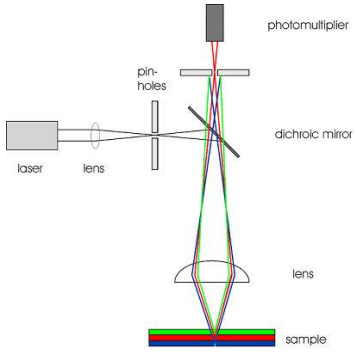

Figure 1.6: Setup of the confocal laser scanning microscope [17].

In addition to the silicon, polymer materials are used to fabricate the components of the MEMS scanners. PDMS (Poly-Di-Methyl-Siloxane) and SU-8 photoresists are well-known polymer materials used for fabricating hinges of the torsional scanners. Due to its high elasticity and high resistance, PDMS is suitable to fabricate hinges to have large angular deflection with low stress. Silicon and PDMS are used to fabricate hybrid structures to integrate the position sensors. PDMS is also preferred in comparison to silicon due to its low Young's modulus. Also, it is a UV cured polymer and it has very good resistance to the strong chemicals and high thermal stability [18]. SU-8 can be used as the scanner itself. In [19], cantilever beam is fabricated by SU-8 and the magnetic material, Nickel, is deposited to actuate the cantilever by external magnetic field. Low Young's modulus of SU-8 results in low stress during bending of the cantilever. Polymer materials are also used in offset comb fabrication. In this type of scanners, offset comb fingers can be fabricated with different techniques. One of the techniques is angular vertical comb drive microscanner [20] and the scanner is shown in Figure 1.7. The self- aligned comb drives are fabricated with single etch of the SOI wafer. A rectangular portion is etched from the silicon and

filled by a thermoplastic polymer material which provides the required surface tension force.

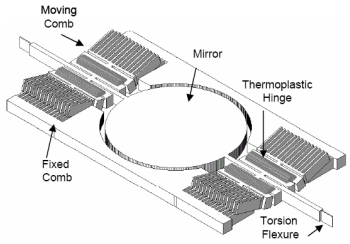

Figure 1.7: Schematic of the angular vertical comb (AVC) scanner [20].

Moreover, in Optical Microsystems Laboratory, a novel polymer scanner is developed using FR4 material. This work is discussed in detail in Chapter 5.

1.2 Actuation of MEMS Scanners

Different actuation mechanisms are utilized in microscanners such as electrostatic, electromagnetic, piezoelectric and thermal actuation. Common purpose of these methods is converting the input energy to the mechanical motion with maximum efficiency. Thermal actuators have long response time in comparison to other methods and piezoelectric actuation requires high voltages and has hysteresis problem [21].

1.2.1 Electrostatic Actuation

Electrostatic actuation principle depends on the capacitance variation between the conducting electrodes separated by a dielectric medium. Figure 1.8 illustrates the parallel plate capacitors.

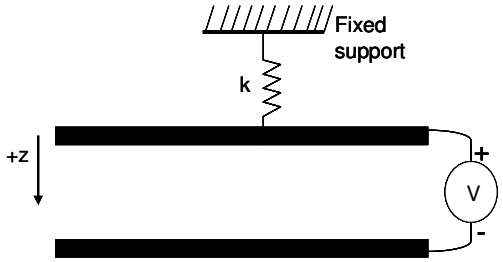

Figure 1.8: The basic electrostatic actuator: Parallel plate capacitor

When voltage is applied, conducting electrodes are charged with opposite sign and energy stored in the system is proportional to the capacitance between the conducting plates. Capacitance of the movable parallel plate capacitor and the stored energy are illustrated in the equations 1.1 and 1.2.

$$C = \varepsilon \frac{A}{d} \tag{1. 1}$$

$$W = \frac{1}{2} C V^2 \tag{1. 2}$$

where C is the capacitance, V is the drive voltage, ε is permittivity of the dielectric material between the plates, A is the plate area and d is the gap between the plates. Generated attractive force is given as:

$$F_{Elec} = \frac{\partial W}{\partial z} = \frac{1}{2} \frac{dC}{dz} V^2 \tag{1. 3}$$

Electrostatic actuation is a simple method and offers many advantages for MEMS scanners such as fast response time, low power consumption in both resonant and quasistatic operation, low cost and small size. In addition to these advantages, electrostatic actuation technique has important disadvantages like electrostatic instability and non-linearity [22].

Comb actuators are the main actuator type used in this thesis and discussed in detain in Chapter 2.2.

1.2.2 Electromagnetic Actuation

Electromagnetic actuation can take place with moving coil, moving magnet or Permalloy thin- film actuators [23, 25]. Electromagnetic actuation can be driven with relatively smaller drive voltages compared to electrostatic actuation, but may require higher currents. In moving coil electromagnetic actuation, as illustrated in Figure 1.9, the coil is deposited on the scanner and placed in the external magnetic field generated by the permanent magnet. Current passes through the coil results in an electromagnetic force consequently in mirror rotation. In the second type of the electromagnetic actuation, the permanent magnet is integrated on the scanner and the external magnetic field is exerted by the electro-coil. The Permalloy thin-film actuation method is illustrated in [25]. A cantilever beam is electroplated with a very thin Permalloy layer and the external magnetic field is generated by the coil driven with an AC signal and produces a magnetic field. The field magnetizes the thin- Permalloy film and generates a net torque which actuates the cantilever at its resonant mode. In this method, the magnetic film layer is modeled as an array of permanent magnets.

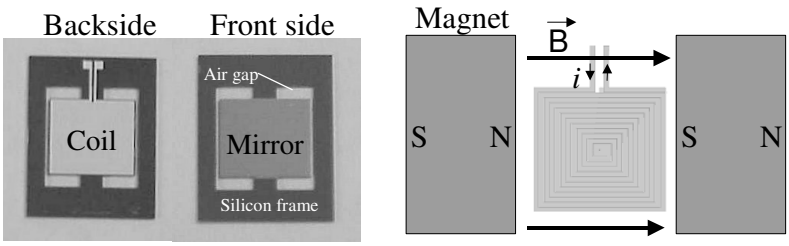

Figure 1.9: General configuration of a moving coil torsional scanner

1.3 MEMS Stages for Scanning with Microlens Arrays

In different laser scanning applications, mostly mirror- based MEMS scanners are used for beam scanning and steering. However, since reflective scanning requires beam folding, scanner can not fit into a small area. To eliminate this limitation, instead of reflective beam scanning, refractive systems can be built using lenses. Beam scanning can be achieved by 4-f scanning technique which consists of two in-plane moving identical lenses separated by two focal lengths. Scanning with single lenses brings important drawbacks into the system such as slow scanning and optical aberrations. Also, with the single lens actuation, large angular deflection is hard to achieve. Instead of single lenses, scanning microlens arrays (MLA) offers many advantages such as larger deflection angles, less optical aberrations and better resolution. Moreover, microlens arrays are lighter and better scan speed can be obtained.

Comb actuated 1D and 2D linear scanners are designed and modeled for the endoscopic laser scanning camera for in- vivo imaging. Main advantages of the system will be wider field of view and higher resolution. There are different endoscopic imaging techniques which use MEMS scanners with confocal microscopy [26] and optical coherence tomography [27]. 1D in- plane linear MEMS scanners are designed to scan the refracted light and increase the field of view of the camera. 2D linear scanners are designed for focus adjustment of the microlenses, as well. For focus adjustment, different than our approach, dynamic focusing can be achieved by tunable liquid microlenses as discussed in [28].

Due to the periodic structure of MLA, diffraction of the system limits the number of addressable points. Only specific angles can be addressed where constructive interference is satisfied. The three-MLA beam steering system is illustrated in Figure 1.10. While the first MLA is moving, second and third MLAs are combined and named as double- MLA (DMLA). Two microlens arrays of DMLA must be separated with $n.f_{MLA}$ where n is the refractive index of the material. The discrete addressing problem is solved by using a

movable prescan lens in the system. r_1 and $r_{2,}$ in the figure, shows the lateral displacement of the prescan lens and MLA, respectively. [29] The movable components must be actuated accurately and fast enough to solve the discrete addressing problem that is why the comb actuated MEMS scanners are designed and modeled in this thesis.

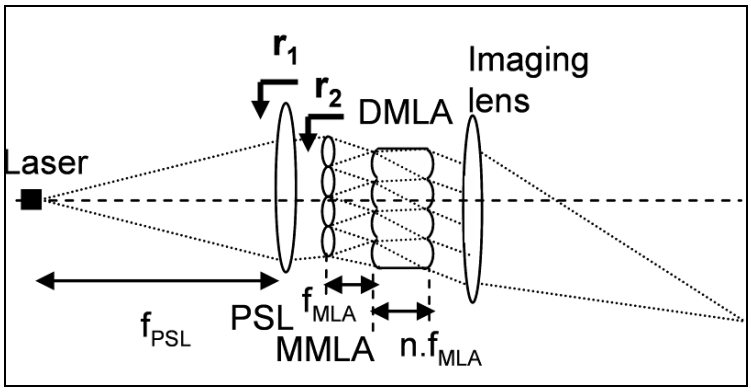

Figure 1.10: Microlens beam steering system [29].

In the literature, different methods are used to fabricate microlens arrays such as reflow techniques, replication, micro-jet printing, gray- scale lithograph and direct writing with laser or electron beam [30, 31]. Through these methods, only thermal reflow and replication methods are used for fabrication of the microlens arrays integrated with the comb actuated MEMS stages.

Standard integrated circuit (IC) techniques and equipments are used for thermal reflow process; consequently the process is compatible with the MEMS fabrication procedures. Different type of photoresists [30, 32], doped amorphous Teflon and solgel can be used for thermal reflow method. However, photoresists are not preferred due to their low environmental stability. In our microlens array fabrication processes, Cytop (fluorocarbon polymer) is used with both thermal reflow and hot embossing techniques by Çaglar Ataman Sven Holmstrom from Koç University and Karin Hedsten in Chalmers Technical University, Sweden. Cytop is a polymer material with good environmental stability,

chemical resistance and optical properties. Most significant property of Cytop is its high transmittance (>95) for wavelengths from 200 nm to 1900 nm [30]. Fabrication steps of the thermal reflow process are shown in Figure 1.11.

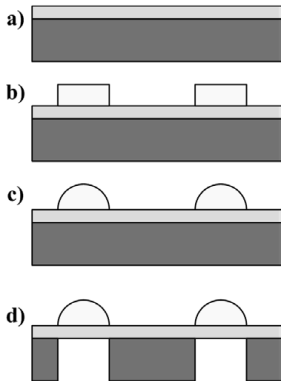

Figure 1.11: Process flow of reflowed Cytop lenses. (a) Deposition of SiO2 on the silicon wafer. (b) Spin coating and patterning of Cytop to form cylinders on the oxide surface. (c) Thermal reflow of Cytop at 200 ◦C. (d) Patterning of the backside of wafer and dry plasma silicon etching to remove the silicon from the light path [30].

In the first step, Cytop is spin coated onto silicon dioxide substrate. In the next step, Cytop is patterned to form cylindrical shapes and in the following step, the wafer is heated up to 200 ºC. After heating process, polymer cylinders form the near-spherical microlenses as a result of the surface tension. At the last step, microlenses are cooled to room temperature. Microlenses are successfully fabricated monolithically with 1D linear MEMS scanners using thermal reflow method (Figure 1.12). However, at the last step of the microfabrication, stages carrying the microlenses are damaged and released devices could not be obtained.

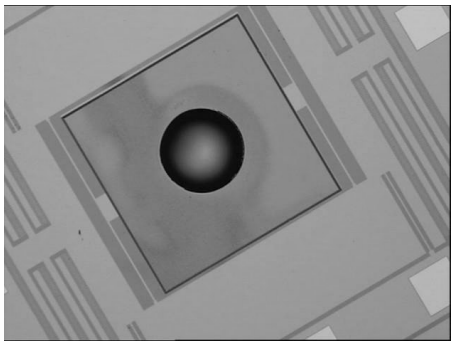

Figure 1.12: 500 um diameter microlens fabricated monolithically with the MEMS scanner using reflow method.

In the second fabrication run, hot embossing replication method is used with Cytop polymer. A wafer bonding machine is used with a transparent mold. Fabrication steps are illustrated in Figure 1.13. Quartz mould is fabricated using isotropic etching by Microvision, Inc., USA. As seen in Figure 1.13 (a), lens arrays are isotropically etched and in order to separate the mold from the polymer at the end of the process, a release agent is deposited on the interior surfaces of the mold. 20 um Cytop is spun on the silicon wafer and precured in the oven. In the next step, quartz mould is compressed on the Cytop coated wafer. At the final step, mould is separated from the wafer [33].

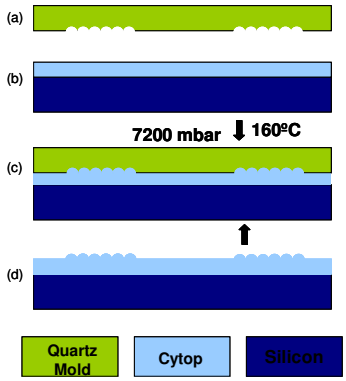

Figure 1.13 Hot embossing process flow. a) The replication tool; a glass mould with refractive lens arrays. b) Silicon wafer with a ~20 um thick spun polymer layer on top. c) The wafer with the spun polymer is brought in contact with the glass mould under pressure at an elevated temperature. d) Silicon wafer with the replicated polymer lens arrays [33].

In our fabrication process, polymer microlens arrays are fabricated monolithically with 1D linear MEMS scanner. However, at the last step of the fabrication process, despite a release agent is utilized, adhesion was too much to separate the mold from the surface. Another problem was high pressure requirement of the microlens fabrication. Despite all the limitations, still, successfully fabricated microlens arrays are obtained and shown in Figure 1.14. Radius of curvature and the focal length of the fabricated microlenses are measured ~130 um and 300 um, respectively.

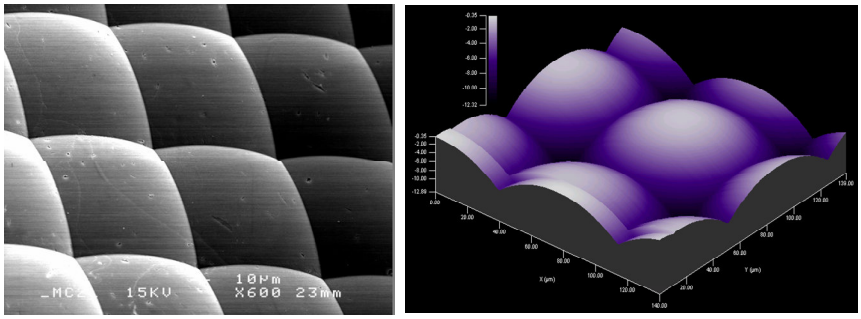

(a) **(b)**

Figure 1.14. (a) SEM picture of the fabricated Cytop microlens array. (b) 3D surface profile of the microlens array [33]

Chapter 2

MICROFABRICATION AND OPERATION OF COMB DRIVE SCANNERS

2.1 Microfabrication of Linear and Torsional Scanners

As discussed in the previous chapter, microlens fabrication is successfully achieved on 1D MEMS scanner and two microlens fabrication methods are covered in detail. Despite 2D linear scanners are fabricated, microlens integration process is postponed to another fabrication run due to time limitations. Fabrication steps of the lensless linear devices are same with the torsional devices and shown in Figure 2.1. Note that, fabrication process of the torsional devices includes two more steps to form the mirror with metallization.

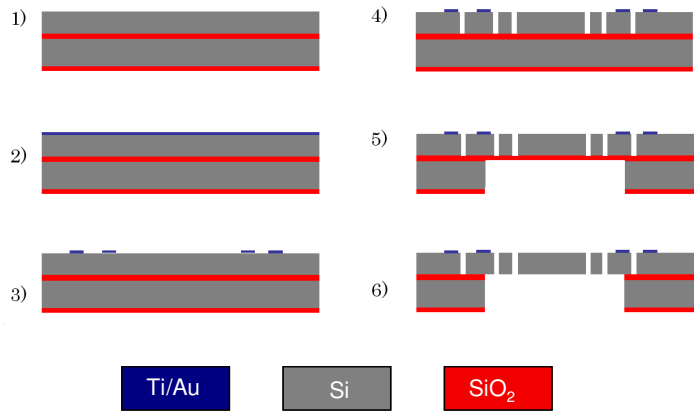

Figure 2.1: Microfabrication process of the linear MEMS scanners

The fundamental steps of the fabrication steps of the linear devices are:

1. 20 um or 50 um SOI wafer,
2. Definition of the wire-bond electrodes: Ti/Au metal layers (20 nm/120 nm),
3. Patterned wire- bond electrodes,
4. Structural elements are defined through a DRIE step,
5. Backside DRIE etching,
6. Release of the device.

Microscope and SEM pictures of the fabricated devices are presented in Figure 2.2.

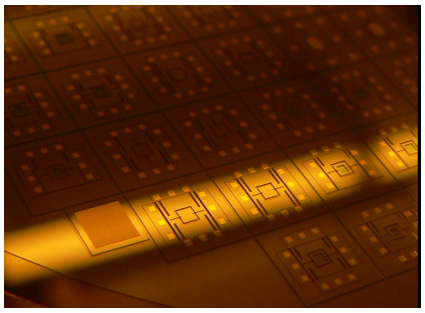

(a)

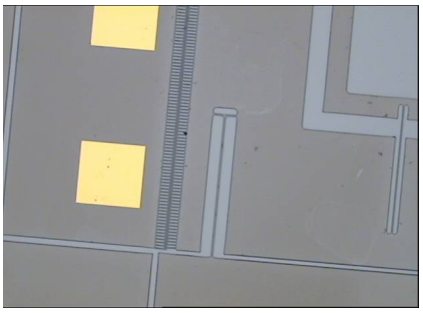

(b)

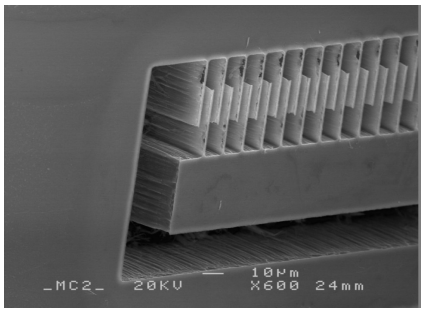

(c)

Figure 2.2: (a), (b) Microscope pictures of 50 um thick 2D linear devices. (c) SEM picture of the 35 um length comb fingers with 20 um comb overlap

2.2 Comb Drive Electrostatic Actuation

2.2.1 Actuation Principle and Modes of Operation

Early electrostaticly actuated scanners are mainly actuates with electrodes placed underneath the mirror [34] and illustrated in Figure 2.3. These devices require high voltages (several 100 V) [35]. In order to decrease the required driving voltage, comb fingers are presented instead of parallel plate electrodes as they can provide much larger capacitance variation. Therefore, larger deflection amplitudes are obtained with reduced voltages.

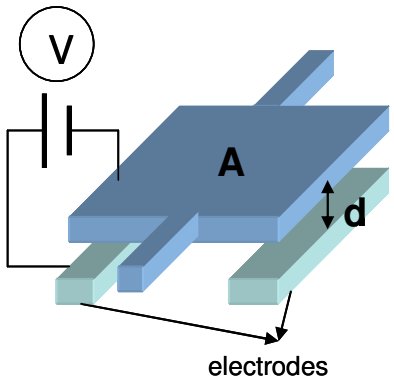

Figure 2.3: First torsional silicon scanner designed by Petersen utilizing two bottom electrodes [34]

Comb drive actuators find applications in linear and torsional actuation, such as accelerometers [36], gyroscopes [37] and RF resonators and filters [38].

The geometrical structure of the comb drive actuators is illustrated in Figure 2.4. When the voltage difference is applied to the actuator, an electrostatic force (torque) is generated between the comb fingers and for the N comb fingers, the total electrostatic force (F) and torque (M) along the deflection are defined as:

$$F_{Elec} = \frac{\partial W}{\partial z} = N\frac{1}{2}\frac{dC}{dz}V^2$$
$$M_{Elec} = \frac{\partial W}{\partial \theta} = N\frac{1}{2}\frac{dC}{d\theta}V^2 \quad (2.1)$$

where z is the linear displacement for translatory linear modes, θ is the angular displacement of the torsional modes and V is the applied drive voltage. The capacitance (C) is calculated using;

$$C_1 = \varepsilon\frac{L_{overlap}t}{g_1}$$
$$C_2 = \varepsilon\frac{wt}{g_2} \quad (2.2)$$

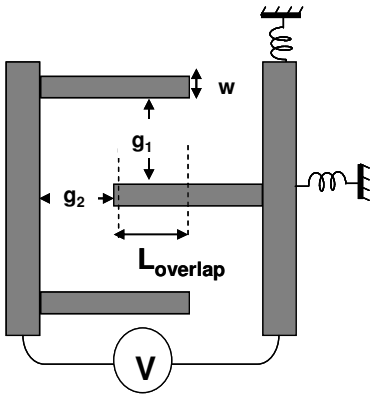

Figure 2.4: Schematic diagram of comb drive actuator.

where, g_1 and g_2 are the gap between the adjacent and complementary comb fingers. $L_{overlap,}$ w and t are the overlapping length, width and thickness of the fingers, respectively.

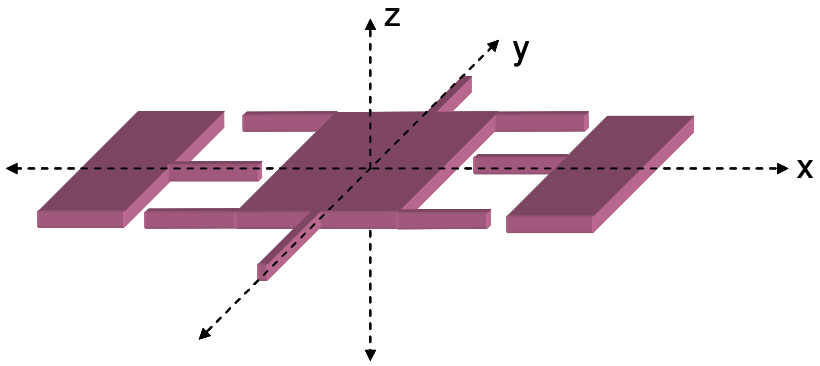

Figure 2.5: 3D illustration of comb actuated MEMS scanner

To find the generated electrostatic force or torque, capacitance change with respect to the linear or rotational deflection must be found. In this thesis, only out- of- plane sliding (translation along the z-axis), in- plane sliding (translation along the x-axis) and torsion modes (rotation around the y-axis) are investigated and their capacitance variations are modeled (Figure 2.5). Fundamental vibration modes and the analytical formulae are illustrated in [39]. In order to find the deflection amplitude of the designed scanners, capacitance variation of the comb actuators are modeled in COMSOL© Multiphysics (Figure 2.6) and the capacitance- displacement plots of in-plane sliding and out-of-plane sliding vibration modes are shown in Figure 2.7.

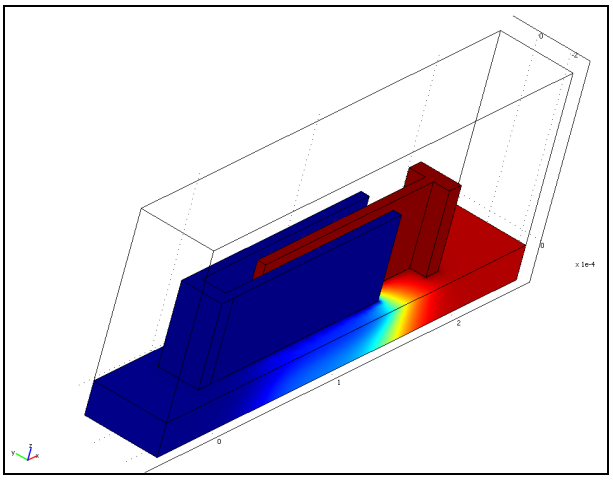

Figure 2.6: Capacitance vs. Displacement modeling of the comb actuators using COMSOL© Multiphysics

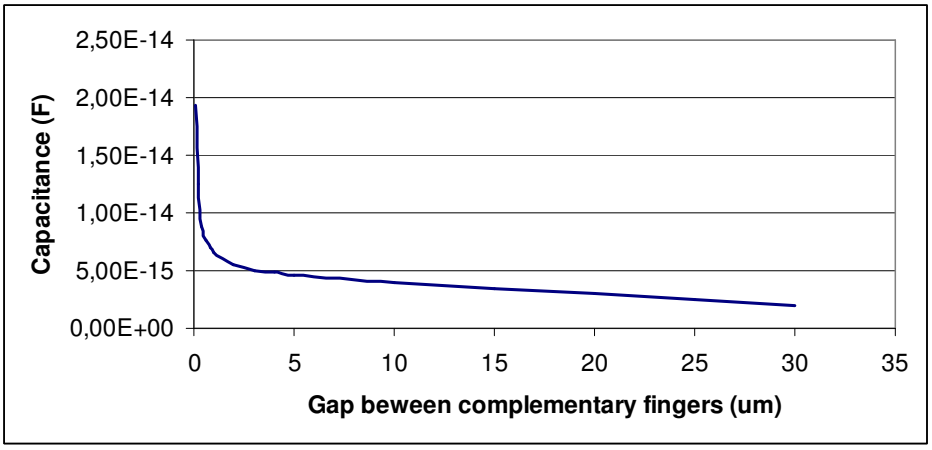

(a)

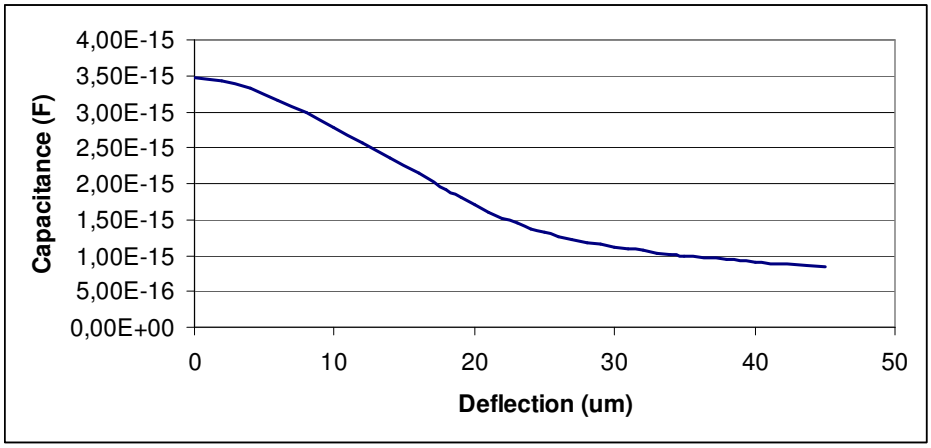

(b)

Figure 2.7: Capacitance- displacement characteristics of the 1D linear scanner presented in the thesis (a) In- plane sliding mode (b) Out-of- plane sliding mode

As seen in Figure 2.7 (a), in the in-plane sliding mode, the capacitance goes to very high values when the gap, denoted by g_2 (Figure 2.4) is very small. When the fingers start to disengage, the capacitance between the adjacent comb fingers is dominant and decreases linearly with decreasing the comb overlap. Due to the dynamic pull-in issue, in plane devices can not work in the non- linear region where g_2 is too small. So that, the capacitance variation and the electrostatic force of the in- plane sliding devices is independent of the displacement. Figure 2.7 (b) illustrate the capacitance variation characteristic of the out- of- plane sliding mode. Capacitance variation of the out- of- plane sliding mode and the torsional mode are similar. Both vibration modes have displacement dependent electrostatic force (torque) and their governing second order equations are non-linear [40].

2.2.2 DC Pull- in Phenomena

Pull- in phenomenon occurs at the voltage- controlled parallel plate electrostatic actuators when the electrostatic force generated by the voltage exceeds the elastic restoring force exerted by the moving plate. Mainly, devices oscillates at the in- plane sliding and the in- plane rocking modes can suffer from the pull- in problem. In the in- plane sliding mode, pull in can be modeled as parallel plate actuators as illustrated in Figure 2.8.

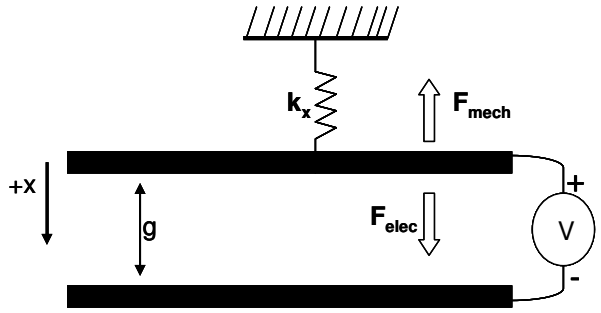

Figure 2.8: Schematic diagram of the parallel plate actuators

Net force exerted by the upper plate is given as:

$$F_{net} = F_{elec} - F_{mech} \tag{2. 3}$$

$$F_{elec} = \frac{\varepsilon A}{2g^2} V^2 \quad , \quad F_{mech} = k(g_0 - g) \tag{2. 4}$$

$$F_{net} = \frac{\varepsilon A}{2g^2} V^2 - k(g_0 - g) \tag{2. 5}$$

where A is the plate area, g is the gap, V is the driving voltage and g_0 is the initial gap between the plates.

Equilibrium states of the system are found using:

$$F_{net} = 0 \tag{2. 6}$$

In order to find the pull- in state, stability of the equilibrium states must be found by determining the behavior of the system when a small perturbation force (δF_{net}) is applied.

$$U = \frac{\delta F_{net}}{\delta x} \tag{2. 7}$$

When U=0, the equilibrium state is critically stable and the static pull-in occurs with the pull- in voltage denoted by V_{pi}. The equilibrium state is stable when U<0 and unstable when U>0. Above V_{pi}, the system has no equilibrium, however, below V_{pi}, the system has one stable and one unstable equilibrium states. The equilibrium curve of the parallel plate capacitor is shown in Figure 2.9.

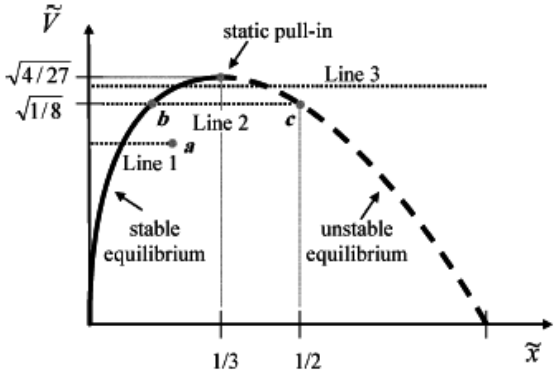

Figure 2.9: Equilibrium curve of 1 DOF parallel- plate actuator [41].

DC pull- in occurs at $g = \frac{2}{3} g_0$ and using U=0, the pull- in voltage can be expressed as;

$$V_{pi} = \sqrt{\frac{8kg_0^{\,3}}{27\varepsilon A}} \tag{2. 8}$$

2.3 Characterization of Comb Drive Scanners

An optical characterization setup is built to find the deflection amplitude and the phase of the microscanners. Characterization of 1D linear and torsional scanners are performed using knife edge technique and Laser Doppler Vibrometry, respectively. In APPENDIX A, characterization setup is discussed in detail.

Knife edge technique is used to find the deflection of the devices in the in- plane sliding vibration mode and presented in [42]. A Gaussian beam is focused on the edge of the device and the reflected light is collected by the detector during the oscillation. Device surface should be reflective to collect the returning light on the detector.

Laser Doppler Vibrometry (LDV) is an efficient technique to measure the deflection amplitude at the out- of- plane mode and utilizes the light reflected or scattered from the device surface. A torsional microscanner can be characterized using the LDV by focusing the laser especially on the edge of the scanner since the points on the microscanner do not oscillate with same velocity in the torsional mode.

Chapter 3

MECHANICAL DESIGN WITH COUPLED ACTUATION AND TEST RESULTS

3.1 Introduction

Comb drive electrostatic actuators are discussed in Chapter 2. Larger deflection amplitudes can be obtained with comb drive actuators at lower voltages.. However, for large deflection at high frequencies, comb drive MEMS actuators still require high voltages. Therefore, in this thesis a novel actuation mechanism is proposed in order to overcome this limitation. This method is not only beneficial for dealing with the high voltage problem, but also useful to decrease the damping losses in the system. Damping power losses can be quite large in comb actuated structures resulting in small deflections particularly for torsional devices at high frequencies.

Figure 3.1 illustrates the basic structure of the novel actuation principle proposed in this thesis. An additional outer frame is defined around the inner frame. Electrostatic comb drive actuators are only present on the outer frame. Small deflection of the outer frame is transferred to the inner frame mechanically with a mechanical coupling efficiency.

For in- plane devices, this novel method is also advantageous to eliminate the pull- in problem. In single frame MEMS platforms, to achieve large in- plane deflection, the gap between the tip of the comb fingers and the frame must be large enough to prevent pull- in. So that, in order to keep the same electrostatic energy in the system with conserving the comb overlaps, finger length must be increased. However, using the mechanical coupling method, relatively shorter comb fingers are sufficient to obtain a large deflection at the inner frame. In the torsional scanners, mechanical coupling method results in less sliding

film damping at the comb fingers, since the comb fingers deflect less in comparison to the structures with single frame.

Different 1D and 2D linear and 1D torsional scanner designs with various dimensions are modeled and fabricated on 20µm and 50 um SOI wafers using a simple fabrication process at Chalmers Technical University, Sweden by Çaglar Ataman and Sven Holmstrom in collaboration with Prof. Enokson's group. However, analytical and numerical analyses of only one design for each type of the scanners are presented in this thesis.

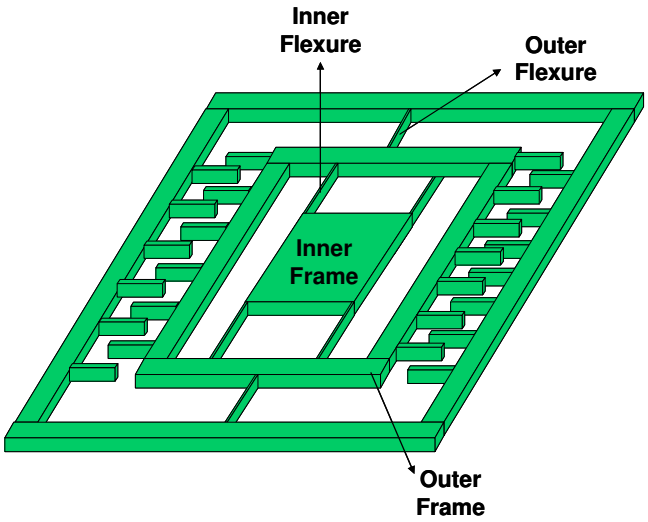

Figure 3.1: 3D illustration of the linear and torsional devices actuated using mechanical coupling

3.2 Mechanical Coupling

Mechanical coupling efficiency of the comb drive scanners is defined as the ratio of the peak inner and outer frame deflections and denoted by x_i and x_o, respectively and is dependent on vibration frequency. Unlike the single frame scanners, 2-Dof (Degree-of-freedom) systems have two natural resonance frequencies at each fundamental vibration modes. At the lower vibration frequency, the inner and outer frames moves in-phase (referred as IP), while at the higher vibration frequency, the motion of the frames is out- of-

phase (referred as OP). The lower vibration mode (IP-mode) and higher vibration mode (OP- mode) resonance peaks are defined by the mass and spring constant of the frames and the flexures. Depending on the required oscillation frequency, mechanical coupling can be obtained at either of the resonance frequencies of the system defined by the system parameters. Comparing the motion amplitudes at the coupling frequency shows that a small movement of the outer frame is coupled into and amplified at the inner frame. The amplification factor, the *mechanical coupling efficiency* is related to the stiffness and mass of the inner and outer frames and denoted by M (x_i/x_o) [43- 45].

The equation of motion of the electrostatically actuated two body MEMS platform can be derived via Euler- Lagrange (E-L) method [43]:

$$L = T - V \tag{3. 1}$$

where *L* is the Lagrangian, and *T* and *V* are the kinetic and potential energies in the system, respectively.

Kinetic energy can be expressed as:

$$T = \frac{1}{2} m_i \dot{x}_i^{\,2} + \frac{1}{2} m_t \dot{x}_o^{\,2} \tag{3. 2}$$

Potential energy can be expressed as:

$$V = \frac{1}{2} k_i (x_i - x_o)^2 + \frac{1}{2} k_o x_o^{\,2} \tag{3. 3}$$

L is then given by:

$$L = \frac{1}{2}\left(m_i \dot{x}_i^{\,2} + m_t \dot{x}_o^{\,2} - k_i (x_i - x_o)^2 - k_o x_o^{\,2} \right) \tag{3. 4}$$

where *k* is the spring constant associated with inner and outer flexures. The subscripts 'i' and the subscript 'o' denote the inner and the outer frames. m_i is the inner frame mass and the m_t is the total mass including inner and outer frames. The viscous damping factor of the inner and the outer frame are defined as b_i and b_o. While F_{Ext} is the total electrostatic force created at the comb fingers, F_{Di} and F_{Do} are the damping force exerted on the inner and outer frames, respectively.

$$\frac{d}{dt}\left(\frac{\partial L}{\partial \dot{x}_i}\right) - \frac{\partial L}{\partial x_i} = 0 - F_{Di} \tag{3. 5}$$

$$\frac{d}{dt}\left(\frac{\partial L}{\partial \dot{x}_o}\right) - \frac{\partial L}{\partial x_o} = F_{Ext} - F_{Do} \tag{3. 6}$$

$$\frac{\partial L}{\partial x_i} = -k_i(x_i - x_o), \quad \frac{\partial L}{d\,\dot{x}_i} = m_i \dot{x}_i, \quad \frac{\partial L}{\partial\, \dot{x}_o} = m_t \dot{x}_o, \quad \frac{\partial L}{\partial x_o} = k_i(x_i - x_o) - k_o x_o \tag{3. 7}$$

The equations of motion of the system are written as follows:

$$m_i \ddot{x}_i + k_i(x_i - x_o) = 0 - b_i \dot{x}_i \tag{3. 8}$$

$$m_t \ddot{x}_o + k_i(x_o - x_i) + k_o x_o = F_{Ext} - b_o \dot{x}_o \tag{3. 9}$$

Frequency spectrum of the system, shown in Figure 3.2 is obtained numerically with MATLAB©, using the equations 3.8 and 3.9. The IP- and OP-resonance frequencies and the mechanical coupling are illustrated in the figure.

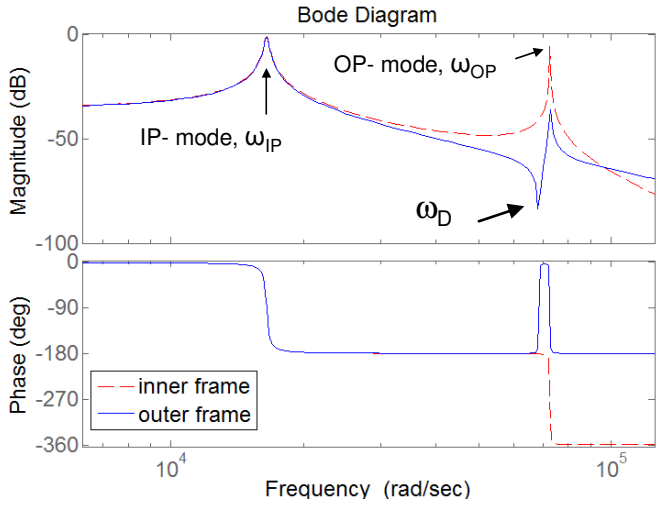

(a)

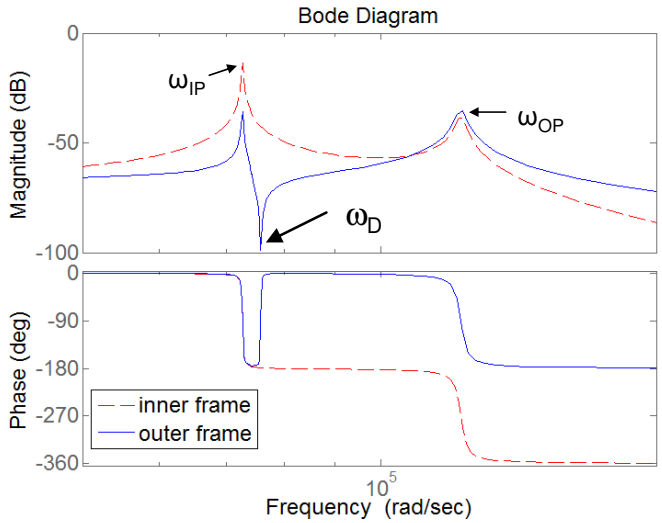

(b)

Figure 3.2: Harmonic analysis: Frequency spectrum of 2- DoF systems. Mechanical coupling is obtained in (a) OP-mode (b) IP-mode.

The outer and inner frame deflections can be solved in the Laplace domain for this linear system:

$$m_i X_i(s)s^2 + b_i X_i(s)s + k_i(X_i(s) - X_o(s)) = 0 \tag{3. 10}$$

$$m_t X_o(s)s^2 + b_o X_o(s) + k_i(X_o(s) - X_i(s)) + k_o X_0(s) = F_{ext} \tag{3. 11}$$

$$\frac{X_o(s)}{F_{Ext}} = \frac{m_i s^2 + b_i s + k_i}{((m_t s^2 + b_o s + k_i + k_o)(m_i s^2 + b_i s + k_i) - k_i^2)} \tag{3. 12}$$

$$\frac{X_i(s)}{F_{Ext}} = \frac{k_i}{((m_t s^2 + b_o s + k_i + k_o)(m_i s^2 + b_i s + k_i) - k_i^2)} \tag{3. 13}$$

Setting s= jω for steady-state frequency domain analysis, the *mechanical coupling efficiency M* can be calculated as;

$$M = \left|\frac{X_i(s)}{X_o(s)}\right| = \left|\frac{X_i(jw)}{X_o(jw)}\right| = \frac{k_i}{\sqrt{(k_i - m_i\omega^2)^2 + (b_i\omega)^2}} \tag{3. 14}$$

where ω is the oscillation frequency of the frames.

The natural frequencies of the inner frame and the outer frame acting alone (i.e., the set of flexures suspending the other frame is considered infinitely stiff) denoted by ω_i and ω_o, given as:

$$\omega_i = \sqrt{\frac{k_i}{m_i}} \text{ and } \omega_o = \sqrt{\frac{k_o}{m_t}} \tag{3. 15}$$

Figure 3.3 shows the frequency dependence of the mechanical coupling efficiency. Maximum mechanical coupling efficiency is obtained at the frequency where the outer frame has a mechanical zero. This dip frequency, denoted by $\omega_{D,}$ is equal to the resonance frequency of the inner frame (Figure 3.2) and does not change with dimensions of the outer frame. Mechanical coupling efficiency is equal to the quality factor of the coupling mode at this valley. At the dip frequency, despite maximum mechanical coupling efficiency is obtained, phase difference between the inner and the outer frame motion is 90º and outer frame deflection is not large enough to create sufficient electrostatic force.

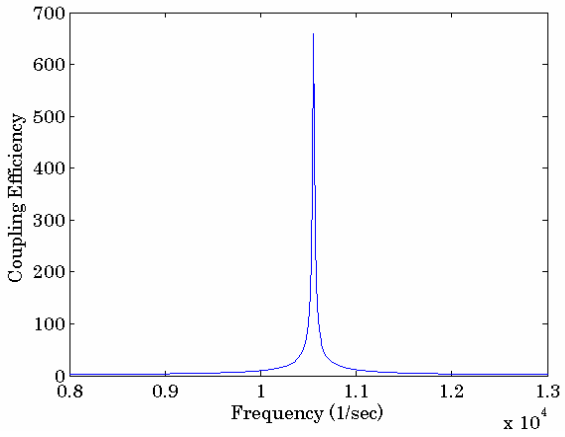

Figure 3.3: Numerical simulation result for mechanical coupling variation with frequency

The IP- and OP- resonance frequencies of the system can be solved and represented by ω_{IP} and ω_{OP};

$$\omega_{IP}{}^2 = \frac{k_i}{2m_t} + \frac{\omega_o{}^2}{2} + \frac{\omega_i^2}{2} - \frac{\sqrt{-4k_ik_om_im_t + (k_om_i + k_im_i + k_im_t)}}{2m_im_t} \tag{3. 16}$$

$$\omega_{OP}{}^2 = \frac{k_i}{2m_t} + \frac{\omega_o{}^2}{2} + \frac{\omega_i^2}{2} + \frac{\sqrt{-4k_ik_om_im_t + (k_om_i + k_im_i + k_im_t)}}{2m_im_t} \tag{3. 17}$$

Equation 3.16 and 3.17 are used to define the device dimensions in order to achieve maximum mechanical coupling efficiency. Despite higher mechanical coupling efficiency can be obtained when the inner frame resonance frequency approaches to the coupling frequency, since the outer frame doesn't move or moves very little at that frequency, the inner frame deflections would be very small. It is important to note that the system should be optimized to obtain the largest deflection at the inner frame, not to obtain the maximum mechanical coupling efficiency. This will be discussed in more detail subsequently.

3.3 1D in- Plane Sliding Mode Scanner Design

3D illustration of the 1D in- plane MEMS stage design is shown in Figure 3.4. The inner frame is connected to the outer frame with four flexures and outer frame is connected to the Si substrate with four flexures. Different 1D in-plane designs are fabricated and tested during this study. The designs differ in their inner frame forms and in their dimensions. Mainly two different 1D scanner forms are fabricated. Designs with solid inner frame are fabricated in order to integrate the SOI fabrication process for the MEMS stage with a monolithic microlens array process to fabricate microlens arrays (MLA) on MEMS stages for refractive scanning. The main application is beam steering for endoscopic imaging applications that require deflections on the order of the diameter of a single microlens in the microlens array for full-angle beam steering [29]. Other scanner form has hallow inner frame which is designed to investigate the contribution of the stage mass to the mechanical coupling mechanism.

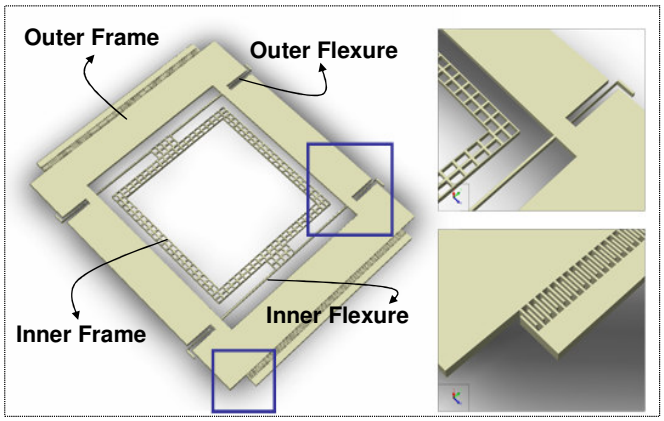

Figure 3.4: 3D illustration of the 1D in-plane sliding device

3.3.1 Numerical and Analytical Analyses

General drawing of 20 um and 50 um thick 1D sliding mode scanners is shown in Figure 3.5. As illustrated in Figure 3.6, finite element modeling (FEM) is performed via ANSYS© simulation software with dimensions of the hallow frame design (D2HF2) given in Table 3.1. Natural frequencies of the IP- and OP- resonance modes are obtained with modal analysis and found at 2622 Hz and 12.1 kHz, respectively. The mechanical coupling efficiency at the OP-resonance mode is derived from the ANSYS analysis is found to be 7.8.

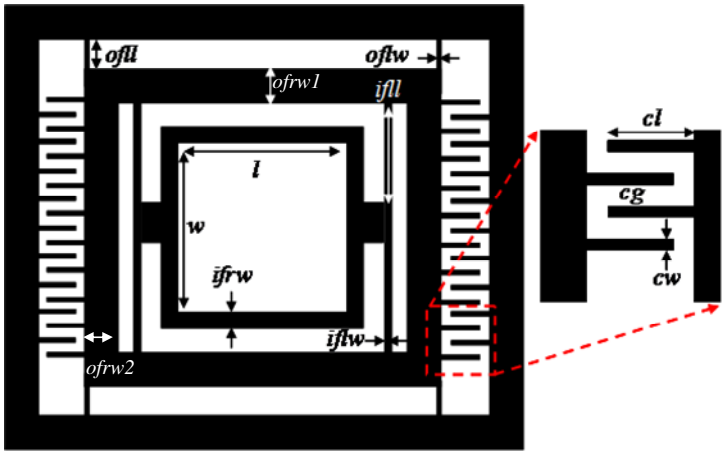

Figure 3.5: 2D illustration of the 1D in- plane scanner and geometrical parameters

Parameter		Dimension (um)
W	Inner frame width	1500
L	Inner frame length	1500
İfrw	Inner frame thickness	75
İfll	Inner flexure length	775
İflw	Inner flexure width	18
Ofrw1	Outer frame width1	650
Ofrw2	Outer frame width2	200
ofll	Outer flexure length	700
oflw	Outer flexure width	13
Cl	Comb finger length	35
Cw	Comb finger width	2
Cg	Comb finger gap	4

Table 3.1: Dimensions of D2HF2

Modal Analysis Results	
IP- Resonance Mode *2622Hz*	*OP- Resonance Mode* *12. 1 kHz*
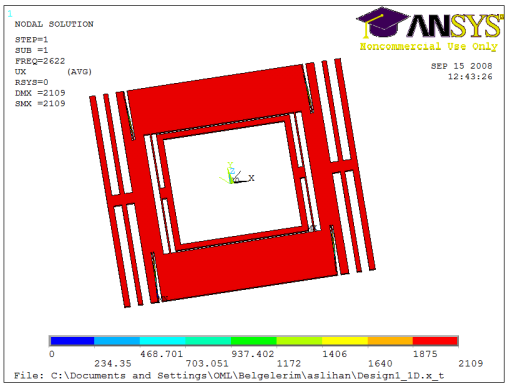	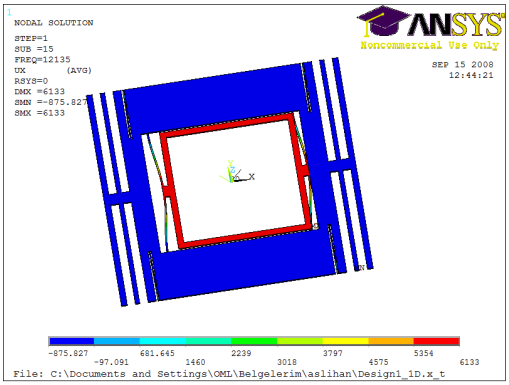

Figure 3.6: Modal analysis results of D2HF2 obtained using ANSYS

Frequency response of D2HF2 is obtained by harmonic analysis in MATLAB and illustrated in Figure 3.7. As seen in the figure, IP-mode resonance frequency is found at 2626 Hz and no mechanical coupling efficiency is observed at that mode as expected. At the OP- resonance mode, the mechanical coupling efficiency is found to be 8 at 11.57 kHz. OP-resonance frequency calculated using the analytically derived equation (3.17) and the corresponding mechanical coupling efficiency are obtained from (3.14) is exactly equal to the numerically obtained values.

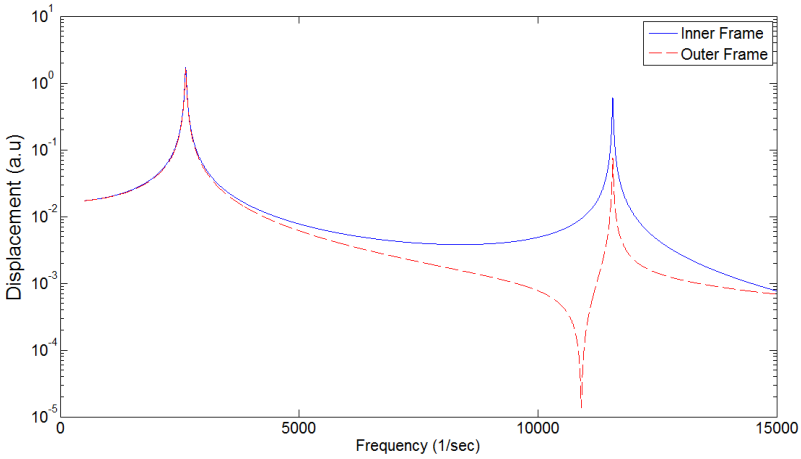

Figure 3.7: Harmonic analysis result of D2HF2

Transient analysis of the test device, presented in Figure 3.8, is performed by MATLAB© ODE solver at the IP- resonance frequency with 30 V peak-to-peak voltages and at the OP- resonance frequency with 15V peak- to- peak voltages.

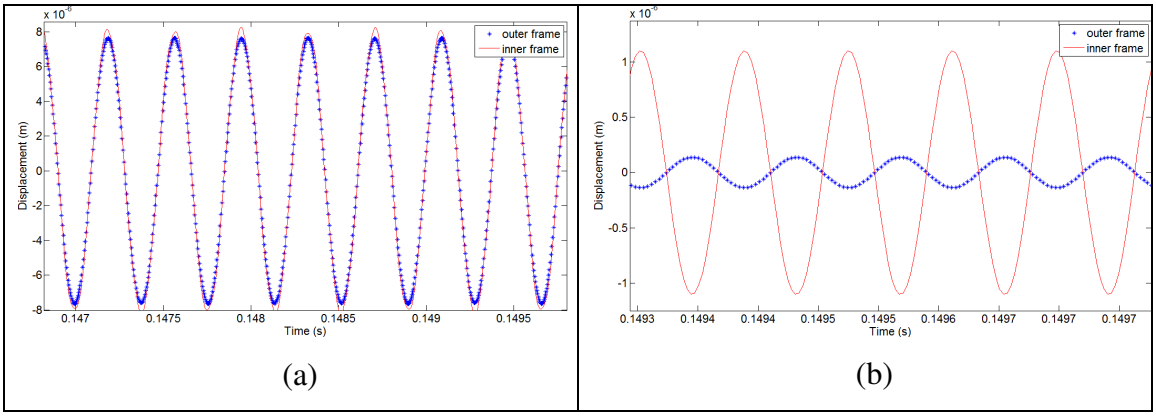

Figure 3.8: Transient analysis using MATLAB © ODE solver. (a) Deflection vs. Time at the IP- resonance mode. (b) Deflection vs. Time at the OP- resonance mode

As seen in Figure 3.8 (a), at the IP- resonance mode, inner and outer frames move in phase and displacement is 8 um. At the OP- resonance mode, frames move out- of- phase and the displacement of the inner frame is found to be 1.1 um (Figure 3.8(b)).

For optical utilization of the mechanical coupling, one should carefully optimize the system parameters for the desired characteristics. In the first analysis, to maximize the inner frame deflection, the effect of the outer frame mass and the outer flexure stiffness are analyzed. While the mass of the inner frame is not changed, the inner flexure stiffness is recalculated using (3.18) to achieve the predefined oscillation frequency (ω_c) with different values of the outer frame mass and the outer flexure stiffness for the unit force.

$$k_i = -\frac{\omega_o^{\,2} k_o m_i - (2\omega_c^{\,2} - \omega_o^{\,2})^2 (m_i m_t)}{-2k_o + 2m_i \omega_o^{\,2} + (4\omega_c^{\,2} - 2\omega_o^{\,2})(m_i + m_t)} \qquad (3.18)$$

The mechanical coupling efficiency and the deflection of the inner frame are calculated with respect to the ratio of the device mass to the inner frame mass ($R_m = m_t / m_i > 1$) and the outer flexure stiffness (k_o) for a unit force. The result is given as a contour plot in Figure 3.9. The optimization plots are marked by dashed lines and divided into two main parts with respect to the relation between the inner and outer frame resonance frequencies. In the left hand side of the marked area, the inner frame resonance frequency is higher than the outer frame resonance frequency ($\omega_o < \omega_i$), and in the right hand side; it is vice versa ($\omega_i < \omega_o$).

When $\omega_o < \omega_i$, mechanical coupling is obtained at the higher vibration frequency of the device. Therefore, at the OP-mode of the scanner, the deflection of the outer frame is transferred to the inner frame with mechanical amplification.

While the outer frame resonance frequency decreases, the inner flexure stiffness (k_i) increases to achieve the predetermined OP-resonance frequency (ω_{OP}). It should be noted

that, the mass of the outer frame can not be reduced drastically to preserve the necessary outer frame geometry around the inner frame and to have a significant mechanical coupling efficiency. As presented in 3.14, higher mechanical coupling efficiency is obtained with higher k_i. However, mechanical coupling efficiency is small in the boundaries where maximum deflection amplitude is achieved. Since the mechanical coupling efficiency is beneficial due to lateral pull-in and air damping, the parameters must be defined to optimize the system performance in order to achieve sufficient deflection and considerable mechanical coupling efficiency.

As discussed above, the sample scanner (D2HF2) has mechanical coupling at $\omega_{OP.}$ R_m and the outer flexure stiffness of the device are 8.5 and 60 N/m, respectively and marked on Figure 3.9. The scanner design has a significant mechanical coupling efficiency with sufficient inner frame deflection

In the narrow area between the dashed lines, mode separation disappears since the inner and outer frame resonance frequencies are very close to each other and coupling frequency shifts between OP-mode and IP-mode. Therefore, mechanical coupling can be obtained at the IP-mode when $\omega_i<\omega_o$ (right hand side of the marked region). In this case, higher mechanical coupling efficiency can be achieved increasing the outer frame resonance frequency of the device. However, the maximum achievable deflection is lower compared to the first case ($\omega_o<\omega_i$) due to stiffer outer flexures.

The mechanical coupling is determined mainly by the inner frame resonance frequency (ω_i). While the coupling frequency approaches to the inner frame resonance frequency (ω_i), mechanical coupling efficiency increases and makes maximum where the coupling frequency equals ω_i. However, it is proven that, the maximum deflection is not in company with the maximum mechanical coupling efficiency.

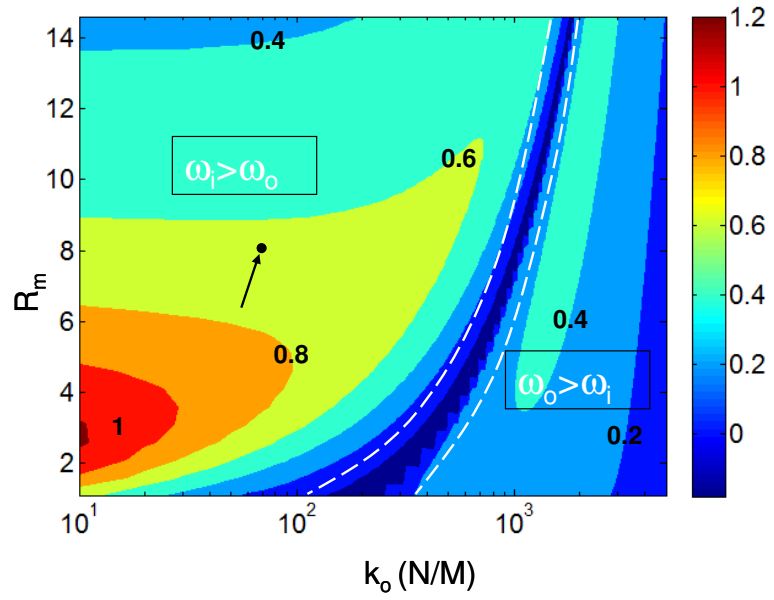

(a)

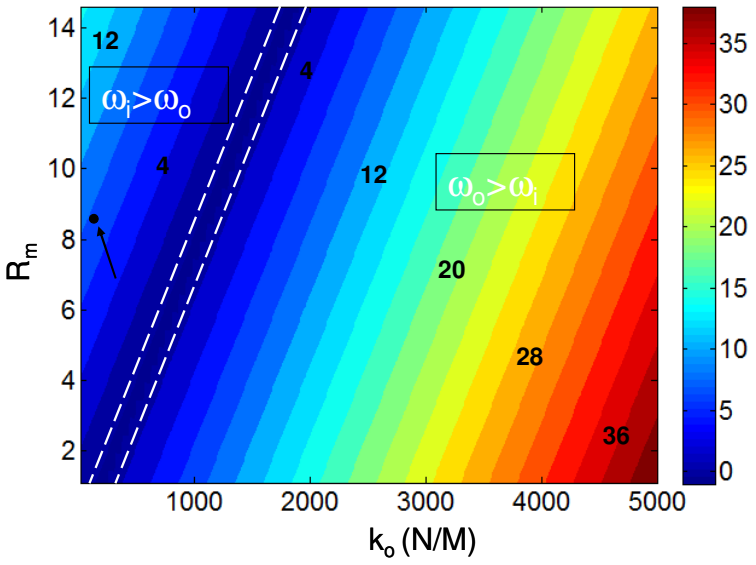

(b)

Figure 3.9: Effects of the outer frame mass and outer flexure stiffness on (a) Inner frame deflection. (b) Mechanical coupling efficiency.

In the first analysis, it is proven that, the coupling frequency can shift between IP-resonance mode and OP-resonance mode depending on the device parameters. In the second analysis this shift is demonstrated clearly. This time, both inner frame mass and the inner flexure stiffness are kept constant and coupling frequency and the corresponding mechanical coupling efficiency are calculated with respect to different outer frame mass and outer flexure stiffness values (Figure 3.10).

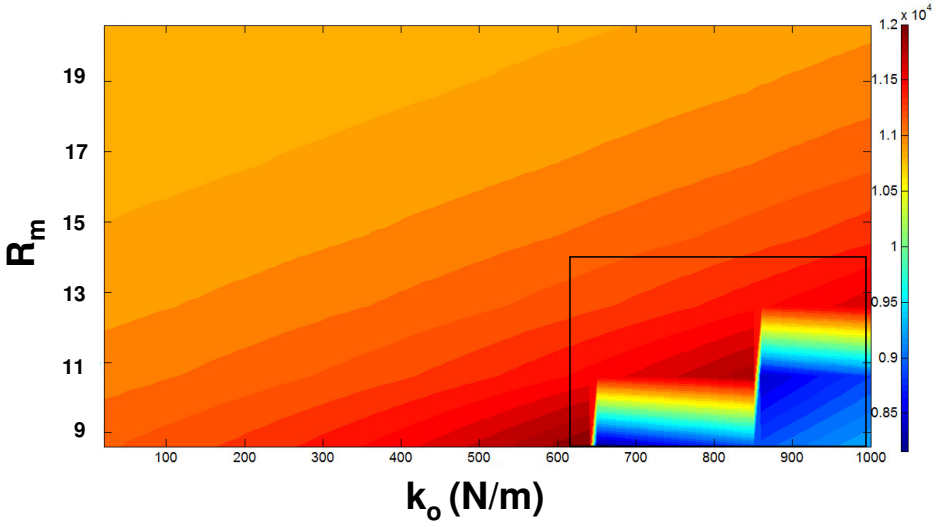

(a)

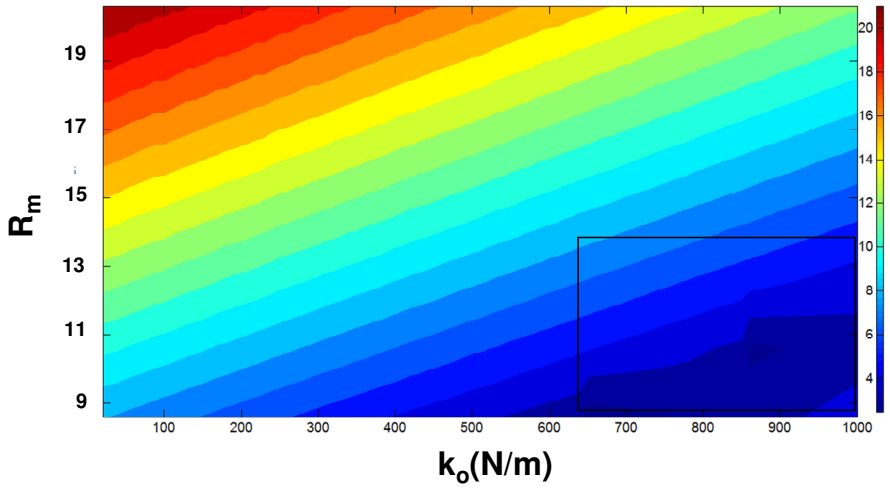

(b)

Figure 3.10: Effects of the outer frame mass and outer flexure stiffness on (a) coupling frequency (b) mechanical coupling efficiency.

At the lower values of k_o mechanical coupling is obtained at the OP-mode. As a result of the frequency variations, a mechanical coupling efficiency>1 can be obtained at the IP-

mode. In the region marked by a rectangular box used on Figure 3.10 illustrates the situation, in detail. When the outer flexure stiffness is lower than 650 N/m, mechanical coupling is obtained at the OP-resonance mode. In the marked area, higher mechanical coupling efficiency is obtained at the IP-resonance mode instead of OP-resonance mode (color shifts from red to blue in Figure 3.10(a)). For example, when k_o=900 N/m and R_m=8.6, the mechanical coupling efficiency obtained at the IP-mode is higher than the mechanical coupling efficiency obtained at the OP-mode Figure 3.11. By increasing the outer frame mass, higher mechanical coupling efficiency can be obtained at the OP-mode, again (color changes from blue to red).

These results are obtained for mechanically coupled devices by using the sample 1D in-plane sliding device. Figure 3.9 and Figure 3.10 can be drawn for the devices oscillate at any of the fundamental vibration modes. The only difference would be the considered outer frame mass and the outer flexure stiffness boundaries.

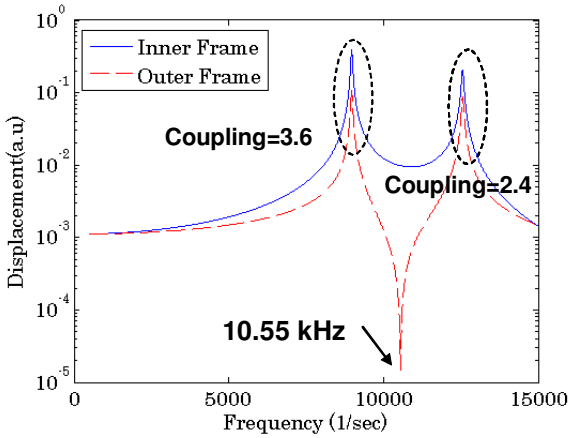

Figure 3.11: Frequency spectrum of the device with same inner frame dimensions R_m=8.6 and k_o=900 N/m.

As seen in Figure 3.2, 2-DOF system has two different quality factors at the IP- and the OP-resonance modes, defined by the structural and the viscous damping. The quality factor

dependency of the mechanical coupling efficiency is investigated numerically. The mechanical coupling efficiency is found to be independent of the quality factor at the IP-resonance mode while as illustrated in Figure 3.12 it is dependent on the lower values of the quality factor at the OP- resonance mode.

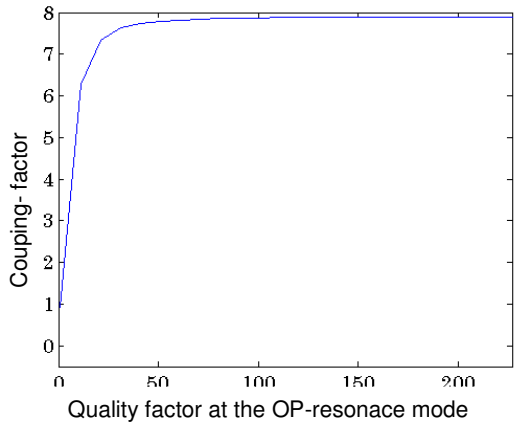

Figure 3.12: Mechanical coupling efficiency vs. quality factor at the OP- resonance mode

Quality factor of the OP- resonance mode is experimentally found to be 678 for D2HF2. For two- body system, it can be stated that mechanical coupling efficiency is independent of both quality factors of both the IP- and the OP- resonance mode.

3.3.2 Experimental Results of the 1D In- plane Sliding Design

Comb drive scanner designs are tested to validate the mechanical coupling mechanism. Complementary and biased drive voltages are applied to comb fingers on either side of the outer frame for differential driving to ensure harmonic excitation (Figure 3.13). The driving voltages and the electrostatic force exerted on the scanner are illustrated with the equations 3.18, 3.19 and 3.20. Capacitance change in the system is denoted by $\frac{\partial C}{\partial x}$ and expressed in Chapter 2

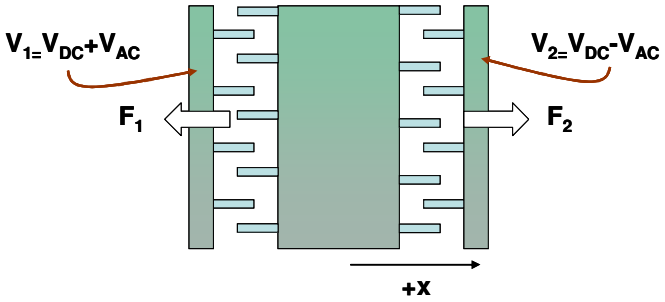

Figure 3.13: Driving of the comb actuated in- plane sliding devices with complementary biased signal.

$$V_1 = V_{DC} + V_{AC}$$
$$V_2 = V_{DC} - V_{AC} \qquad (3.\ 19)$$

$$F_1 = \frac{1}{2}\frac{\partial C}{\partial x}V_1^{\ 2}$$
$$F_2 = \frac{1}{2}\frac{\partial C}{\partial x}V_2^{\ 2} \qquad (3.\ 20)$$

$$F_{net} = F_1 - F_2 = \frac{1}{2}\frac{\partial C}{\partial x}(V_1^{\ 2} - V_2^{\ 2})$$
$$F_{net} = \frac{1}{2}\frac{\partial C}{\partial x}4V_{DC}V_{AC} \qquad (3.\ 21)$$

Microscope picture of the sample test device is shown in Figure 3.14. Experimental frequency response and voltage response of the scanner is illustrated in Figure 3.15. IP-resonance and OP- resonance frequencies are 2.63 kHz and 11.51 kHz, respectively. At the lower vibration mode, 6 um deflection is obtained with 30 V peak-to-peak voltage. Frequency response of the scanner is not hysteretic. The path traced when the frequency sweep up and down are same in the in- plane sliding mode. However, cubic nonlinearity in the forcing function results in spring stiffening at the IP- resonance mode with 30 Vpp

voltages. At the OP-resonance mode, the frequency response is linear with 15 Vpp excitation voltages and 1 um inner frame deflection is obtained. The mechanical coupling efficiency is found to be 5. The maximum voltage applied to the scanner is 100 Vpp voltages and 9 µm inner frame deflection is obtained at 11.51 KHz.

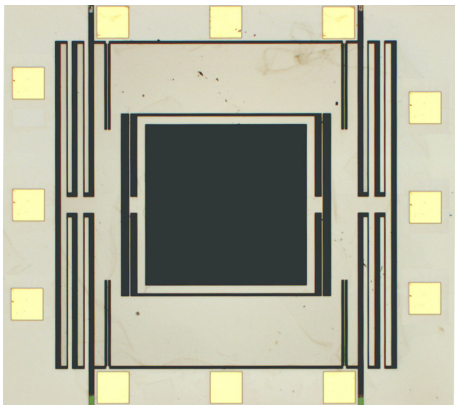

Figure 3.14: Microscope picture of the fabricated 1D comb actuated MEMS device (D2HF2).

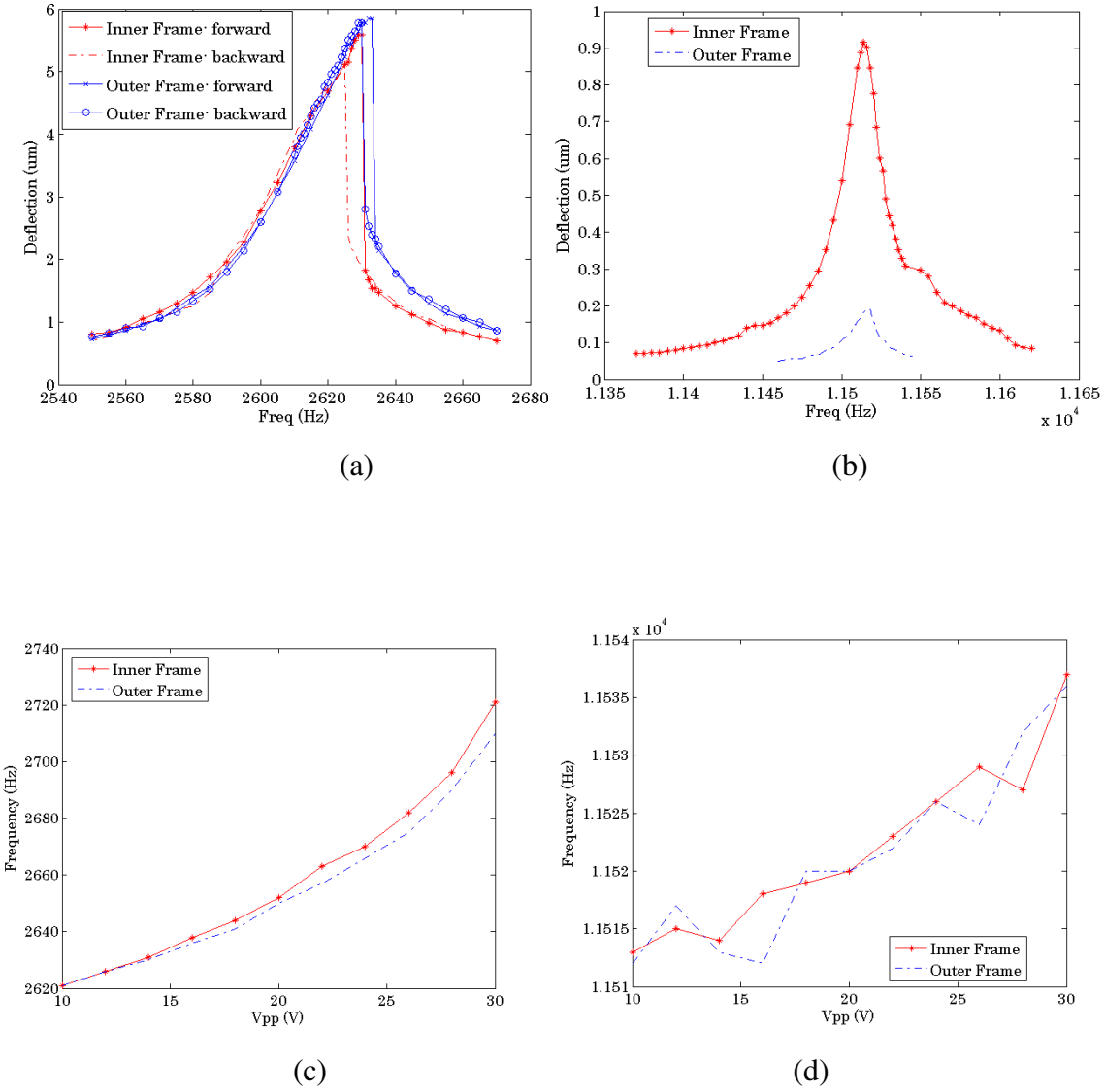

Figure 3.15: Experimental result of frequency response at (a) IP- resonance mode (b) OP- resonance mode. (c) Frequency shift with voltage variation at the IP- resonance frequency, (d) Frequency shift with voltage variation at the OP- resonance frequency.

Resonant frequency shift at the IP- and OP-resonance frequencies due to mechanical spring non-linearity is illustrated in Figure 3.15 (c) and Figure 3.15 (d).

Experimentally obtained deflections are only slightly different than the numerically obtained values, which is mainly due to the fabrication variations and some broken comb fingers.

3.4 2D Sliding Mode Devices

In addition to the 1D in- plane sliding devices, mechanical coupling principle is also implemented to 2D sliding devices. 2D sliding designs are fabricated in order to actuate in-plane sliding mode at IP- resonance frequency and actuate in out- of plane (OOP) mode at the OP-resonance frequency, simultaneously. For the in- plane sliding motion, combs on the either side of the outer frame will be driven with complementary DC biased sinusoidal signal and for the out- of- plane sliding motion, they will be driven with same DC biased sinusoidal signal. In order to actuate the microscanners in the out-of-plane sliding motion, a slight height difference should be in the comb fingers. Since the microscanners are not fabricated perfectly, comb fingers are not in the same lateral level and there is a height difference between conjugate fingers. This imperfection results in the out-of-plane motion.

3D Illustrations of the fabricated designs are shown in Figure 3.16 and the dimensions of the device parameters are shown in Table 3.2.These devices are fabricated on 50 um SOI wafers.

Design1	***Design 2***	***Design 3***
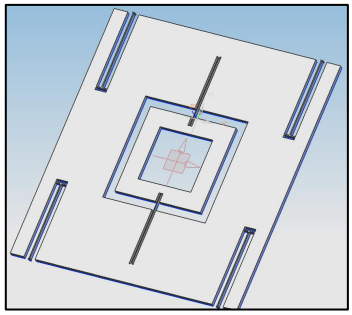	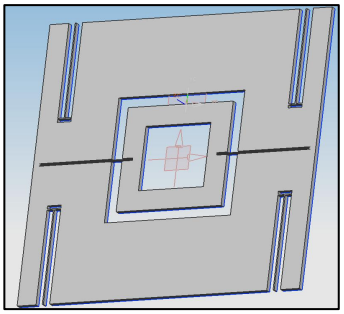	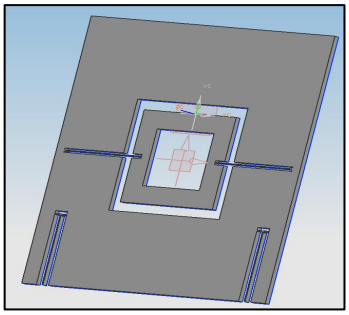

Figure 3.16: 3D illustrations of 2D linear devices

Dimensions	***Design 1***	***Design 2***	***Design 3***
Outer Frame Width	2650 um	2650 um	2650 um
Outer Frame Length	2700 um	2900 um	2900 um
Inner Frame Width	1 mm	1 mm	1 mm
Inner Frame Length	1mm	1 mm	1 mm
Inner flexure length	870 um	820 um	800 um
Inner flexure width	7 um	6,5 um	6 um
Outer flexure length	950 um	920 um	800 um
Outer flexure width	10 um	10 um	10 um

Table 3.2: Dimensions of 2D linear devices

The maximum edge length of the 2D devices is limited to 3 mm. Besides, these devices are designed to have out-of-plane and OP- resonance frequency around 10 kHz. Due to the frequency and the dimension restrictions, inner flexures of the 2D devices are designed long and narrow. However, at the end of the release process, inner flexures of the most of the devices are broken and inner frames did not survive. This problem is evidence for the fragility of the narrow and long micro structures. Device review is still continuing and new designs will be fabricated in the future. Despite the fabricated devices did not survive,

numerical analysis results of *Design 2* are included in the thesis. Frequency spectrum of the device is obtained by harmonic analysis in MATLAB and illustrated in Figure 3.18. IP- and OP-resonance frequencies belong to in-plane and out- of- plane sliding modes of the device are shown in Figure 3.17. As stated above, in 2D devices, we are concerned with the IP-resonance frequency of the in- plane sliding mode and the OP-resonance frequency of the out-of-plane mode. Mechanical coupling efficiency in the out-of-plane mode of the device is found to be 5.5 in MATLAB.

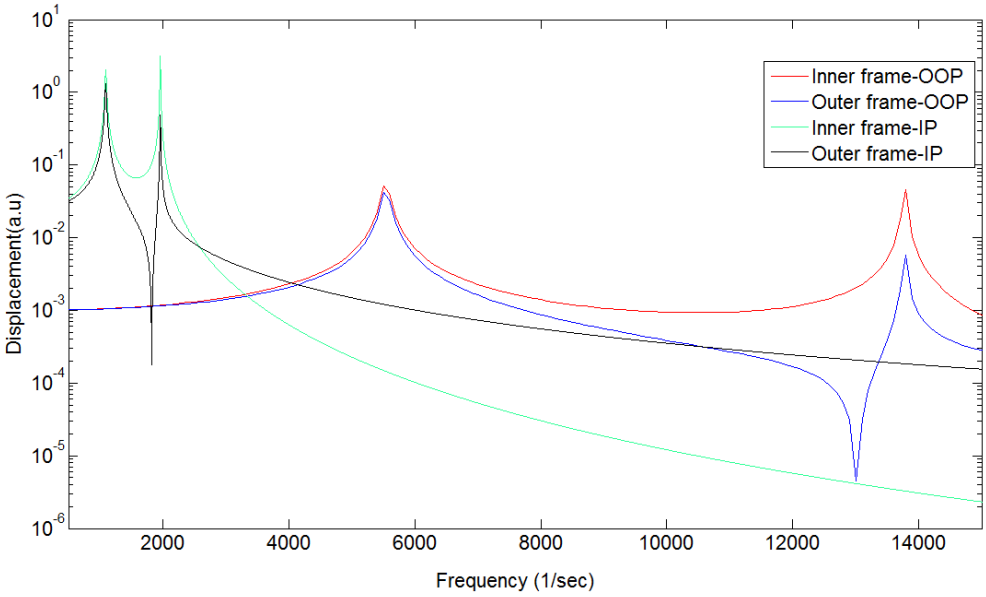

Figure 3.17: Harmonic analysis results of *Design 2*

Vibration mode	IP-Resonance Frequency	OP- Resonance Frequency
In-Plane sliding	1092 Hz	1957 Hz
Out-of-plane sliding	5.5 kHz	13.8 kHz

Table 3.3: Natural resonance frequencies of IP and OOP modes of *Design 2* obtained using MATLAB

Natural frequencies of the device are also obtained with modal analysis in ANSYS and illustrated in Figure 3.18. IP- resonance frequency of the in-plane sliding mode is found 1.3 kHz and OP-resonance frequency of the out-of-plane sliding mode is found 12 kHz.

In-Plane Sliding Mode/ IP-resonance frequency 1.3 kHz	Out-of-Plane Sliding Mode/ OP-resonance frequency 12.01 kHz
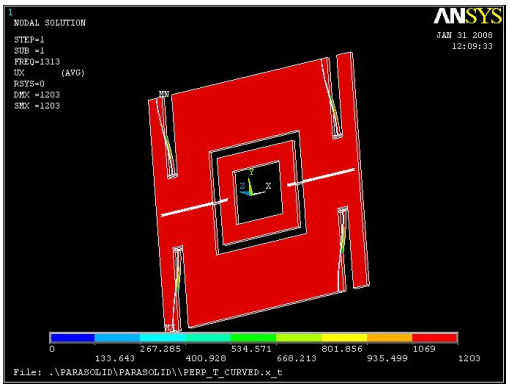	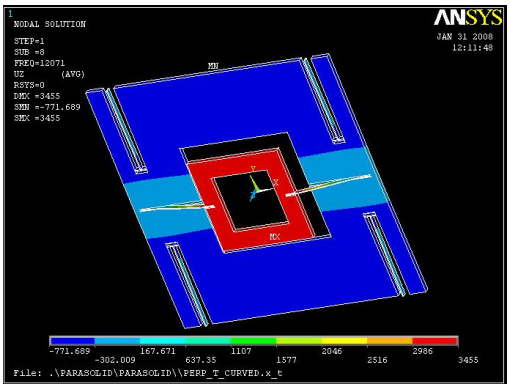

Figure 3.18: Modal analysis results of *Design 2* is obtained using ANSYS simulation tool

3.5 Torsion Devices

Silicon torsional MEMS scanners are used for scanning the light beams and first presented by Petersen [34]. In this study, mechanical coupling of the electrostatically actuated torsion scanners is investigated in addition to the linear scanners. Torsional devices are designed to achieve 24 kHz OP- resonance frequency and 18º inner frame MSA (Mechanical Scan Angle). Device layer thickness is 50 um. Inner frame stands for the mirror in torsional devices and 3D illustration of the design is shown in Figure 3.19. θ_o º and θ_i º are MSA (mechanical scan angle) of the outer and inner frame, respectively. Reflection of Si (silicon) surface is enhanced via depositing Al.

In order to actuate comb drive torsional microscanners, at the rest position, there should be a small height difference between fixed and movable fingers, since the actuation depend on the capacitance change. Comb fingers already have a vertical asymmetry due to microfabrication; scanners can operate in the fundamental resonant mode without requiring offset combs.

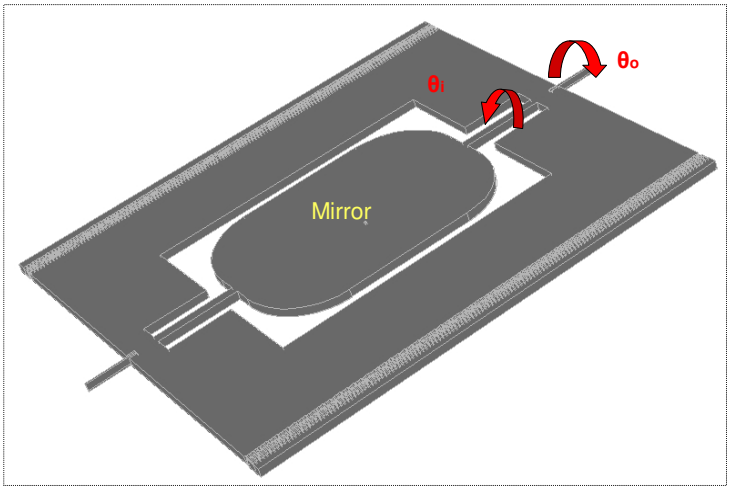

Figure 3.19: 3D illustration of the torsional scanner actuated with mechanical coupling. The comb fingers are along the two edges of the outer frame.

3.5.1 FEM and Numerical Analyses of Torsion Devices

Modal analysis of the torsion scanners is performed with ANSYS and natural frequencies of the IP- resonance and OP- resonance modes are investigated. Dimensions of the torsion test device are illustrated in Table 3.4. Parameters used in this design is same with the parameters used in the in- plane scanners.

Parameter		Dimension (um)
W	Inner frame width	1500
L	Inner frame length	1000
İfll	Inner flexure length	480
İflw	Inner flexure width	50
Ofrw1	Outer frame width1	550
Ofrw2	Outer frame width2	500
ofll	Outer flexure length	300
oflw	Outer flexure width	12
Cl	Comb finger length	50
Cw	Comb finger width	5
Cg	Comb finger gap	5

Table 3.4: Dimensions of the fabricated torsional scanner

ANSYS modal analysis results are shown in Figure 3.20. IP- resonance frequency is found at 1035 Hz and the OP- resonance frequency is found at 23.9 kHz. Mechanical coupling efficiency at the OP- resonance mode is found to be 9 for tip displacement at z-direction. Using device dimensions, mechanical coupling efficiency of the deflection angle is found to be 21.

Modal Analysis Results	
IP- Resonance Mode 1035 Hz	OP- Resonance Mode 23.9 kHz
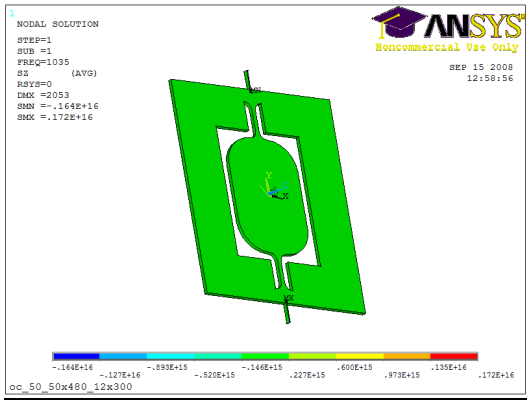	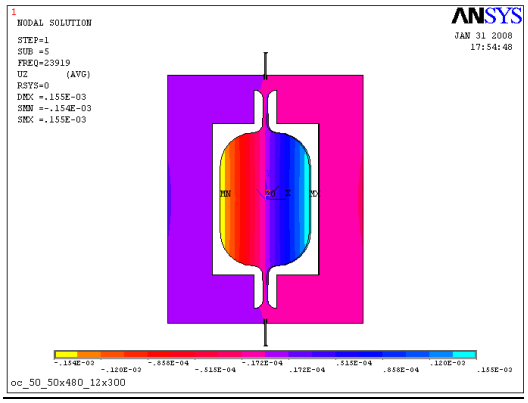

Figure 3.20: ANSYS: FEA of the 1D torsional MEMS scanner

Stress analysis of the torsion scanner is performed in ANSYS as well and designs are modified in order to decrease the 1 st principle stress below 1GPa. Maximum 1st principle stress of the torsion scanner is found 1.74 GPa for 18º mirror MSA (Figure 3.21). So that, the maximum achievable MSA of the inner frame is 10 º with 1 GPa stress for this scanner design at the OP-resonance mode.

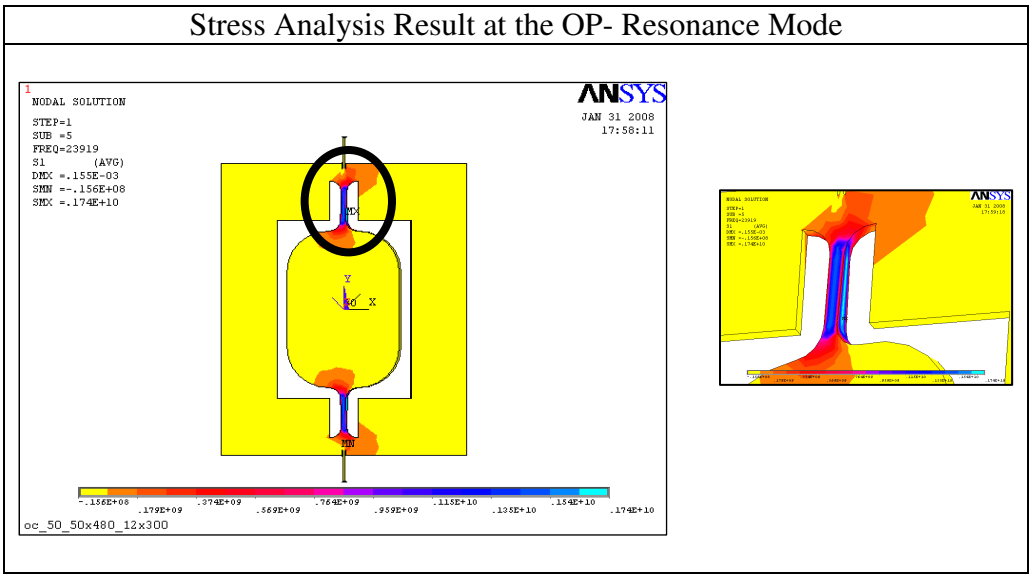

Figure 3.21: Stress analysis results in ANSYS

Frequency response of the torsional scanner is obtained using MATLAB© and illustrated in Figure 3.22. IP- and OP- resonance frequencies are found at 1060 Hz and 22.3 kHz, respectively. Numerically, mechanical coupling efficiency is found to be 22 (in rotation). Frequency response curve of the torsion scanner has the same form with the out-of-plane scanners and were discussed in detail in [40].

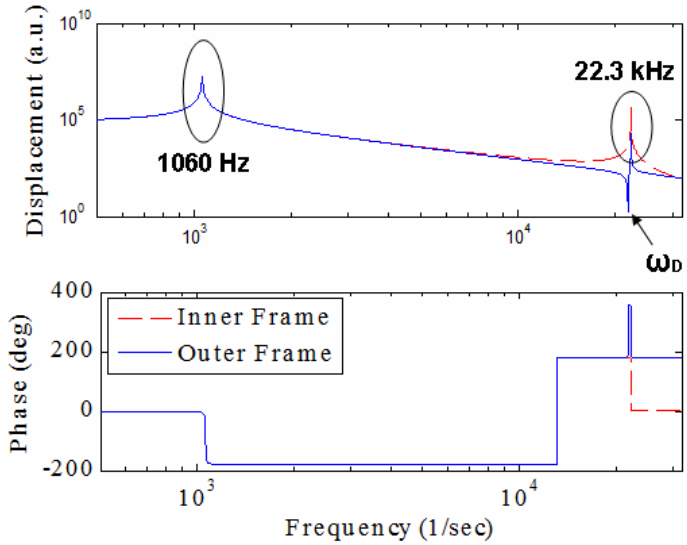

Figure 3.22: Frequency response of the fabricated torsional scanner obtained using MATLAB

Torsional scanners have equation of the motion in the form of parametric nonlinear ODE which is discussed in detail in chapter 4. Parametric system has a hysterical frequency response and two different jump frequencies are obtained while frequency is swept up and swept down, depending on the initial conditions. As a result of the parametric characteristics of the torsional scanners, in the transient analysis, electrostatic force is calculated around twice the mechanical resonance frequency.

Transient analysis of the torsion scanner is performed using MATLAB© ODE solvers. In order to find the MSA of the mirror numerically, electrostatic force generated at the comb fingers is calculated with 14 Vpp DC biased voltages. Corresponding MSA of the device is plotted in Figure 3.23. At the IP- resonance mode of the scanner, first and second jump frequencies of the excitation signal are found at 2130 Hz and 2155 Hz, respectively. Numerically, 1.5° and 0.4° MSA is obtained at the first and the second jump frequencies, respectively. Likewise, at the OP- resonance mode, there are two jump frequencies at

46654 Hz and 46642 Hz. Transient analysis results confirm the out- of- phase motion of the scanners at the OP- resonance mode. Numerically, 300 V peak- to- peak DC biased sinusoidal excitation signal result in 20 ° and 15º mirror MSA at the first and the second jump frequencies.

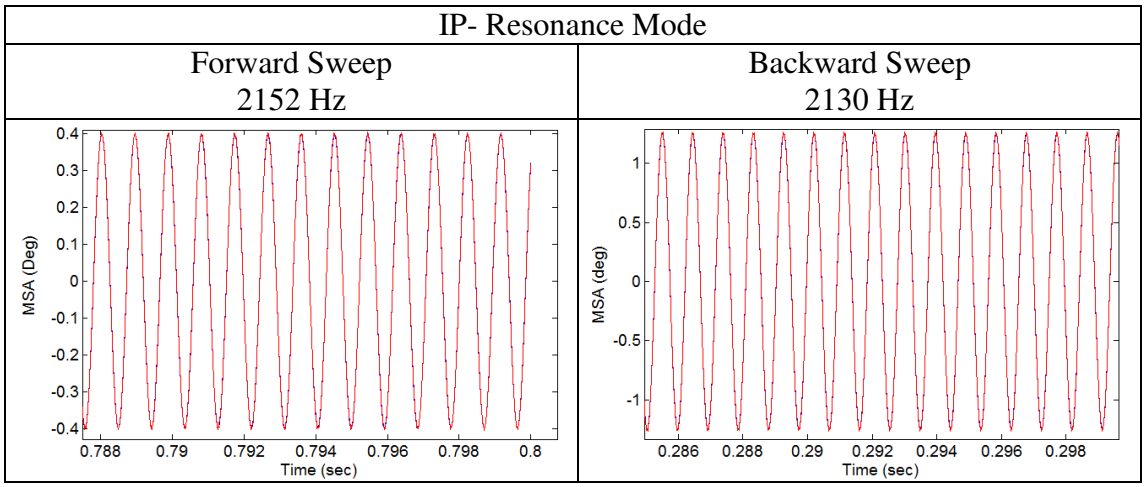

(a)

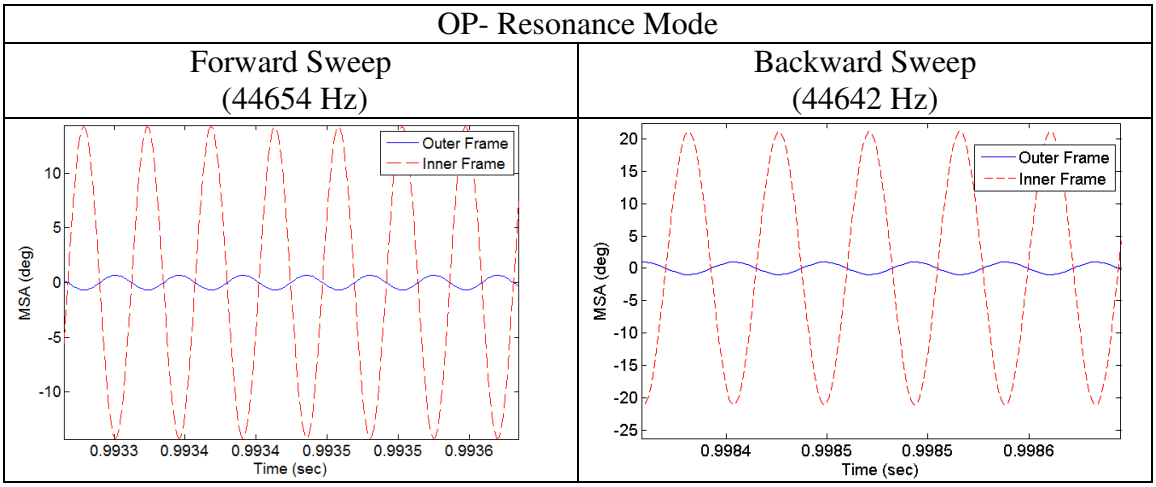

(b)

Figure 3.23: Transient analysis results at 2f excitation frequency (a) IP- resonance mode (b) OP-resonance mode

3.5.2 Experimental Results

Torsional devices are driven by DC biased sinusoidal signals and total optical scan angle (TOSA) of the mirror is measured at IP- and OP- resonance modes of the device illustrated at Figure 3.24. Device is driven with 14 Vpp voltages and 2º TOSA is obtained at IP- resonance mode. Regarding the numerical results derived solving the equations of motion using MATLAB© ODE solver, expected TOSA is close to 6º. However, since the devices are not fabricated ideal, small differences were already expected. Most important difference between the designs and the fabricated devices is broken comb fingers which directly decrease the generated electrostatic force. Moreover, comb fingers are thinned below the design dimensions because of over etch problem encountered during the fabrication.

During the tests, a good scan line is obtained at the IP- resonance mode, however, at the OP-resonance mode, only milidegree TOSA is obtained at both mirror and outer frame with voltages up to 200 Vpp. In order to figure out the reason of this result, voltage stability analysis of the device is performed and the minimum required voltage of the design is found close to 260 V peak- to- peak voltage. Since the isolation layer is not thick enough, we could not drive the scanner with voltages over 200 Vpp, so that we could not achieve the numerically expected TOSA. Voltage stability analysis of the device is discussed in the subsequent chapter.

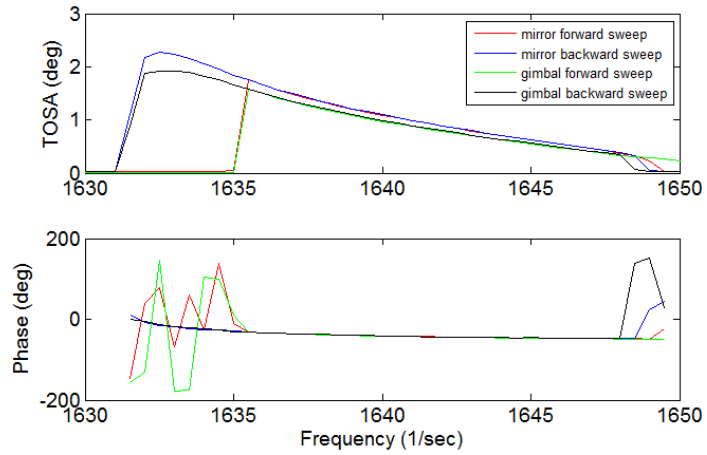

(a)

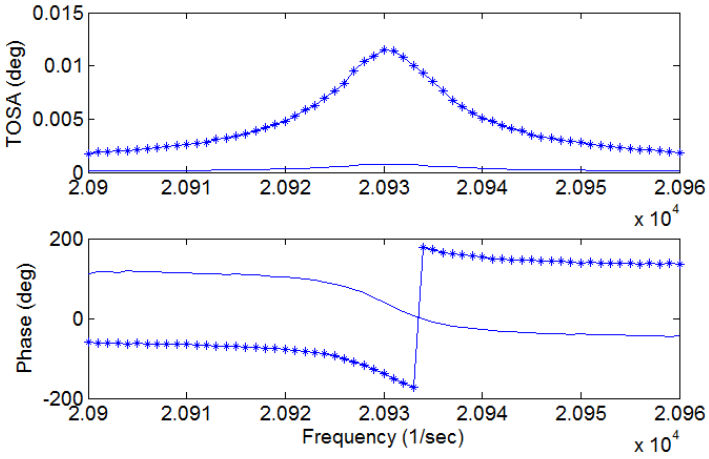

(b)

Figure 3.24: Experimentally obtained deflections at (a) IP- resonance mode, (b) OP-resonance mode. The mirror and the gimbal in the figure represent the inner and the outer frame.

Chapter 4

VOLTAGE STABILITY AND DAMPING ANALYSIS FOR TORSIONAL SCANNERS

4.1 Frequency Domain Characteristics of Torsion Scanners

Comb- actuated scanners are used in the applications require either in- plane or out- of plane motion. As shown in Figure 2.7 (a), at the in-plane sliding mode, rate of the capacitance change with respect to the displacement is independent of the displacement of the fingers. The in- plane actuation is governed by a second order differential equation with constant coefficients. Actuation mechanism of the torsional devices is different. Capacitance change rate in this mode depends on the angular deflection and illustrated in Figure 2.7 (b). Thus, the electrostatic torque depends on the displacement as well as the voltage and the system is no longer linear due to the time varying coefficients. The system is called parametric system. In definition, a system is parametric if one of the coefficients of the governing equation changes with time periodically [46]. The playground swing is a simple example of the parametric oscillations [46, 47]. Parametric systems show hysterical behavior and generate subharmonic oscillations [40].

The equation of motion for the electrostatically actuated torsional scanner is shown in (4.1).

$$I\frac{d^2\theta}{dt^2} + b\frac{d\theta}{dt} + k\theta = M(\theta) \qquad (4.1)$$

where;

I= Mass moment of inertia,

b=Damping constant,

k=Torsional spring stiffness,

M(θ)=Electrostatic torque.

For N number of comb fingers, the torque function is expressed as:

$$M(\theta) = 2N\frac{dC}{d\theta}V(t)^2 \tag{4. 2}$$

Where V(t) is the time dependent voltage applied to the microscanner and the resulting torque is a function of both time and the displacement. Derivation of the general solution of the equation of motion is difficult, some assumptions are made and the resulting torque function is obtained in (4.3) for the square root of a biased sinusoidal function V(t) .

$$M(\theta) = -(r_3\theta^3 + r_1\theta)A^2(\cos(wt)+1) \tag{4. 3}$$

Rate of change of the total capacitance is expressed as third order polynomial and since the torque function is odd, even order terms are removed from the function. (4.2) is rewritten by substituting the torque function and the oscillation frequency:

$$\frac{d^2\theta}{dt^2} + \alpha\frac{d\theta}{dt} + (\beta + 2\delta\cos(2\tau))\theta + (\delta_1 + \delta_3\cos(2\tau))\theta^3 = 0 \tag{4. 4}$$

where;

$$\tau = \frac{wt}{2}, \qquad \alpha = \frac{b}{wI}, \qquad \beta = 4\frac{(r_1A^2 + k)}{w^2I}, \quad \delta_1 = \frac{2r_1A^2}{w_2I}, \qquad \delta_3 = \frac{4r_3A^2}{w^2I} \tag{4. 5}$$

Time dependence of the coefficients is clearly seen in (4.4). The analytical solution of (4.4) is derived in [40, 48] by neglecting cubic nonlinearity and in this thesis, only the results of the analysis are considered.

Figure 4.1 illustrates the excitation signal and mirror scan waveform. The solid line represents the deflection and the dashed line represents the square wave driving signal. In order to start the oscillations, electrostatic torque is applied to initially tilted comb fingers to pull the scanner to its rest position. When scanner passes through the rest position, driving voltage is switched off and the scanner makes maximum deflection by its momentum. Thus, frequency of the driving signal is twice the mechanical oscillation frequency. Using a square wave signal with duty factor of 50% is the most effective way to excite the scanner [49]. Excitation frequency is important to have the maximum deflection. If the switch- off time of the excitation signal coincides with the position where the scanner passes the rest position, the scanner is not subjected to decelerating electrostatic torque at the point of maximum deflection. If this condition fails, then the oscillation amplitude decreases. Therefore, at the primary resonance, mechanical oscillation frequency (f_m) is half of the frequency of the excitation signal and these oscillations are called subharmonic oscillations [40, 50]. In order to produce a large response with small excitation, excitation frequency must be at the primary resonance frequency or an integer fraction of $2f_m$. nth-order resonance is located at $2f_m/n$, n=1,2,3…. Maximum amplitude is obtained at n=1 and it decreases with higher values of n.

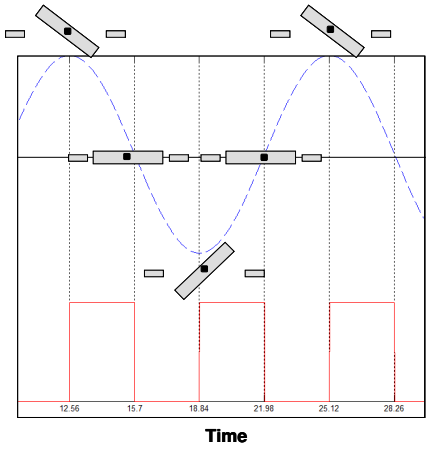

Figure 4.1: Oscillation and excitation waveform. Solid line represents the square- wave excitation signal and dashed line represents the deflection waveform of the torsional scanner

Parametric systems have hysterical frequency behavior and variation of the deflection angle with respect to frequency is illustrated in Figure 4.2 [40, 49]. The path traced when the frequency is increased is different than the path traced when the frequency is decreased. When the excitation frequency is swept down, deflection angle increases and at the frequency denoted by f_1, deflection angle has its maximum value. When the frequency is swept up, until f_2, deflection angle is zero. f_1 and f_2 are called the jump frequencies. There is only one stable solution where $f>f_2$ and $f<f_1$. However, there are two stable solutions between the jump frequencies depending on the initial condition. In order to find maximum scan angle, initial condition of the system must be higher than the maximum scan angle.

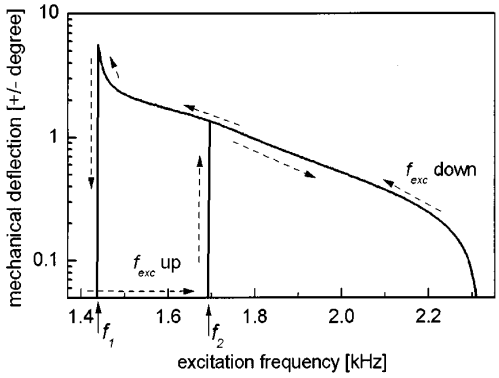

Figure 4.2: Hysterical frequency response of torsional microscanners [49]

4.2 Stability Analysis: Numerical and Experimental Results

The region between two jump frequencies f_1 and f_2 is unstable. These boundary frequencies depend on the amplitude of the excitation voltage. For different applied voltages, the range between the jump frequencies changes and a tongue- like shape stability curve is obtained. The analytical investigation of the stability characteristics of the system is performed in [40, 48]. An example of a typical stability tongue is illustrated in Figure 4.3. This result is not related to the actual devices used in thesis and just used to show the stability behavior of the comb actuated torsional microscanners. As shown in the figure, oscillation in the torsional mode does not start until a certain voltage. At the minimum required voltage, two jump frequencies approach to each other and the unstable region in the frequency response curve disappears.

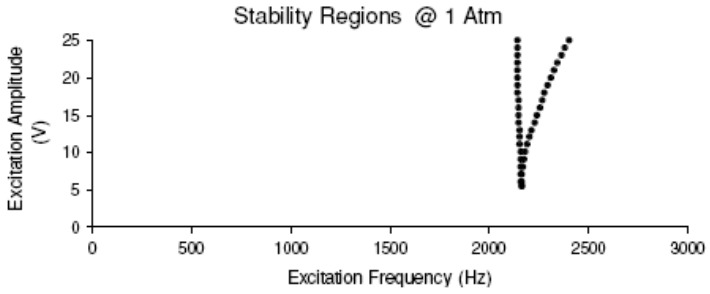

Figure 4.3: Typical voltage stability: Excitation voltage amplitude vs. frequency [50].

In this thesis, stability of the torsional scanners is analyzed numerically and for different excitation voltages, jump frequencies are found. 3D illustration, geometrical dimensions, numerical analysis and the finite element modeling of the torsional scanners are already illustrated in the previous chapter.

Experimentally obtained frequency response of the test device is shown in Figure 4.4. At the IP-resonance mode, the hysterical frequency response of the scanner is seen clearly. At the OP- resonance mode, the frequency response curve shows a linear behavior. However, note that, the deflection angle at this mode is very small to be considered as a real deflection. This experimental result is obtained with 14 Vpp and 40 Vpp voltages, respectively. Up to 200 Vpp voltage is applied to the scanner at OP-resonance mode, however, still a considerable deflection was not achieved.

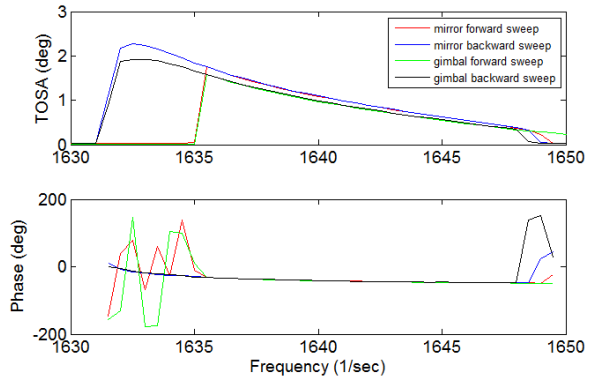

(a)

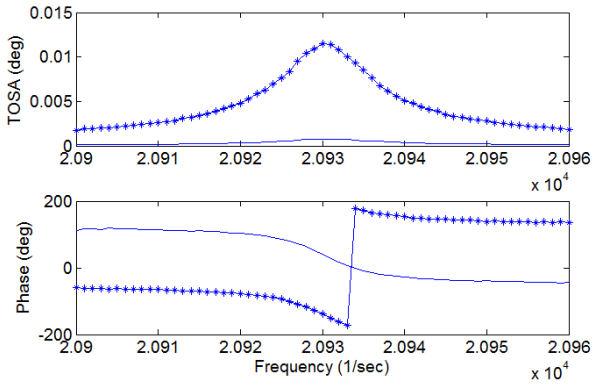

(b)

Figure 4.4: (a) Frequency response of the test device at the IP- resonance mode. (b) Frequency response of the test device at the OP- resonance mode

The voltage stability analysis of the fabricated torsional scanner is performed using MATLAB© ODE solver. In order to find the jump frequencies, equations of motions of the system are solved with different drive voltages. For each voltage, two different initial conditions are given to the system. To find the higher jump frequency (f_2), a quite small initial condition is applied. Then, the lower jump frequency (f_1) is found by applying relatively higher initial condition. Results of the stability analysis are shown in Table 4.1 and Table 4.2.

Vpp	f_2	IF_MSA (deg)	f_1	IF_MSA (deg)
14	2155	0,40	2130	1,5

Table 4.1: Deflection amplitudes at IP- resonance mode obtained using MATLAB© ODE solver.

Vp-p	f_2	IF_MSA (deg)	OF_ MSA (deg)	f_1	IF_MSA(deg)	OF_MSA (deg)
600	44670	22,80	1,62	44644	40,00	2,50
550	44666	21,70	1,60	44643	38,90	2,46
500	44663	21,00	1,46	44642	37,00	2,17
450	44658	21,00	1,43	44642	35,50	2,00
400	44655	20,00	1,31	44642	34,00	1,66
300	44654	14,28	0,66	44642	21,10	0,97
280	44646	13,00	0,61	44641	20,80	0,93
260	44642	11,50	0,54	44641	19,20	0,88

Table 4.2: Deflection amplitudes at OP- resonance mode obtained using MATLAB© ODE solver.

Since the torsional test device is driven with 14 Vpp at the IP-resonance mode, numerical analysis is only performed for this voltage to compare experimental deflection with numerically obtained results. Maximum mechanical scan angle (MSA) is obtained at the first jump frequency (f_1) as considered and found to be 1.5º. In this case, total optical scan angle (TOSA) is 6º. Experimentally obtained TOSA is 2º which is lower than the MATLAB result. Main reasons for this difference are the broken comb fingers and the over etch problem in the comb gaps.

In order to start the actuation of the scanner, electrostatic force generated at the comb fingers must be higher than the total damping force which includes both structural and air damping. To generate required electrostatic force, our design needs 260 Vpp driving

voltage at the OP- resonance mode. Until this voltage, damping force is higher than the electrostatic force so that the oscillation does not start. During the calibration tests, fabricated scanners were driven with a maximum of 200 Vpp at the OP-resonance mode. At the voltages higher than 200 Vpp, the devices are burned. Therefore, at the OP-resonance mode, scan line is not obtained with the fabricated devices.

The stability curve of the test device is illustrated in Figure 4.5. 19.2º TOSA is obtained numerically with 260 Vpp voltages. At this voltage, instability region disappears.

It should be noted that, the numerical analysis are performed at the twice the excitation frequencies that is the IP- and OP- resonance frequencies.

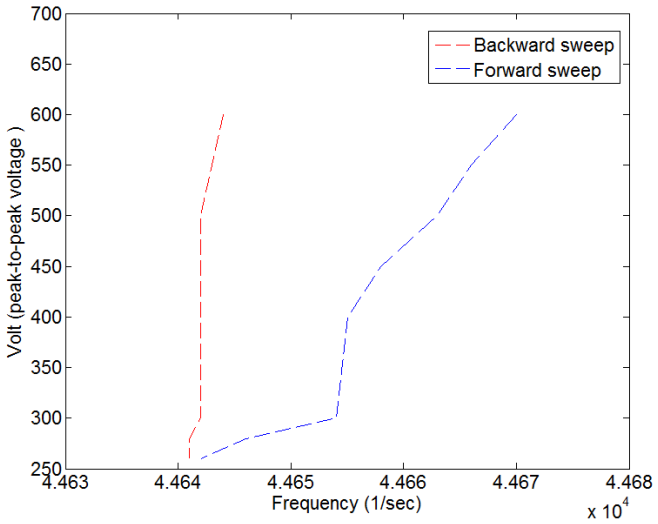

Figure 4.5: Voltage stability tongue for sample 1D torsional comb drive scanner at the OP-resonance mode

4.3 Damping Analysis of Torsional Microscanners

The minimum voltage required to start the oscillations is found by voltage stability analysis. Below this voltage, since the electrostatic force is lower than the damping force, oscillation can not be observed. The minimum voltage can be found by damping analysis, as well. In this method, air damping is calculated analytically by the help of MATLAB simulation tool. During the oscillations at the torsional mode, since the device oscillates out-of- plane, sliding film damping exists at the comb fingers and the frames experience drag force. In the literature [51], mostly, damping of the torsional devices is modeled with squeeze film damping. However, since during the tests, the gap width underneath the device is in the order of centimeter, squeeze film damping is not considered in these calculations.

4.3.1 Sliding Film Damping and Drag Force

Sliding film damping occurs between two parallel incompressible plates in x-y plane and illustrated in Figure 4.6. Slide film damping can be expressed by both the Couette flow and the Stokes flow models. Since the Couette flow ignores the inertial effects, it can be inaccurate for high frequencies. At high frequencies, the frequency dependent Stokes flow model is used [52].

Stokes flow model describes the air flow between two parallel planes as illustrated in Figure 4.6(a). Velocity gradient across the gap is not constant. To derive the Stokes flow model, Navier-Stokes equations simplify to nonlinear differential equations and given by:

$$\frac{\partial u(t,z)}{\partial t} = v\frac{\partial^2 u(t,z)}{\partial z^2} \tag{4. 6}$$

where;

$u(t,z)$ = Complex spatial velocity distribution

v = The kinetic viscosity

$$v = \frac{\eta}{\rho} \tag{4. 7}$$

η=Dynamic viscosity, ρ= Density of the fluid

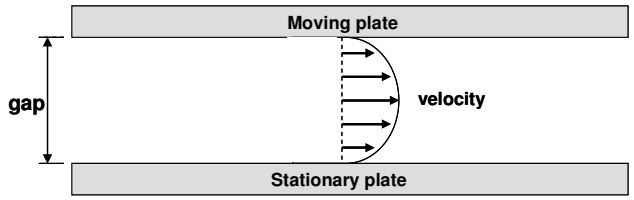

(a)

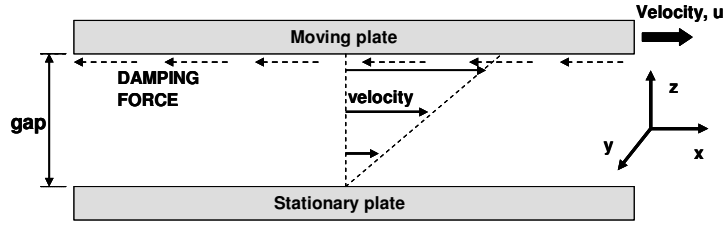

(b)

Figure 4.6: Sliding film damping between two infinite plates. (a) Stoke's flow model. (b) Laminar Couette flow model

Complex spatial velocity distribution is given by [35]:

$$u(t,z) = \hat{u}_x(z)e^{jwt}\Big|_{z=g} \tag{4. 8}$$

where

$\hat{u}_x(z)$ = Complex velocity amplitude of the moving plate surface.

w = Angular frequency

Air flow between the parallel plates is in the slip flow regime. The boundary conditions of the complex velocity amplitude $\underline{\hat{u}}(z)$ is defined by:

$$\hat{u}(z=0) = \lambda \frac{\partial \hat{u}}{\partial z}\Big|_{z=0} \qquad \hat{u}(z=g) = \hat{u}_x - \lambda \frac{\partial \hat{u}(z)}{\partial z}\Big|_{z=g} \tag{4. 9}$$

where λ is mean-free path of the gas molecules

To solve (4.6), slip- boundary conditions (4.9) and (4.8) are used and the following solution is obtained [35]:

$$\hat{u}(z) = \hat{u}_x \left[\frac{\sinh(D.z) + D\lambda\cosh(D.z)}{(1 + D^2\lambda^2)\sinh(D.g) + (2D\lambda\cosh(D.z)} \right] \tag{4. 10}$$

D is a complex frequency dependent variable, given by:

$$D = (1 + j)\sqrt{\frac{w}{2v}} \tag{4. 11}$$

A laminar Couette- flow model can be used low frequencies where the width and length of the parallel plates are much larger then the electrode trench width. Pressure gradient of the Navier- Stokes momentum equation is ignored and linear velocity model is used to illustrate the velocity profile of the Couette- flow model is [52, 35]:

$$\frac{\partial^2 \bar{u}(t, z)}{\partial t^2} = 0 \tag{4. 12}$$

$$u(z = 0) = 0 \qquad u(z = g) = u(x) \tag{4. 13}$$

With respect to no-slip condition, the velocity of the viscous fluid is zero relative to the solid moving boundary. Using the boundary conditions illustrated in (4.13) solution of the Navier- Stokes equations is found as follows:

$$u(z) = \frac{u(x)}{g} z \tag{4. 14}$$

It is found that the difference between the Stokes flow model and the Couette flow model is significantly low for frequencies lower than 100 kHz [35]. Since, our devices are designed to work frequencies lower than 25 kHz, Couette flow model is used in our analysis.

To find the sliding film damping between the comb fingers, viscous shear stress on the finger surfaces is defined as [35]:

$$\tau_{xz} = -\eta \frac{\partial u(z)}{\partial z} \tag{4. 15}$$

By substituting (4.14) in the viscous shear stress formula, sliding film damping torque (M_{cf}) is found as:

$$M_{cf}(\theta) = -\rho v \frac{u(x)}{g} A.R_{cf} \tag{4. 16}$$

where A is the area of the comb finger and R_{cf} is the distance of the comb finger to the torsion axis.

The angular deflection of the torsional scanner is defined as:

$\theta(t) = \hat{\theta}\sin(wt)$, where $\hat{\theta}$ is the amplitude of the angular deflection.

Speed of each comb finger is:

$$u = R_{cf}\dot{\theta}, \qquad \dot{\theta} = \hat{\theta} w \cos(wt) \tag{4. 17}$$

Using the sliding film torque and the speed of the comb fingers, damping torque experienced by the comb fingers is [35, 52]:

$$M_{cf}(\theta, t, R_{cf}) = -2R_{cf} \frac{\rho v L w u(\theta, t, R_{cf})}{g} \tag{4. 18}$$

where:

L=Length of the comb finger,

w= Width of the comb finger,

g= Width of the gap between comb fingers.

Damping experienced by the scanner is different than the damping at the comb fingers. Damping come out due to scanner deflection is calculated by the drag damping torque formula which is given by:

$$dM_{drag}(\theta,t,r,\Theta) = C_d \rho \frac{u(\theta,t,r,\Theta)^2}{2} R(r,\Theta) \tag{4. 19}$$

$$M_{drag}(\theta,t) = -2 \int_{0}^{0.5a+0.5L} \int_{-0.5\pi}^{0.5\pi} dM_{drag}(\theta,t,r,\Theta) r dr d\Theta \tag{4. 20}$$

where C_d is the shape dependent drag coefficient, a is the diameter of the circular scanner, r and Θ are the polar coordinates of the circular scanner.

Coordinates and limits of the integration are taken with respect to the circular shape scanners. However, the formulas are applicable to scanners with different geometrical shapes.

Length of the torsion arm R(r, Θ) and the velocity of the scanner $u(\theta,t,r,\Theta)$ are given by:

$$R(r,\Theta) = r\cos(\Theta), \qquad u(\theta,t,r,\Theta) = R(r,\Theta)\dot{\theta} \tag{4. 21}$$

The total damping torque for the torsional scanner with N comb fingers is:

$$M(\theta) = N.M_{cf}(\theta) + M_{drag}(\theta) \tag{4. 22}$$

4.3.2 Damping Analysis of the Torsional Devices and Comparison with Voltage Stability Results

Voltage stability result of the torsional scanner at the OP-resonance mode is illustrated in Table 4.2 and the stability curve is shown in Figure 4.5. In order to confirm the stability results, damping of the system is calculated by experimentally obtained quality factors. As stated in the previous chapter, experimentally obtained quality factors of the scanner at the IP- and OP- resonance modes are 237 and 2325, respectively. Quality factor of a system can be found with different methods. Resonant systems respond to their natural frequencies (f) stronger than other frequencies. So that, quality factor can be found using the bandwidth of the resonance. Quality factor of the OP- resonance mode is found by using the

experimental data. However, since the frequency response at the IP- resonance mode is nonlinear, quality factor is found by stopping the oscillation during the experiment. When the excitation signal is removed, system decelerates and signal dies out due to damping on the system as illustrated in Figure 4.7.

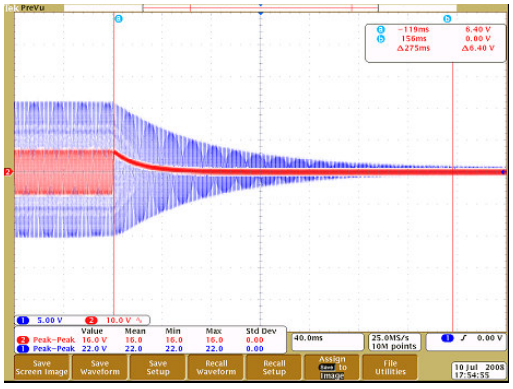

Figure 4.7: Damping response of the scanner at OP- resonance mode

Damping coefficient, b, can be find by fitting $e^{-\alpha wt}$ to the damped signal, where w is the natural frequency and α is damping ratio which is given as:

$$\alpha = \frac{b}{2\sqrt{km}} \tag{4. 23}$$

Work dissipated by air damping and the electrostatic work supplied to the scanner at the IP- resonance mode is shown in Figure 4.8 (a). Horizontal axis of the figure is drawn with respect to mechanical scan angle of the outer frame. Note that, at the IP- resonance mode, the deflection of the inner frame equals to the deflection of the outer frame. In Figure 4.8 (a) red lines show the electrostatic work due to different drive voltages and blue line shows the damping work dissipated in the system. As shown in Table 4.1, with 14 Vpp drive voltages, 1.5° MSA is achieved as a result of the transient analysis. As seen in the figure, 1.5° MSA is achieved with around 12 Vpp.

Drag coefficient (C_d) is analyzed to find out its deflection dependence. First, damping work is found by using experimentally found quality factors. Second, (4.20) is used accepting Cd equal to one and drag work is calculated. Then the difference between these two damping calculations is found and the difference is fitted with an equation as illustrated in Figure 4.8(c). This fit function gives the deflection dependent drag coefficient. Figure 4.8(b) shows the experimentally found damping work and the drag work which is calculated with the fitted drag coefficient.

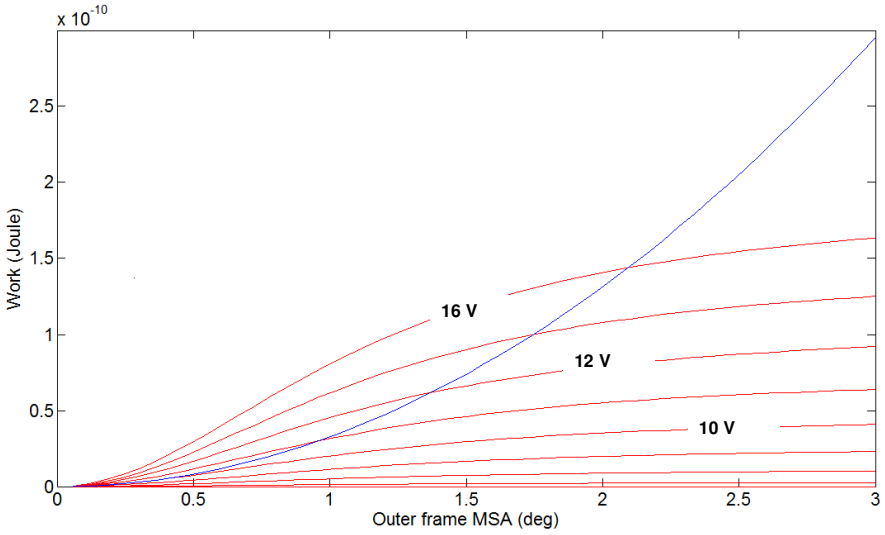

(a)

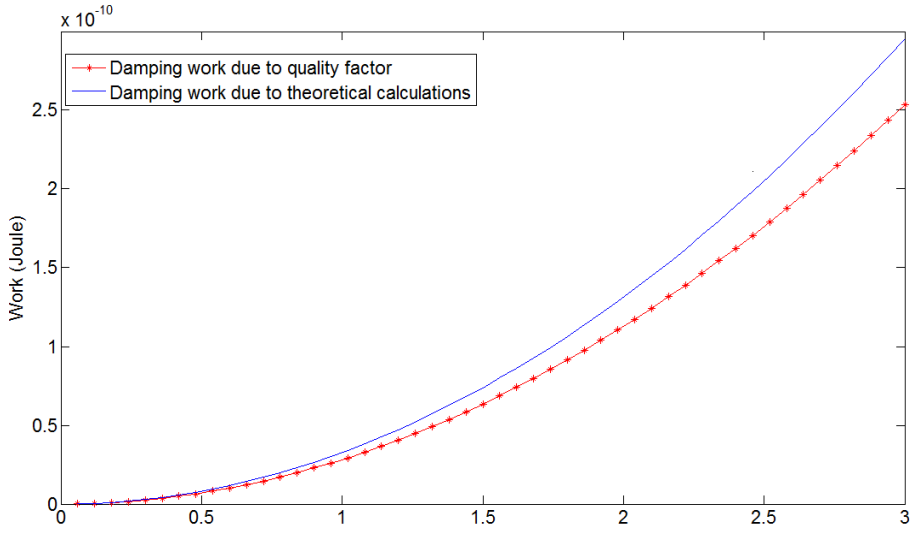

(b)

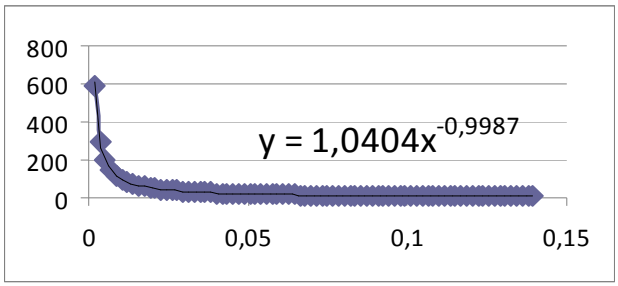

(c)

Figure 4.8: IP- resonance mode (a) Red lines represent the electrostatic work with respect to different drive voltages; blue line represents the dissipated work by air damping. (b) Blue line represents damping work found due to (4.22), red line represents the damping work calculated with respect to experimentally obtained quality factors (c) Fit function used to find the drag coefficient [Wyatt Davis, Microvision Inc. personal communication, 2008]

Same analysis is repeated in order to find the damping characteristic of the device at the OP-resonance mode. As shown in Figure 4.9, approximately 2.5 ° outer frame MSA is achieved with 500 Vpp voltages while it is found 600 Vpp voltages by transient analysis in

Table 4.2. Since at the OP- resonance mode, the inner and the outer frames move out of phase, different drag coefficients must be calculated for each. Fit function of the drag coefficient and the fitted damping work is shown in Figure 4.9 (c) and (b). Mechanical coupling efficiency is 21 in these analyses.

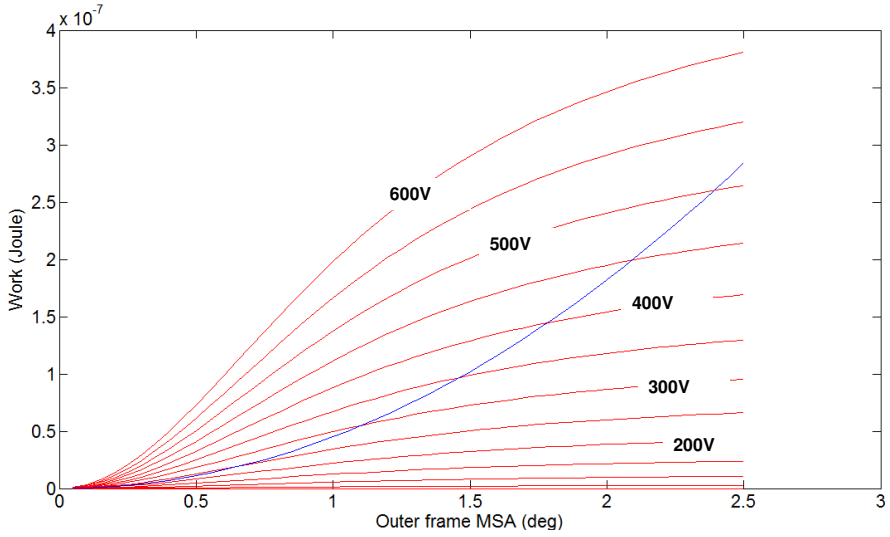

(a)

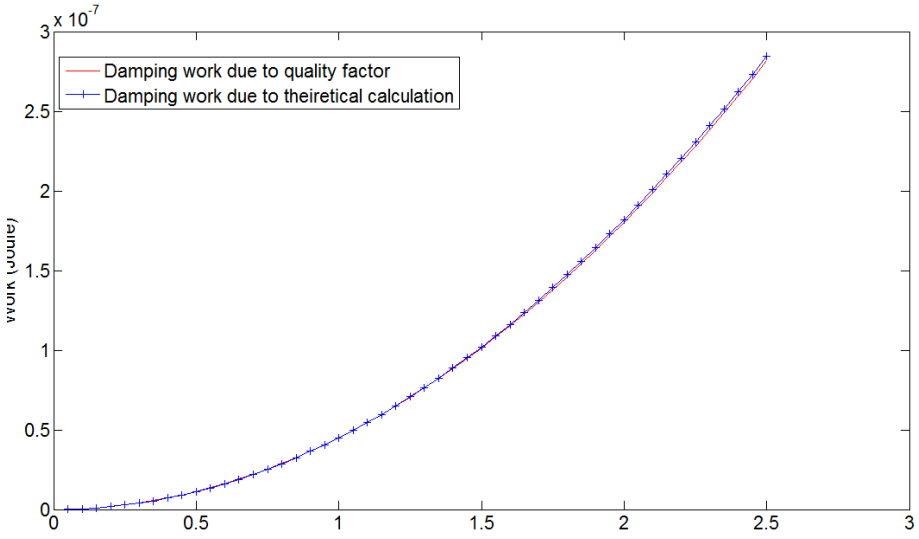

(b)

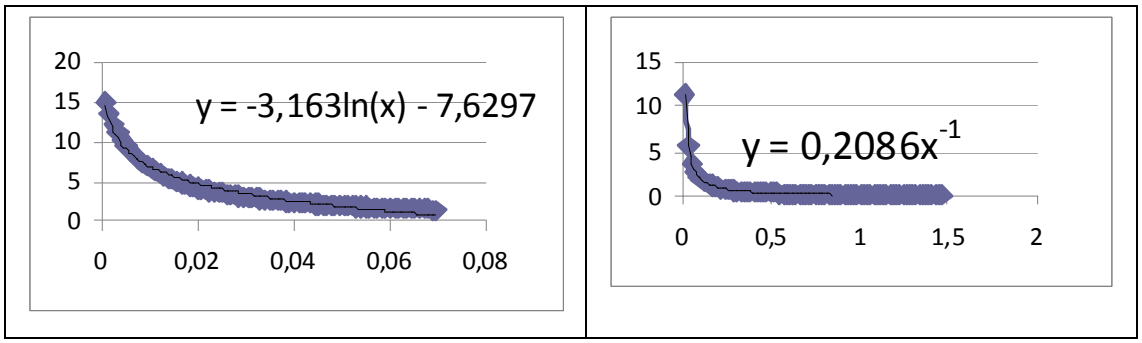

(c)

Figure 4.9: OP- resonance mode (a) Red lines represent the electrostatic work with respect to different drive voltages; blue line represents the dissipated work by air damping. (b) Blue line represents damping work found due to (4.22), red line represents the damping work calculated with respect to experimentally obtained quality factors (c) Fit functions used to find the drag coefficient for plate and mirror. [Wyatt Davis, Microvision Inc. personal communication, 2008]

4.4 Torsional Scanner Redesign Results

Mechanical and electrostatic analyses of the fabricated torsional scanner are discussed in the previous sections. The minimum required drive voltage is found to be 260 Vpp to start the oscillations at the OP- resonance mode. In order to decrease the power consumption to achieve 18º inner frame MSA at 24 kHz, the torsional scanner design is revised. 3D illustration of the torsional scanner is shown in Figure 4.10. The geometrical form of the revised scanner is the same with the first fabricated device but some of the dimensions are changed. Main modification on the scanner is the longer comb fingers. In the fabricated device, comb finger length of the new torsional scanner design is 160 um with 150 um comb overlap while comb finger length of the fabricated device is 50 um. Comb width and comb pitch is not changed. Since the outer frame length is increased from 2.8 mm to 3.2 mm, number of comb fingers are used in the device is increased.

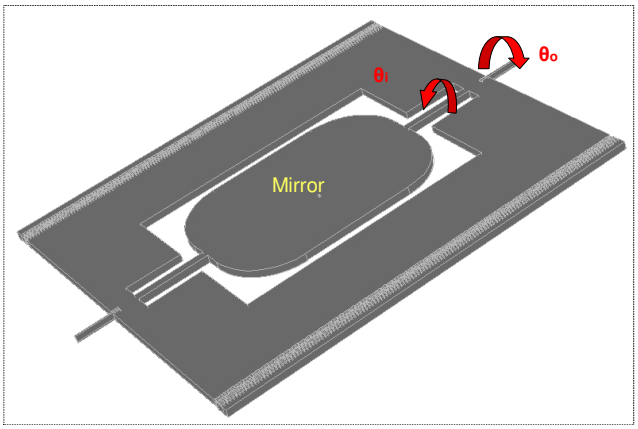

Figure 4.10: 3D illustration of the torsional scanner

Since the number of the comb fingers and the comb overlap is increased; capacitance variation in the system is also increased. Geometrical dimensions of the revised design are shown in Table 4.3.

Parameter		Dimension (um)
W	Inner frame width	1500
L	Inner frame length	1000
İfrw	Inner frame thickness	50
İfll	Inner flexure length	655
İflw	Inner flexure width	50
Ofrw1	Outer frame width1	750
Ofrw2	Outer frame width2	300
ofll	Outer flexure length	300
oflw	Outer flexure width	12
Cl	Comb finger length	160
Cw	Comb finger width	5
Cg	Comb finger gap	5

Table 4.3 Geometrical dimensions of the revised scanner

Analytical analysis, numerical analysis and the FEM of the design performed and explained in this section.

Frequency response of the torsional scanner is obtained with harmonic analysis using MATLAB and illustrated in Figure 4.11. IP- and OP- mode resonance frequencies are found at 1.3 kHz and 22.57 kHz, respectively. Rotational mechanical coupling efficiency is found 16 for this design.

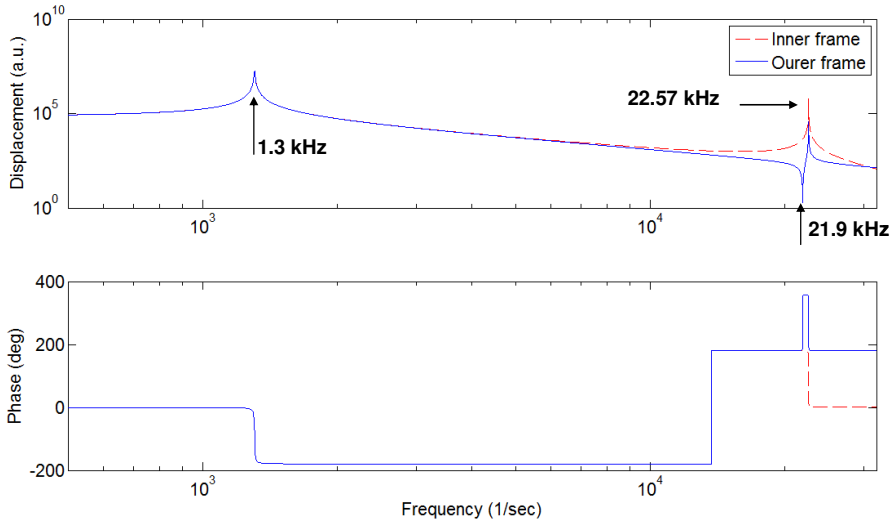

Figure 4.11: Frequency response of the revised scanner performed using MATLAB simulation tool

OP-mode resonance frequency of the scanner is found using ANSYS, as well. Since in this thesis, OP-frequency of the torsion mode is interested, for the revised structure, only modal analysis and the stress analysis of the OP- resonance mode are illustrated in Figure 4. 12.

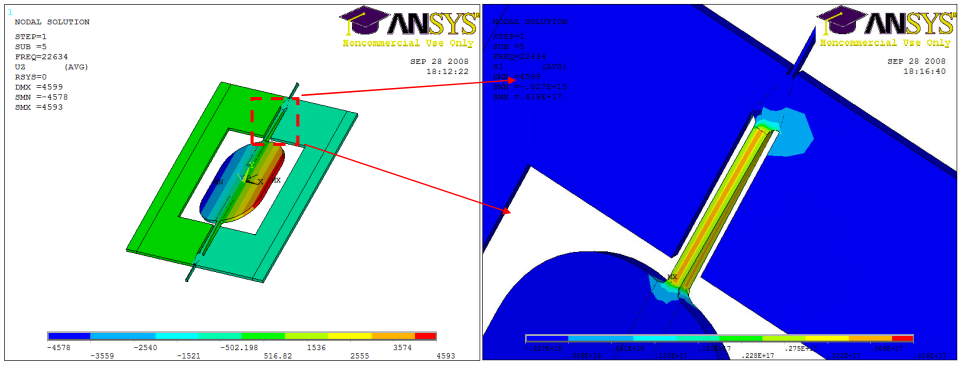

Figure 4. 12 Modal and stress analyses results obtained using ANSYS.

OP- mode frequency is found at 22.6 kHz and for 18º inner frame MSA, the maximum stress at the connections of the inner flexures with the frames is found to be 1.35 GPa. During the revision of the scanner, inner flexure length is increased to decrease the stress. However, length of the inner flexure can not be increased drastically since longer flexures result in longer devices, consequently in bigger device area. Moreover, device dimensions should be adjusted carefully to achieve the required mode frequencies, proper mode separation and the mechanical coupling efficiency.

Stability analysis of the revised device is performed with respect to two different quality factor sets. First, quality factors found experimentally for the fabricated torsional devices are concerned. Then, device performance is analyzed in higher damping circumstances. Voltage stability results of the OP- resonance mode are shown in Table 4.4 and Table 4.5.

Vp-p	f_1	IF_MSA (deg)	OF_MSA(deg)
300V	45155	60.50	3.700
200V	45155	44.11	2.690
100V	45158	18.88	1.170
80V	45158	10.50	0.635

Table 4.4 Deflection amplitudes at the OP- resonance mode, low damping case (IP-mode quality factor=237, OP- mode quality factor=2325)

Vp-p	f_1	IF_MSA (deg)	OF_MSA (deg)
300 V	45183	30.22	1.820
200V	45195	18.02	1.112
150 V	45200	7.64	0.490

Table 4.5: Deflection amplitudes at the OP- resonance mode, high damping case (IP-mode quality factor=50, OP- mode quality factor=500)

Vp-p	f_1	MSA (deg)
300 V	45145	14,8
200 V	45144	13,6
150 V	45144	12
100 V	45144	9,6
80V	45144	8,8
60 V	45145	6,8
40 V	45146	4,8
20V	45151	2,08

Table 4.6: Deflection amplitudes for single frame scanner

Quality factor for IP- and OP-resonance modes are assumed to be 237 and 2325, respectively at

Table 4.4. These are same with the experimentally obtained results of the fabricated device. To start the oscillations at the OP resonance frequency of the revised device, the minimum voltage is reduced 80 Vpp from 260 Vpp. The revised device can be driven with significantly lower voltages compared to the first fabricated devices. Moreover, 100 Vpp voltages are enough to have 18º inner frame MSA which meets the needs of the application.

Table 4.5 shows the deflection with respect to various drive voltages for higher damping case. Quality factor of the IP- resonance and the OP- resonance modes are assumed as 50 and 500, respectively. As seen in the table, minimum required voltage is 150 Vpp voltages in this case and to achieve 18º inner frame MSA, 200 Vpp is required instead of 100 Vpp.

To compare the demonstrated 2-DoF torsional scanners with single frame scanners, the deflection analysis of the single frame torsional scanner is performed by keeping the mirror (inner frame in 2-DoF systems) dimensions and resonance frequency constant. Experimentally measured quality factor is again used in this analysis. As seen in Table 4.6, in order to achieve 18º mirror MSA in 1-DoF systems, the scanner must be driven higher than 260 Vpp while in 2-DoF system, 100 Vpp supply voltage was sufficient. The main advantage of the 1-DoF system is that the oscillation can be started at relatively low voltages.

In this analysis, it should be noted that, combs disengage with 2.7º outer frame deflection. Before the fingers disengage, displacement changes quadratically with the applied voltage and changes linearly when the combs start to disengage. Displacement variation with respect to the applied voltages agrees with the theory.

In torsional scanners, in addition to voltage stability and stress limitations, pull- in is a serious problem as well. Pull in problem of the comb drive torsional scanners is different than that of in- plane devices. In this case, adjacent comb finger may stick to each other due

to various reasons. First reason is the poor mode separation. If the torsion mode and the in-plane rocking mode of the device are too close to each other, then at the torsion mode, comb fingers can stick to each other.

Another reason of the pull- in problem arises because of the comb fingers at the corners of the device (Figure 4.13). Comb fingers at the corners experiences electrostatic force only at one side. When damping force is defeated by the electrostatic force, the movable comb finger sticks to the fixed one.

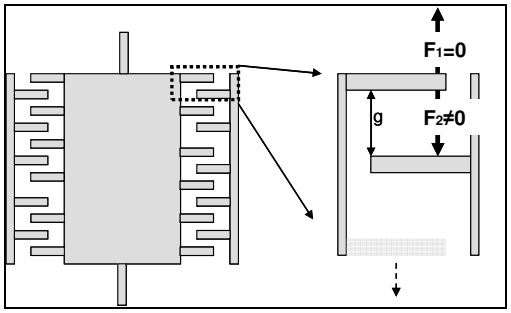

Figure 4.13: 2D illustration of the comb actuated torsional scanner and the force in-equilibrium at the corner fingers

In this pull- in problem, only the movable comb finger bends like a uniform force exerted cantilever beam as illustrated in Figure 4.14. Since one side of the beam is anchored, parallel plane pull- in approximation can not be used here. In this situation, while the beam bends, electrostatic force exerted on the beam changes along the length of the finger. Since, it is very hard to analyze the situation analytically, so FEM is performed with ANSYS to find the pull- in voltage (V_{pi}) for fingers with different length and width and the results are shown in Figure 4.15. The revised design has comb fingers with 5 um width and 160 um length and the pull in voltage is found to be 300 V (Figure 4.15 (a)). To increase the pull in voltage, it is sufficient to increase the width of the comb finger at the corner of the device only. Figure 4.15 (b) is plotted for the comb finger with the same

length but 7 um width and pull in voltage is increased to 480 V. Another analysis is performed to see how the pull in voltage changes with the comb finger length. This time comb width is kept 5 um and comb length is increased to 300 um and pull in voltage is found to be 90 V. This result shows that, since the stiffness of the comb finger decreases with increasing comb length, pull in voltage decreases to very low values. This difficulty can be solved again by increasing the width of the fingers.

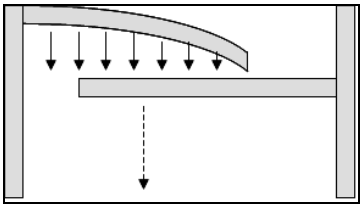

Figure 4.14 Pull- in problem due to the electrostatic force at the corner fingers

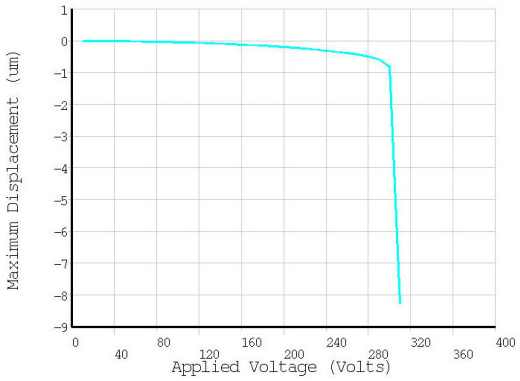

(a)

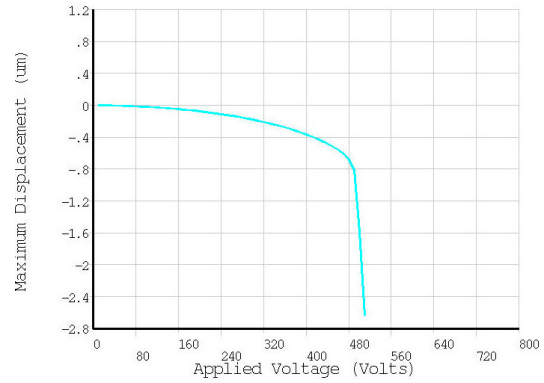

(b)

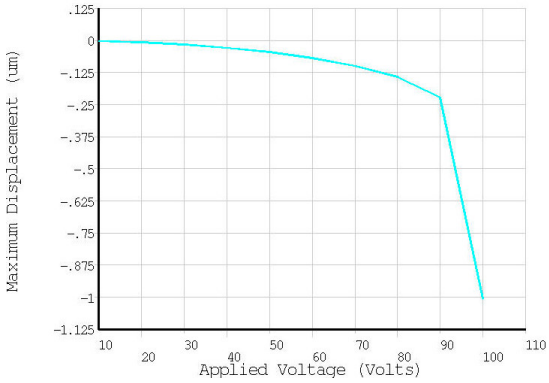

(c)

Figure 4.15: Pull in voltage analysis: a) V_{pi}=300 V with 5 um comb width and 160 um comb length, (b) V_{pi}=480 V with7 um comb width and 160 um comb length. (c) V_{pi}=90 V with 5 um comb width and 300 um comb length

As stated above, analytical investigation of pull-in is hard to achieve. However, by using parallel plate capacitor approximation, for uniformly distributed force, pull in voltage is found for 160 um and 300 um length comb finger with respect to different comb widths and plotted in Figure 4.16. Analytically obtained results are very close to FEA results. For the first case, pull in voltage is found to be 300 V, for the second case pull- in voltage is found to be 498 V and for the last case pull- in voltage is found to be 85 V. Since these

results are very close to FEA results, it can be stated that, parallel plate approximation is a very good approximation in this system.

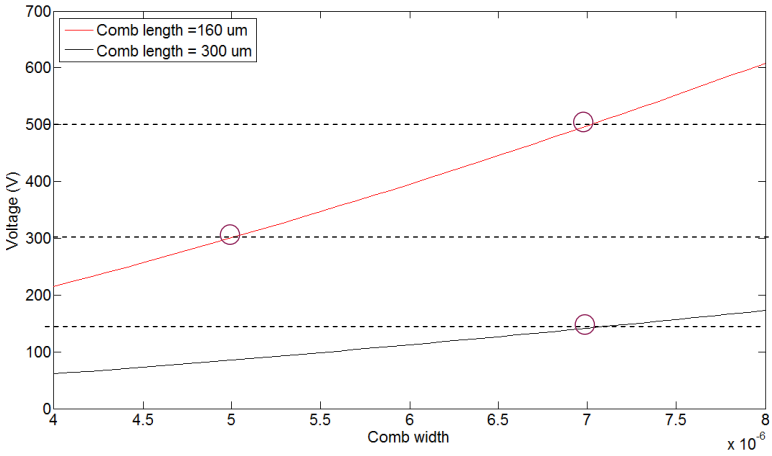

Figure 4.16: Pull in voltages calculated with parallel plate assumption, red line represents the comb fingers with 160 um length and the black line represents the comb fingers with 300 um length

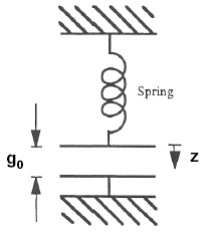

Figure 4.17: Modeling of parallel plate capacitor

DC dynamic pull in problem of the parallel plate capacitor (Figure 4.17) is investigated in chapter 2. To find the pull in voltage (2.7), stiffness of the structure in the direction of the deflection should be found first. For the cantilever beam shown in Figure 4.18, the stiffness of the device is found for uniformly distributed load as follows:

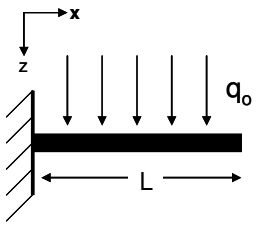

Figure 4.18: Cantilever beam under distributed load

$$\frac{d^4 w(x)}{dx^4} = \frac{q_o}{EI} \tag{4. 24}$$

where w(x) is the deflection amplitude in z direction and represented as third order polynomial function of x, E is the Young's Modulus, I is the area moment of inertia and q_o is the distributed force.

$$w(x) = A + Bx + Cx^2 + Dx^3 \tag{4. 25}$$

To solve the deflection function, first uniform distributed load is replaced by an equivalent external force at the tip of the beam. (4.25) is integrated four times and boundary conditions are applied.

$$F_{eq} = q_o L \tag{4. 26}$$

First integration:

$$EI \frac{d^3 w}{dx^3} = q_o x + C_1 = -F_{eq} \tag{4. 27}$$

At x=0, $F_{eq} = q_o L$,

$$C_1 = -q_o L \tag{4. 28}$$

Second integration:

$$EI \frac{d^2 w}{dx^2} = \frac{q_o x^2}{2} - q_o L x + C_2 \tag{4. 29}$$

At x= 0, M= 0 ($M = -EI\frac{d^2w}{dw^2}$), C_2=0

where M is the external moment.

Third integration:

$$EI\frac{dw}{dx} = \frac{q_o x^3}{6} - \frac{q_o L x^2}{2} + C_3 \tag{4. 30}$$

At x=0, $\frac{dw}{dx} = 0$ then C_3=0

After fourth integration w(x) is given as:

$$w(x) = \frac{q_o x^4}{24} - \frac{q_o L x^3}{6} \tag{4. 31}$$

Stiffness of the beam in +z direction is found by calculating maximum deflection which is obtained at the tip of the beam where x=L

$$w(L) = -\frac{q_o L^4}{8EI} \tag{4. 32}$$

$$k = \frac{F_{eq}}{w(L)} \tag{4. 33}$$

Using (4.33), spring constant is found as:

$$k = \frac{8EI}{L^3} \tag{4. 34}$$

Note that, in these calculations, during the deflection, equivalent force does not change. Thus, despite electrostatic force changes during bending, in the analytical pull- in voltage calculation of the comb fingers at the corners, force assumed not changing and (4.34) is substituted directly in (2.7).

Chapter 5

INTEGRATION OF POLYMER WAVEGUIDES ON FR4 SCANNERS

5.1 Polymer Waveguide and LED Array Integration on FR4 Scanner

A polymer waveguide is integrated together with a light emitting diode (LED) on top of the FR4 polymer scanner to realize functionalities such as optical interconnects and imaging. The scanner is actuated in torsional mode using moving magnet electromagnetic actuation. The permanent magnet is integrated on the back side of the scanner and the external magnetic field is exerted by the electro- coil. Magnetic field amplitude is adjusted by the current through the coil.

5.1.1 FR4 Scanner

FR4 is the most widely used material for printed circuit boards (PCB) which has good electrical, thermal and mechanical properties. Micromechanical devices can be fabricated with high-precision and low cost on PCB which also enables integration of mechanical, optoelectronic, magnetic, electrical and micro-optic devices. Fabrication of the FR4 structures is easier in comparison with the MEMS structures, since only standard PCB machinery is required for fabrication of FR4 structures [53].

5.1.2 Waveguide Fabrication at Heriot Watt University and LED Array Integration on FR4 Scanner

In this thesis, magnetically actuated FR4 scanners are used to integrate polymer waveguides and LED arrays. Magnetically actuated FR4 scanner is illustrated in Figure 5.1. A permanent magnet is attached on the bottom side of the scanning platform and the external magnetic field is generated by the electrocoil placed underneath the scanner.

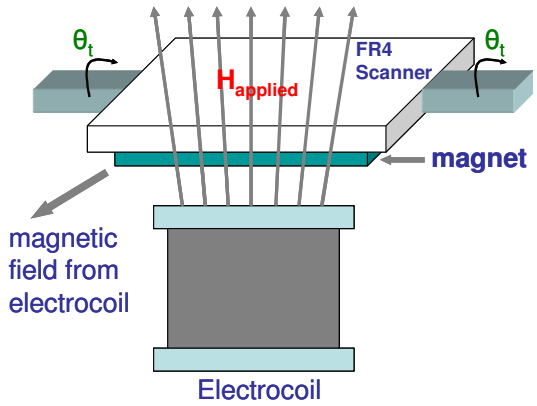

Figure 5.1: Magnetically actuated FR4 scanner and the driving electro-coil.

LED array integrated FR4 scanner is illustrated in Figure 5.2. The system designed in Optical Microsystems Laboratory and the wire bonding is done in Aselsan, Turkey. A one dimensional LED array is mounted on a 13 mm x 13.5 mm FR4 platform [54] and driven by an external circuitry. 220 um X 220 um size LEDs are received from OSRAM. There is an electronic contact on the middle of the 70 um diameter circular light emitting surface on top of the LED. This contact is wire bonded to the electrical connections and used as the independent cathode. LEDs are connected to the conducting trench using an electrically conducting epoxy.

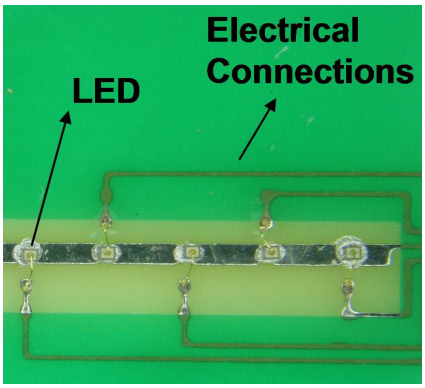

Figure 5.2: LED array integrated FR4 scanner

The polymer waveguide is fabricated at Heriot Watt University [55] by direct laser writing method using the design requirements defined by the Optical Microsystems Laboratory. The waveguides have 220 um x 220 um size core and PMMA substrate as undercladding. The refractive index of the core is 1.57 while the refractive index of the cladding is 1.52. A channel is opened in the PMMA to place the LED together with the wire bonding as illustrated in Figure 5.3. 45º mirror is fabricated on the waveguide in order to maximize the coupled light by utilizing the total internal reflection.

Instead of the standard photolithography, direct laser writing method is used to fabricate the polymer waveguides without using masks. Mask fabrication is expensive and increase the process time. Using direct laser writing method, in the processes which require multiple mask steps, mask alignment issue can be eliminated. UV sensitive polymer materials are used in the direct laser writing systems. UV exposed areas are hardened and the remaining parts are removed. The direct laser writing method is illustrated in Figure 5.4. Polymer waveguides can be fabricated by laser ablation [56] and hot embossing techniques, as well. Polymer materials are promising materials with their good chemical and environmental resistance. Polymer waveguides has many advantages such as low attenuation, high bandwidth, low cost, high flexibility and portability of manufacturing PCB. Polymer waveguides find applications in high speed data transmission in electronic systems utilizing

vertical cavity surface emitting lasers (VCSEL) and photodiodes. The loss of the polymer waveguides is reported 0.05dB/cm at 850 nm in [57]. Another possible application is integration of the polymer optical waveguides with hermetically sealed fluidic channels [58].

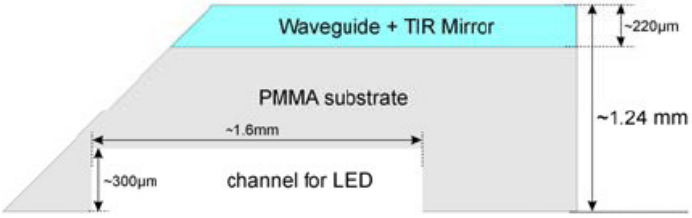

Figure 5.3: The waveguide specifications mounted on top of the FR4 scanner

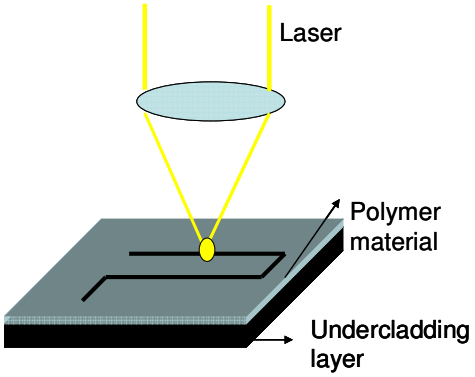

Figure 5.4 : UV light emitted by laser cures the polymer material

The polymer waveguide is aligned with the LED, which is integrated on the FR4 scanner. After completing the alignment, the waveguide is glued on the LED with a UV curing transparent epoxy. The magnetically actuated FR4 scanner integrated with the polymer waveguide and the LED array is illustrated in Figure 5.5

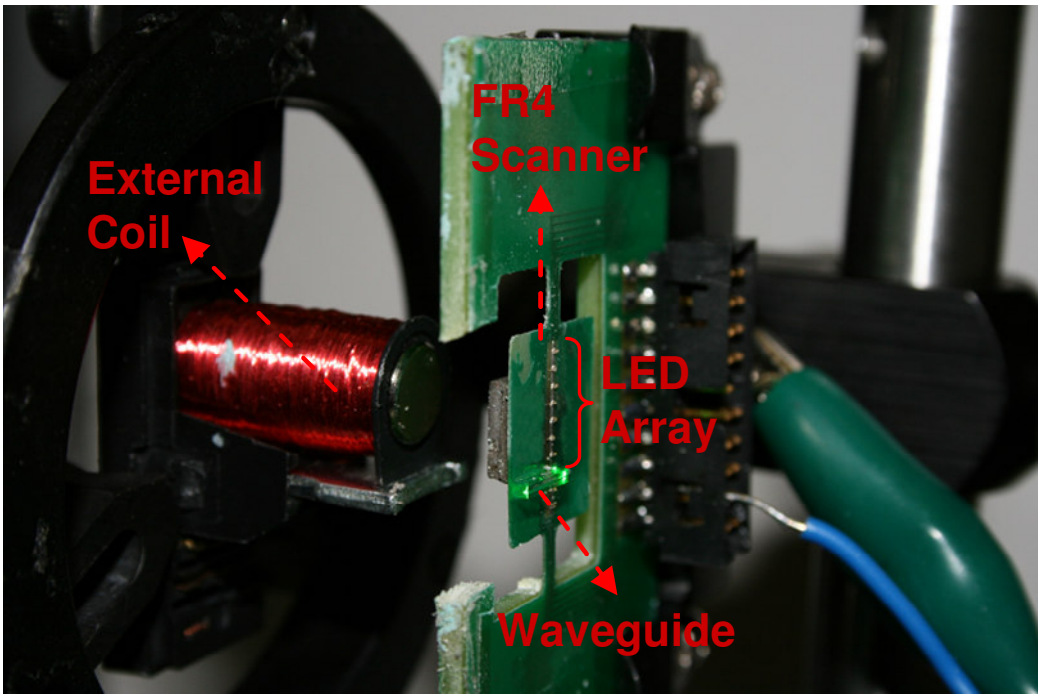

Figure 5.5: Waveguide integrated FR4 scanner is actuated with an external electro- coil. The waveguide is coupled only one LED in the array.

ANSYS software is used to model the scanner assembly including the FR4 scanner, the polymer waveguide and the permanent magnet. The LEDs are not included to the modal analysis since they are on the torsional axis and do not contribute to the inertia. The modal analysis result is shown in Figure 5.6. The torsional mode frequency is found to be 171.75 Hz. Waveguide integrated scanner is actuated with electro-coil with 10 V drive voltage at the natural frequency of the torsional scanner. Experimentally, the torsional mode is found at 161 Hz. Figure 5.7 illustrates a bright line of light which can be seen in the middle corresponds to the core of the waveguide. The length of the scan light is measured 5.3 mm corresponding to 40º total optical scan angle (TOSA) [59].

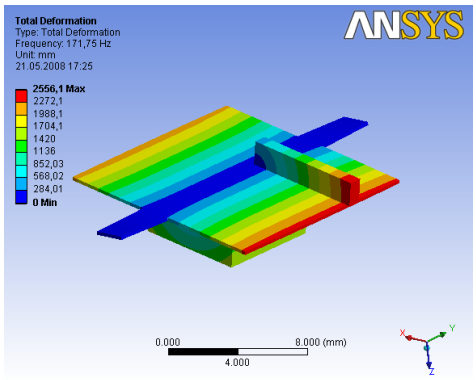

Figure 5.6: Torsion mode analysis of the polymer waveguide integrated FR4 scanner using ANSYS Software

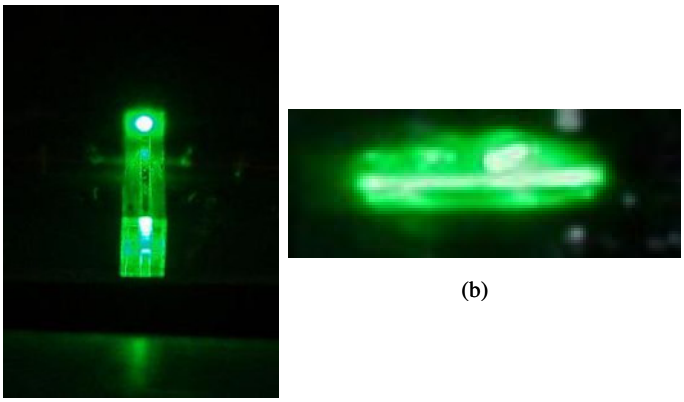

(a) (b)

Figure 5.7: (a) Top view of the waveguide. The bright spot closer to camera (bottom of picture) is the light output from the waveguide, the top bright spot is the reflection from the 45º mirror that is not guided (b)Scan line generated in torsion mode captured by directly imaging the output of the waveguide illustrating several mm edge deflection and rotation capability of the FR4 stage.

LED is preferred in this system as light source to enable certain display applications because they provide large color gamut, low-cost, simple integration and high efficiency. For optical interconnects, vertical-cavity surface-emitting lasers (VCSEL) seem more

suitable to integrate on FR4 with waveguides for better coupling efficiency and high modulation rates.

5.2 Polymer Waveguide and Maskless Lithography Setup

In Optical Microsystems Laboratory, as a part of the endoscopic camera project, a maskless lithography setup is built to write waveguides using polymer materials and the setup illustrated in Figure 5.8. In the system, a UV laser is used to cure the polymer materials which emit light at 408 nm.

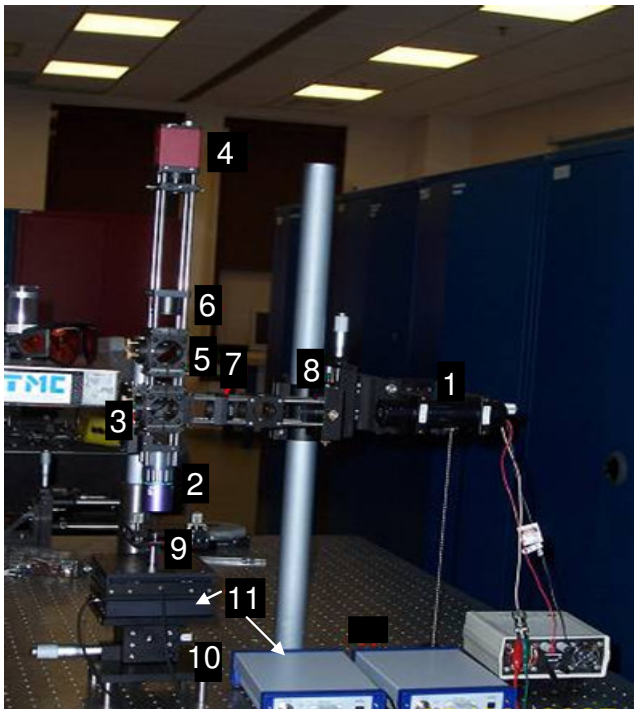

Figure 5.8: Maskless lithography setup

Components of the maskless lithography setup are:

1. 20 mW, 408 nm UV-visible laser.
2. Mitutoyo infinity- corrected long distance 20X objective.
3. Dichroic beam.
4. AVT Marlin F131 camera.
5. Beam splitter: A white light source is used in the system to illuminate the sample while the process is recorded by the camera.
6. Tube lens is used to collect the reflected light on the camera.
7. 100 mm focal length lens is used to collimate the light emitted by the laser.
8. 30 um diameter filter.
9. Tip- tilts stage.
10. Vertical translation stage with 1um sensivity.
11. Computer controlled piezo stages used for nanopositioning in x and y axes with 100 mm travel range and 100 nm resolution.

The UV light is first filtered and collimated by the lens. The collimated beam is focused on the sample by infinitely- corrected objective after reflected from the dichroic beam splitter. A colored camera is used to record the laser writing process. Therefore, a white light source and a beam splitter are used to image the sample surface on the camera. The tube lens is used to focus the reflected light on the camera with 20 X magnification. The beam splitter is used to direct the white light reflected from the sample surface to the camera. The manual stages are used to adjust the sample position at the focal plane of the objective. The expected pattern is cured by the computer controlled piezo stages which are used to move the sample in x and y axes. In this system, a beam shaping component is not used so that fabricated samples are shaped directly by the Gaussian profile of the beam.

Before fabricating the waveguides, in order to calibrate the cure speed and the focus laser beam size, AZ 9260 and AZ 5214 E positive photoresists are spinned on the substrate. Positive photoresists are the polymers in which the portion of the photoresist that is exposed to the light becomes soluble and can be removed by the developer. So that, the trenches are obtained on the photoresist layer after the development step. The fabricated structures using AZ 9260 photoresist are illustrated in Figure 5.9. Surface profiles of the trenches are shown in Figure 5.10. The trench widths are 58 um, 125 um and 136 um. The length and depth of the trenches are 5 mm and 10 um, respectively.

AZ 5214 E photoresist can be inverted from positive to negative by applying additional baking steps. However, only thin layers can be obtained by this type of photoresist. The laser writing process is performed using the developed photoresist. Microscope picture of the fabricated structure and the surface profile are shown in Figure 5.11 and Figure 5.12. The width and the thickness of the waveguide are 37 mm and 1 um, respectively.

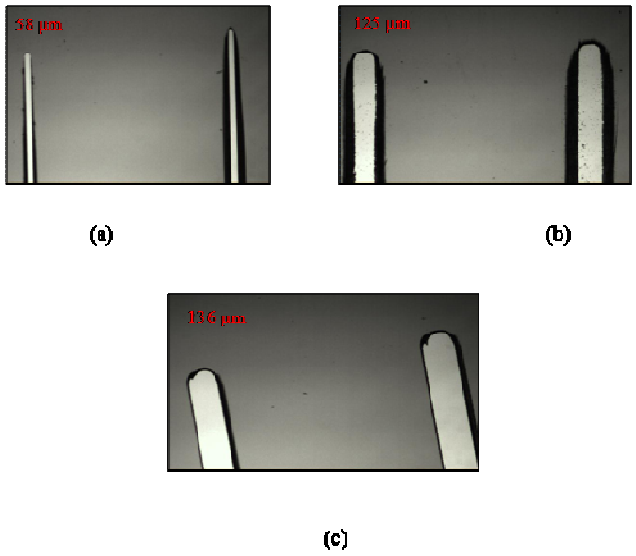

Figure 5.9: Microscope picture of (a) 58 um width, 5 mm length trench. (b) 125 um width, 5 mm length trench, (c) 136 um width, 5 mm length trench

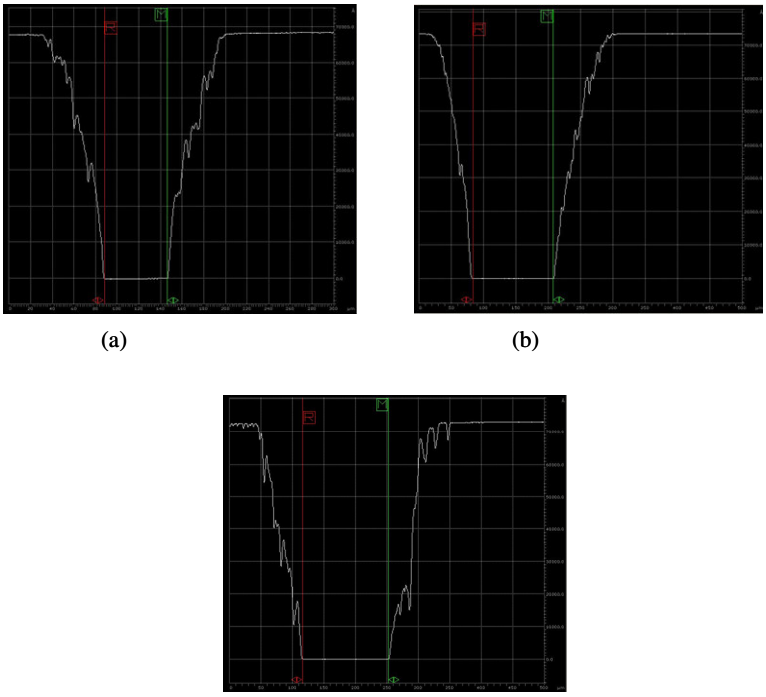

(a) (b)

(c)

Figure 5.10: Surface profile of (a) 65 um width, 5 mm length trench. (b) 125 um width, 5 mm length trench, (c) 136 um width, 5 mm length trench.

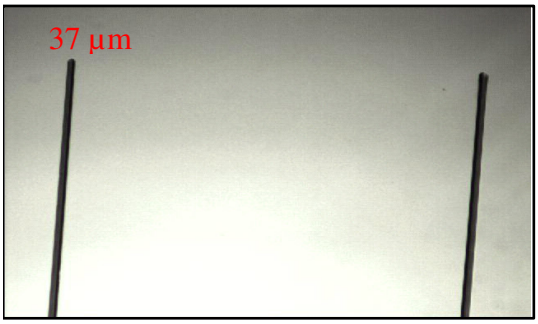

Figure 5.11: Microscope picture of 37 um width, 5 mm length waveguide.

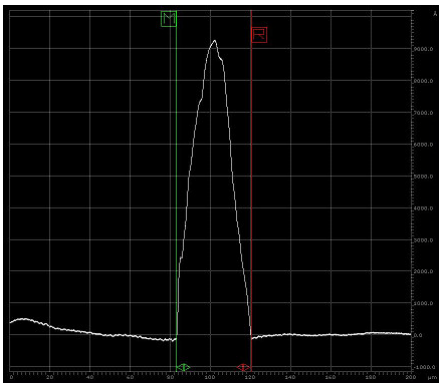

Figure 5.12: Surface profile of 37 um width waveguide

As stated above, these fabricated structures are used only define the Gaussian beam profile of the laser. Since the maskless laser writing project is finalized, actual waveguide fabrication is aborted.

Chapter 6

CONCLUSIONS

In this work, a novel actuation technique is proposed for comb drive MEMS scanners. Numerical and analytical modeling is performed for both translational (in-plane and out-of-plane) and torsional scanners and the results are compared with the experimentally obtained data. The translational scanners are presented to have applications in endoscopic imaging while the torsional scanners are designed for the laser scanning display applications.

In this new actuation mechanism, an additional frame is defined around the inner frame of the scanner and the electrostatic comb drives are only present on the outer frame. A small deflection of the comb fingers transferred to the inner frame with a mechanical coupling efficiency, which is the ratio of the two frame deflections. Analytical formulas for the mechanical coupling efficiency are derived.

For torsional scanners and out-of-plane translation stages, the damping losses become a limiting factor particularly when the comb fingers are disengaged during deflection. Main advantage of this mechanism is that the outer frame deflections, and the damping, can be kept small while achieving large deflections in the inner frame. The proposed scheme is also well-suited for in-plane sliding devices as the comb fingers can be kept much shorter due to small deflections at the combs, significantly reducing the risk of lateral pull-in at the comb fingers. Utilizing the developed mechanism, larger deflection amplitudes can be obtained at high frequencies using lower driving voltages compared to single frame scanners.

Mainly three different types of silicon MEMS scanners are demonstrated. The harmonic and the transient analyses of the 1D in-plane and the torsional scanners are performed using both ANSYS and MATLAB software and compared with the experimental results. While the numerical results of the 1D in-plane devices are verified with the experimental data, same agreement could not be achieved with the torsional scanners. Thus, to find out the reason of the discrepancy, voltage stability analysis and the damping of the torsional scanners is performed and the minimum required voltage is found. Since most of the 2D linear devices are broken due to their narrow and long flexures, only numerical results are included in the thesis. Future work includes fabrication of the redesigned torsional scanners with lower actuation voltages to avoid stability and pull-in problems.

In addition to the silicon microscanners work, laser writing setup is developed and micro-optical waveguides made at Heriot-Watt University are integrated with FR4 mechanical scanning stages developed in our laboratory to achieve scanning with LEDs as an alternative to silicon based scanners.

The contributions of the thesis are listed as;

- 1D linear devices are characterized and 9 um zero-to-peak deflection is obtained at 100 V peak-to-peak voltage.
- Numerical and analytical analyses of the mechanical coupling principle are performed and the mechanical coupling efficiency and the inner frame deflection are optimized.
- 2D linear devices are designed and modeled.
- 1D torsional scanners are designed, modeled and tested.
- Voltage stability and damping analyses of the 1D torsional scanners are performed.
- Pull-in analysis of the comb drive scanners arises due to the electrostatic imbalance at the corner fingers is analyzed.

- The LED array and the polymer waveguide are integrated on the FR4 scanner and the system is tested.
- The maskless lithography system is built and first samples of polymer structures are fabricated.

Appendix A

THE CHARACTERIZATION SETUP

A characterization set up is built to measure the frequency and voltage responses of the microscanners and MATLAB programming tool is used to collect and process the data. In frequency response analysis, frequency of the driving signal is swept up and down and the corresponding deflection amplitude and phase are recorded. As illustrated in Chapter 3, two different resonance frequencies are obtained at each vibration mode of the scanners. The laser spot is focused on both the outer and inner frames to find the IP- and OP- resonance frequencies and the mechanical coupling efficiency is derived using the peak amplitudes at the OP- resonance mode.

To plot the voltage response of the scanners, at the given driving signal, maximum deflection of the scanner is obtained at both IP- and OP- resonance frequencies. At each driving signal, the resonance frequencies of the scanner shift. Therefore, at different voltage amplitudes, the frequency response of the device is recorded and the frequency shift is plotted, as well.

The experimental set up used for characterization of the microscanners is illustrated in Figure A.1. Despite a common characterization setup is used for both in-plane and torsional scanner, the measurement techniques are different and illustrated separately in the figure.

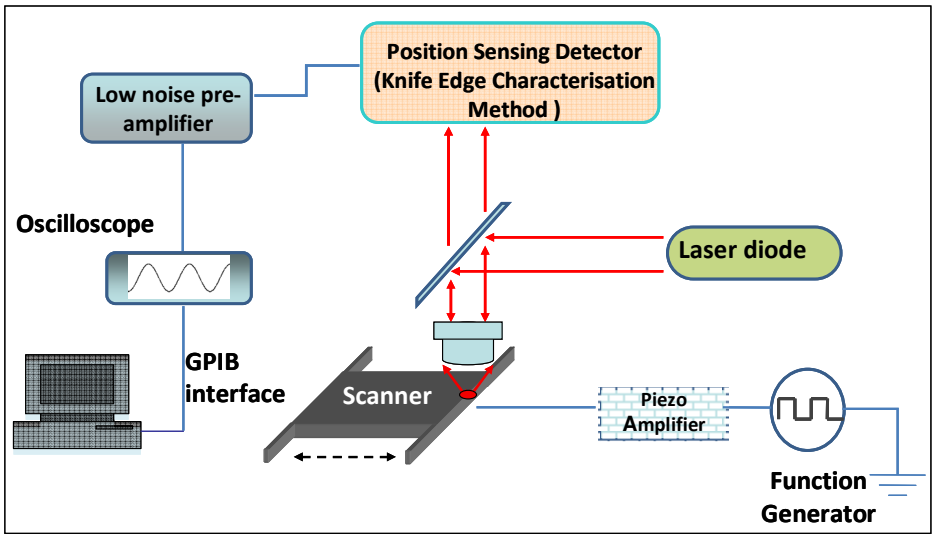

(a)

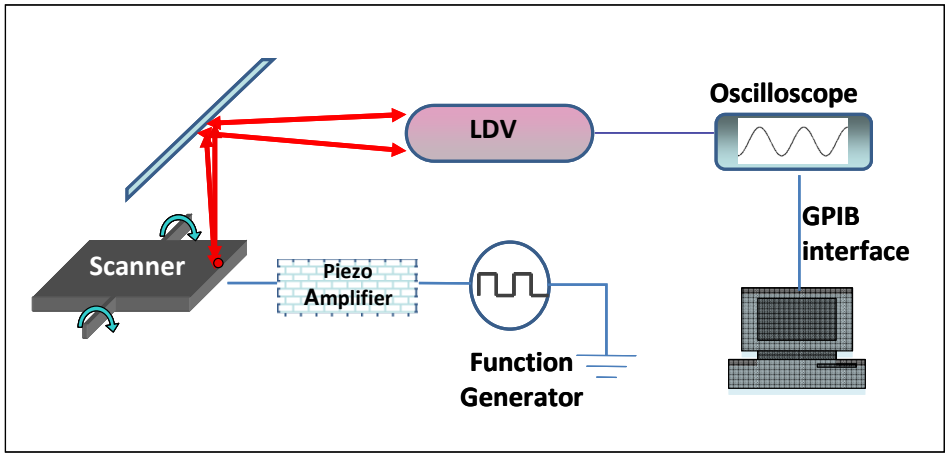

(b)

Figure A.1: The characterizations setup of the microscanners (a) Measurement of the in-plane sliding device (b) Measurement of the torsional scanner

The components of the experimental setup used for characterization of the in- plane devices are illustrated in Figure A.1 (a). MiniLaseCF^{TM} laser diode is used in the experiments which emits 30 mW collimated light at 635 nm. The reflected light is focused

on the detector and the deflection of the scanner is found utilizing the data using knife edge method. TREK PZ0700 piezo-amplifier is used to amplify the output of the function generator to drive the scanners with higher voltages. SRS SR560 low-noise pre-amplifier is used to block the undesired frequency components of the output signal and amplifies the data in the pre-defined frequency bandwidth.

The deflection of the torsional scanners is found using Laser Doppler Vibrometry (LDV) (Figure A.1 (b)). LDV is an optical instrument used to measure the displacement or the velocity of the vibrating structures accurately and without contact [60]. Polytech PDV 100 LDV is used in the experiments, which is capable of measuring velocities between 2 μm/sec and 500 μm/sec. It should be noted that, LDV is only used to measure the deflection amplitude in the OP resonance mode because at this mode scan line could not be obtained. The deflection angle was very small and the returning light did not miss the clear aperture of LDV. As discussed under the damping title, only at the IP resonance mode, considerable scan line can be obtained and the deflection measurement of the mechanical scan angle is done manually. At this mode, LDV is used to obtain the frequency response of the scanner at relatively low voltages.

BIBLIOGRAPHY

[1] H. Urey, "MEMS Scanners for Display and Imaging Applications," *Proceedings of SPIE, Optomechatronic Micro/Nano Components, Devices, and Systems,* vol. 5604, pp. 218-229, 2004.

[2] Y. Ko, J. Chob, Y. Mun, H. Jeong, W. Choi , J. Lee, J. Kim, J. Yoo, J. Lee, "Eye-type scanning mirror with dual vertical combs for laser display," *SPIE Proc. of MOEMS Display and Imaging Systems III,* vol. 5721, pp. 14-22, 2005.

[3] W. Dotzel, T. Gessner, "Silicon Mirrors and Micromirror Arrays For Spatial Laser Beam Modulation," *IEEE Transducers' 97*, pp. 81- 84.

[4] H.Goto, "Two-Dimensional Micro Optical Scanner Excited by PiT Thin Film Microactuator," *SPIE Conference on Optoelectronic Materials and Devices*, vol. 3419, pp. 227- 235.

[5] P. F. V. Kessel, L. J. Hornbeck, R. E. Meier, M. R. Douglass, "A MEMS-Based Projection Display," *Proceedings of The IEEE*, vol. 86, pp. 1687-1704, 1998.

[6] J.Yan, S. Luanava, V. Casasanta, "Magnetic Actuation for MEMS Scanners for Retinal Scanning Displays," *SPIE Proceedings of MOEMS Display and Imaging Systems*, vol. 4985.

[7] H. Urey, "Retinal Scanning Displays", *Encyc. of Optical Engineering*, Marcel-Dekker, 2003.

[8] P. M. Hagelin, U. Krishnamoorthy, J. P. Heritage, O. Solgaard, "Scalable Optical Cross-Connect Switch Using Micromachined Mirrors," *IEEE Photonics Technology Letters,* vol. 12, pp. 882-884, July 2000.

[9] H. Toshiyoshi, H. Fujita, "An Electrostatically Operated Torsion Mirror for Optical Switching Device," *TRANSDUCERS '95,. EUROSENSORS IX,* pp. 297-300, 1995.

[10] Y. Haga, M. Esashi, "Biomedical Microsystems for Minimally Invasive Diagnosis and Treatment," *Proceedings of the IEEE*, vol. 92, pp. 98-114, January 2004.

[11] W. Piyawattanmetha, L. Fan, S. Hsu, M. Fujino, M. C. Wu, P. R Hen, A. D. Aguirre, Y. Chen, J. G. Fujimoto, "Two-Dimensional Endoscopic MEMS Scanner for High Resolution Optical Coherence Tomography," *Technical Digest Series of Conference on Lasers and Electro-Optics (CLEO)*, vol. 1, May 2004.

[12] J. M. Zara, S. Yazdanfar, K. D. Rao, J. A. Izatt, S. W. Smith, "Electrostatic micromachine scanning mirror for optical coherence tomography," *OPTICS LETTERS*, vol. 28, pp. 628-630, April 15, 2003.

[13] H. Ra, W. Piyawattanametha, Y. Taguchi, D. Lee, M. J. Mandella, O. Solgaard, "Two- Dimensional MEMS Scanner for Dual-Axes Confocal Microscopy," *Journal of Microelectromechanical Systems*, vol. 16, pp. 969-976, August 2007.

[14] M.Rajadhyaksha et. al., "In vivo Confocal Scanning Laser Microscopy of Human Skin: Melanin Provides Strong contrast," *The Journal of Investigative Dermatology*, vol.104, pp. 946-952, 1995.

[15] K. B. Sung, C. Liang, M. Descour, T. Collier, M. Follen, R. R. Kortum, "Fiber-Optic Confocal Reflectance Microscope With Miniature Objective for *In Vivo* Imaging of Human Tissues," *IEEE Transactıons On Biomedical Engineering*, vol. 49, pp. 1168- 1172, October 2002.

[16] I. K. Ilev, R. W. Waynant, "Confocal Fiber-Optic Nanobiosensing," *Lasers and Electro-Optics Society, LEOS 2005*, pp. 163-164.

[17] Available online at http://www.uni-mainz.de/FB/Chemie/AK-Janshoff/137_DEU_HTML.php

[18] E. Leclerc, A. Debray, N. Tiercelin, T. Fujii, H. Fujita, "Silicon based optical scanner using PDMS as torsion springs," *IEEE/LEOS International Conference on Optical MEMS,* vol. 18, pp. 95 – 96, 21 Aug. 2003.

[19] Design and Fabrication of polymer micro cantilevers for external magnetic actuation, Msc Thesis, Rahul Bhushan, MIC, DTU, 2007.

[20] P. R. Pattersona, D. Hahb, M. Fujinoc, W. Piyawattanamethab, M.C. Wub, "Scanning micromirrors: An overview," *Proc. of SPIE, Optomechatronic Micro/Nano Components, Devices, and Systems*, vol. 5604, pp. 195-207, 2004.

[21] L. Sun, C. Ru , W. Rong, "Hysteresis Compensation for Piezoelectric Actuator Based on Adaptive Inverse Control," *Proceedings of the 5" World Congress on Intelligent Control and Automation,* pp. 5036-5039, 2004.

[22] H. Toshiyoshi, W. Piyawattanametha, C. T. Chan, M. C. Wu, "Linearization of Electrostatically Actuated Surface Micromachined 2-D Optical Scanner," *Journal of Microelectromechanical Systems*, vol. 10, pp. 205-214, June 2001.

[23] D.W. Lee, T. Ono, M. Esashi, "High-Speed Imaging by Electro-Magnetically Actuated Probe with Dual Spring," *Journal of Microelectromechanical Systems*, vol. 9, pp. 419-424, December 2000.

[24] L. K. Lagorce, O. Brand, M. G. Allen, "Magnetic Microactuators Based on Polymer Magnets," *IEEE Journal Of Mıcroelectromechanıcal Systems*, vol. 8, pp. 2-9, March 1999.

[25] S. O. Isikman, H. Urey, "Dynamic Modeling of Magnetic Film Actuators," *Lasers and Electro-Optics Society, 2007, LEOS 2007,* pp. 912- 913, 2007.

[26] K. C. Maitland, H. J. Shin, H. R., D. Lee, O. Solgaard, R. R. Kortum, "Single fiber confocal microscope with a two-axis gimbaled MEMS scanner for cellular imaging," *OPTICS EXPRESS,* vol. 14, 2006.

[27] W.Y. Oh, B.E. Bouma, N. Iftimia, R. Yelin, G.J. Tearney, "Spectrally-modulated full- field optical coherence microscopy for ultrahigh-resolution endoscopic i maging," *OPTICS EXPRESS,* vol. 14, pp. 2006.

[28] K. Aljasem, A. Seifert, H. Zappe, "Tunable Multi-micro-lens System for High Lateral Resolution Endoscopic Optical Coherence Tomography," *2008 IEEE/LEOS International Conference on Optical MEMS and Nanophotonics, pp.* 44- 45, 2008.

[29] A. Akatay, C. Ataman, H. Urey, "High-resolution beam steering using microlens arrays," *OPTICS LETTERS,* vol. 31, pp. 2861-2863, October 1, 2006 .

[30] K. Hedsten, D. Karlen, J. Bengtsson, P. Enoksson, "Refractive lenses in silicon micromachining by reflow of amorphous fluorocarbon polymer," *Journal Of Micromechanics And Microengineeing,* vol. 16, pp. 88-95, 2006.

[31] Devices, Structures, and Processes for Optical MEMS, PhD Thesis, Hyuck Choo, University of California at Berkeley, 2007.

[32] H. Toshiyoshi, G. D. J. Su, J. LaCosse, M. C. Wu, "Micro Optical Scanners of Photoresist Reflow Lens on MEMS XY-Stage," SEISAN-KENKYU, vol. 53, pp. 91- 95, 2001. 2.

[33] K. Hedsten, C. Ataman, S. Holmstrom, P. Enoksson, H. Urey, "Hot Embossed Microptics In Silicon Micromachining Using A Substrate Bonder*," Proceedings of 19th MicroMechanics Europe Workshop, MME 2008,* pp. 137- 140, 2008.

[34] K. E. Petersen, "Silicon Torsional Scanning Mirror," *IBM J. RES. DEVELOP*. vol. 24 , pp. 631-637, September 1980.

[35] T. Sandner, T. Klose, A. Wolter, H. Schenk, H. Lakner, W. Davis, "Damping Analysis and Measurement for a Comb-Drive Scanning Mirror," *Proc. SPIE*, vol.5455, pp. 147- 158, 2004.

[36] S. Wiak, K. Smólka, "Complex Mathematical Models of Comb Drive Accelerometers," *International Aegean Conference on Electrical Machines and Power Electronics,* pp. 385-392, 2007.

[37] X. Liu, Z.Yang, G.Yan, J. Fan, H. Ding, Y. Liu, " Design and Fabrication of a lateral axis Gyroscope with Asymmetric Comb-Fingers as Sensing Capacitors," *Proceedings of the 1st IEEE International Conference on Nano/Micro Engineered and Molecular Systems,* pp. 762-765, January 2006

[38] V. B. Mungurwadi, U. V. Wali, "Modeling and Simulation of RF MEMS resonator in a hierarchical approach," *International Symposium on Communications and Information Technologies,* pp. 1175-1178, September, 2008

[39] H. Urey, C. Kan, W. O. Davis, "Vibration mode frequency formulae for micromechanical scanners," *Journal of Micromechanics and Microengineering, vol.* 15, pp. 1713-1721, 2005 .

[40] Design, Modeling and Characterization of Electrostatically Actuated Microscanners, MSc Thesis, Çağlar Atman, Koç University, 2004.

[41] D. Elata H. Bamberger, "On the Dynamic Pull-In of Electrostatic Actuators With Multiple Degrees of Freedom and Multiple Voltage Sources," *Journal of Microelectromechanical Systems,* vol. 15, pp. 131-140, 2006.

[42] H. R. Seren, H. Urey, "Optical Characterization of Micro and Nano Mechanical Systems in Two Dimensions," submitted to *Proc. of Eurosensors 2008*.

[43] A. D. Yalcinkaya, H. Urey, D.Brown, T. Montague, R. Sprague, "Two-Axis Electromagnetic Microscanner for High Resolution Displays," *Journal of Microelectromechanical Systems*, vol. 15, pp. 786- 794, 2006.

[44] A. Arslan, C. Ataman, S. Holmström, K. Hedsten, H. R. Seren, P. Enoksson, H. Urey, "Mechanically Coupled Comb Drive MEMS Stages*," IEEE/LEOS Optical MEMS & Nanophotonics 2008,* pp. 140- 141, 2008.

[45] C. Ataman, A. Arslan, S. Holmström, H. Urey, "Comb Actuated Resonant MEMS Platform with Mechanical Amplification," submitted to *Journal of Microelectromechanical Systems.*

[46] E. I. Butikov, "Parametric excitation of a linear oscillator," *European Journal of Physics*, vol. 25, pp. 534-554, 2004.

[47] Available online at http://www.jstor.org/pss/2687680

[48] C. Ataman, H. Urey, "Nonlinear Frequency Response of Comb-Drive Microscanners," *Proc. SPIE of MOEMS Display and Imaging Sytems II,* vol. 5348, pp. 166- 174, 2004.

[49] H. Schenk, P. Dürr, T. Haase, D. Kunze, U. Sobe, H. Lakner, H, Kück, "Large Deflection Micromechanical Scanning Mirrors for Linear Scans and Pattern Generation," *IEEE Journal Of Selected Topics In Quantum Electronics,* vol. 6, pp. 715- 722, 2000.

[50] C. Ataman , H. Urey, "Modeling and characterization of comb-actuated resonant microscanners," *Journal of Micromechanics and Microengineering,* vol. 16, pp. 9-16, 2006.

[51] J. Mehner, S. Kurth, D. Billep, C. Kaufmann, K. Kehr, W. Dotzel, "Simulation of Gas Damping In Microstructures With Nontrivial Geometries," *IEEE Proc. of Micro Electro Mechanical Systems, 1998, MEMS 98*, pp. 172-177, 2008.

[52] F. M. White, "Fluid mechanics," *McGraw-Hill Higher Education*, 2008.

[53] H. Urey, S. Holmstrom, A. D. Yalcinkaya, "Electromagnetically Actuated FR4 Scanners," *IEEE Photonics Technology Letters,* vol. 20, pp. 30-32, 2008.

[54] M. Sayinta, S. O. Isikman, H. Urey, "Scanning Led Array Based Volumetric Display," *3DTV Conference*, pp.1-4, 2007.

[55] H. Suyal, A. McCarthy, A. C. Walker, A. J. Waddie, M. R Taghizadeh , "Direct Laser Written Polymer Structures and Passive Devices for Photonics Applications," *2005 Conference on Lasers and Electro-Optics Europe,* pp.505, 2005

[56] G. V. Steenberge, N. Hendrickx, E. Bosman, J. V. Erps, H. Thienpont, Peter Van Daele, "Laser Ablation of Parallel Optical Interconnect Waveguides," IEEE *Photonics Technology Letters*, vol. 18, pp. 1106- 1108, 2006

[57] Available online at http://www.zurich.ibm.com/st/photonics/characterization.html

[58] M. Fleger, D. Siepe, A. Neyer, "Microfabricated polymer analysis chip for optical detection," *IEE Proc.-Nanobiotechnol.,* vol. 151, pp. 159- 161, August 2004.

[59] M. Sayınta, A. Arslan, H. Suyal, M. Taghizadeh, H. Urey, "Polymer Waveguide and Led Array Integration On FR4 Scanner," Microoptics Conference, 2008.

[60] Available online at http://www.dipmec.univpm.it/misure/strumenti/LDV/ldv_en.html

VITA

Aslıhan Arslan was born in Ordu, Turkey on January 3, 1983. She received her Bachelor of Science degree in Physics from Middle East Technical University, Ankara, in June 2006. From 2006 to 2008, she worked as a research and teaching assistant in Optical Microsystems Laboratory and received her Master of Science degree in Electrical and Computer Engineering from Koç University. She is a student member of IEEE.